Adaptive optics correction for bent multimode fibres for use in biological imaging

Eusebiu Sutu

A thesis submitted for the degree of
Doctor of Philosophy

Lincoln College
University of Oxford
Trinity 2024

Abstract

Multimode optical fibres show great promise for *in vivo* imaging due to their thin profile, limiting invasiveness. However, propagation through such a fibre leads to scrambling of the light, which requires adaptive optics for compensation in order to create a focus at or near the output facet. Furthermore, changes in conformation due to bending lead to a change in transmission properties, limiting the ability to generate a focus at the output facet without recalibration. Hence, a requirement for effective imaging though an optical fibre is that one can adaptively change the calibration as the fibre conformation changes.

The thesis proposes an approach to correct for such changes in transmission and regain the ability to focus through a bent fibre, without access to the distal facet, as the system is intended for use during imaging. The method presented in this report uses a sensorless adaptive optics approach in concomitance with a Walsh mode representation of the modulated input optical field to correct for a bent fibre and increase the intensity of a desired focus. Then, with the use of memory effect, the area in which the correction is achievable is increased. However, the area in which a desired correction of at least 70% of the focus intensity generated with a fully calibrated fibre is limited. Thus, the approach shows that by using multiple correction targets, the entire facet of the fibre can be accounted for. Furthermore, the focus plane is not limited to only the distal facet, but it can be set at different axial depths, through the use of free-space propagation.

The correction procedure is dependent on the use of reflectors for the sensorless adaptive optics optimisation step. Thus, the thesis also proposes a novel approach for the simulation of Bragg gratings in multimode optical fibres, which can provide a tool in choosing the desired reflector to be used with the correction approach.

Acknowledgements

I would like to start by underlining my gratefulness to Prof. Martin Booth and Prof. Nigel Emptage, my two supervisors, for their guidance and support throughout my studies.

I am also grateful to Dr. Patrick Salter and Dr. David Phillips for their ideas and advice.

I am also grateful to Maike Lenz for her ideas and discussions.

Finally, I am also grateful to the Biotechnology and Biological Sciences Research Council and the Doctoral Training Centre for the financial support provided.

Contents

1 Introduction

1.1 Thesis motivation and brief description of achievements

Being able to observe neurons at a cellular level, observing their activity and plasticity while still performing in their natural environment, allows for a better understanding of their structural and functional properties. While microscopy allows for imaging at a cellular level, such a system often comes with limitations in terms of optical capabilities.

Observing a neuron in its natural environment can be impeded by optical aberrations and scattering generated by the refractive index changes occurring due to the presence of surrounding biological tissue. Adaptive optics is the area of optical engineering which strives to correct such aberrations in optical systems through the use of measurement algorithms and sensors to enable the use of hardware able to control the optical field as desired. However, even the applicability of adaptive optics is limited by the amount of scattering produced in a thick tissue, as is the case for deep-brain imaging.

Multi-mode optical fibres have proven to be an important tool in combating optical aberrations present during *in-vivo* imaging experiments, due to their ability to guide light to a desired location within an isolated propagation channel. Furthermore, their thin profile allows for imaging to be achieved while minimising the amount of damage to the surrounding tissue, limiting the observation of undesired malfunctioning neurons.

The light transmission though a multi-mode fibre can be characterised through the use of fibre modes. In an ideal fibre, the light coupled within these modes propagates unaffected by the other modes, nor influencing the propagation of other modes. However, due to differences in their propagation constants, the light is scrambled as it passes through the fibre. Thus, in order for a multi-mode fibre to be used in imaging, the light transmission needs to be characterised. This can be done through empirical interferometric measurements, the resulting transmission matrix describing the relationship between the input optical field and the resultant output optical field. Mathematically, this can be described as $\mathbf{y} = \mathbf{T}\mathbf{x}$, where $\mathbf{T}$ is the transmission matrix, $\mathbf{x}$ and $\mathbf{y}$ are the input and output optical fields, respectively, represented as a column vector of complex values representing the amplitude and phase of the electric field at specific sampled locations in the plane.

The drawback with the use of multi-mode fibres is that light transmission can be affected by changes in the fibre configuration, such as shape or temperature, leading to a loss in imaging quality. The change in light transmission occurs due to changes in the refractive index profile of the fibre due to bending or temperature.

This project focuses on correcting for changes in light transmission through a multi-mode fibre generated by bending. One of the sources of bending in practical neuroscience imaging experiments is the implantation procedure. As the fibre is flexible, implanting the fibre into an animal brain can lead to changes in shape as it travels toward the target location, being affected by the physical properties of the surrounding tissue. In the case of an anaesthetised animal, this application does not require for the correction to be time limited, as the implantation occurs only once at the beginning of the experiment and the fibre shape will not change during the experiment. Thus, the correction can be applied once before the imaging procedure occurs and the time required to correct will not affect the imaging procedure.

A second application is the deep-brain imaging of active animals. This application requires a fast correction procedure, in order to account for bending introduced by the movement of the animal.

Whether the imaging is achieved in a anaesthetised or active animal, being able to observe the neuronal activity and plasticity at a cellular level will allow for a better understanding of the mammalian brain, which could lead to further developments in the combat against neurological diseases. This can be done through the use of multimode fibres, while taking into account and correcting for any light transmission changes occurring due to bending.

Imaging though a multi-mode fibre (MMF) has already been implemented through the use of a point-scanning approach [1]. In order to obtain an image, a focus is scanned at the distal facet of the fibre, which acts as an excitation beam for use in fluorescence imaging. If tissue containing fluorophores is present at the focus location, they are excited and light at a different wavelength is being emitted through the effect of fluorescence. The emitted light is captured by the MMF and transmitted back to the proximal facet, where an imaging apparatus is present. The amount of emitted light is measured and the value obtained represents the intensity of a pixel in the final image.

In order to achieve focusing capabilities at the distal facet of the MMF, a calibration procedure is performed prior to imaging, where the transmission of light through the MMF is being measured and characterised through the use of a transmission matrix (TM). This information can then be used to calculate the required input optical field which would generate a focus at the output of the fibre. The input optical field is shaped through the use of the spatial light modulator. However, bending introduces changes in the transmission of the light through the MMF, resulting in a loss of focusing capabilities, which leads to a decrease in imaging quality.

Being able to re-measure the TM would represent the ideal case of a correction procedure, as then the light transmission would be fully characterised again, however, the same calibration approach cannot be used, as it requires access to the distal facet for interferometric measurement. During imaging, the MMF is implanted in the animal, thus, only proximal access would be available.

The first main contribution of the thesis is a correction approach intended to be used with a reflector placed at the distal facet to correct for a focus at the location of the reflector. This was achieved through a sensorless adaptive optics approach, making use of Walsh-Hadamard modes. The amount of light reflected was used as an optimisation parameter and the coefficients of the Walsh-Hadamard modes were individually changed to maximise the amount of reflected light through an iterative process. In order for the reflected light to be used as an optimisation parameter in achieving a focus at the desired location, the reflector must only reflect the light which contributes to the focus. Thus, a reflector must either be very small in size, comparable to the focus size, or some other approach, which has the same outcome, must be used, such as a fluorescent beacon. However, there were two drawbacks observed: the time required to obtain such a correction and the fact that focusing is only achieved at one specific location (at the reflector).

The time constraint, while important for imaging active animals, does not pose a problem for imaging applications at longer time frames, such as neuronal plasticity. However, recovering the focus at multiple reflectors will be required in order to achieve correction over the entire field of view, a requirement for a reasonable quality image to be acquired.

Expanding the locality of the correction can be achieved through the use of Memory Effect (ME) [2]. This approach is based on the assumption that a small bending does not drastically change the diagonal property of a straight fibre TM, a requirement arising due to assuming that the bent fibre TM is also diagonal, which allows for the reconstruction of the assumed TM from a single focus. However, this approach is limited, as the area in which adequate correction is achieved is dependent on the amount of bending and does not cover the entire distal facet. Thus, multiple reflectors are required to be used, each responsible of a part of the distal facet.

If a sufficient number of reflectors provides an acceptable level of correction across the distal facet, free-space propagation can then be used to generate the required field at the output of the fibre such that a focus at a desired location away from the facet can be generated.

The overall correction procedure is described by the following:

1. Regain the ability to focus at the reflectors
2. Use Memory Effect to regain the ability to control the field of the entire facet
3. Use free-space propagation to generate excitation foci at desired axial depths

The second main contribution of the thesis is a novel approach to simulating Bragg gratings in multimode optical fibres. The new approach manages to compute the propagation of light through an entire Bragg grating irrespective of its length, by directly solving the system of differential equations. However, some restrictions were placed on the type of grating:

1. The grating period must be constant, thus, chirped gratings are not able to be simulated
2. The cross-section region of the grating within the fibre transversal profile must remain constant, however, there is no restriction in terms of shape or location.

The reason for investigating Bragg gratings is their ability to be used as reflectors within the optical fibre, which could be used in the implementation of the correction procedure described in the first contribution.

1.2 Thesis outline

This thesis is composed of seven chapters, starting with an introduction to the thesis in the first. The second chapter describes the history, introduces the theory and some of the existing literature on which this thesis is based upon, drawing from research areas such as: microscopy, adaptive optics and fibre optics.

Chapter 3 describes the sensorless adaptive optics approach used in the correction procedure. It outlines the theoretical basis and implementation of the algorithm, making use of Walsh modes as an orthogonal basis. Finally, it provides some theoretical and experimental results of the approach. Chapter 4 describes the memory effect approach, outlining its use of the diagonal transmission matrix assumption and how it can be used to extend the focus correction area from one position. Chapter 5 describes how free-space propagation can be used to change the axial position of the focusing plane and combines the methods described in the previous two chapters to coalesce the correction procedure. The chapter provides a numerical analysis of the correction's effectiveness through simulations.

Chapter 6 describes the novel Bragg grating simulation approach in multimode optical fibres. It starts with an existing theoretical description of the light propagation through a Bragg grating, then describes a new approach to solving the entire set of differential equations. The chapter finishes with an outline of the implementation and simulation results of the novel approach.

Finally, chapter 7 represents a conclusion to the thesis which reiterates the achievements, discusses on their potential impact in the research scene and describes a number of directions the work can be improved upon and used in the future.

2 Background

2.1 Microscopy

Microscopy has been an area of study for centuries. Robert Hooke, in 1665 [3], presented illustrations of a new world unseen before, including detailed drawings of insects and plants. This book is also the first to coin the term cell, which is the foundation of biology. Robert Hooke's work came a few decades after the Dutch lens-maker Hans Janssen and his son Zacharias are attributed to have invented the compound microscope [4]. In this contraption, light which passes through the sample forms a magnified image of the sample by using two lenses (ocular/eyepiece and objective), the individual magnification of the two lenses being multiplied.

The most common form of microscopy is widefield microscopy, in which the whole sample is illuminated. The image can then be formed either using light transmitted through or reflected from the sample. However, other modes of illumination have been introduced over time. One of the drawbacks of widefield microscopy is that parts of the sample which are out of focus are still imaged and observed in a blurred state, leading to decreased quality of images acquired. In order to reject out-of-focus light, confocal microscopy was introduced [5]. The first step in reducing out-of-focus light is to restrict laser illumination to a single spot. This method allows for the light captured from the sample to then be refocused. Then, a pinhole acts as a spatial filter, as the centre of the refocus contains only light which originates from the in-focus position of the sample. Light originating from out-of-focus locations, focuses away from the centre and is blocked. While this method rejects out-of-focus light, only a small area is illuminated at any time. Thus, in order to image the entire sample, the illumination focus needs to be relocated to different positions and the different observations of the filtered light form together the entire image. This method is named scanning microscopy.

The earliest microscopy methods relied on observation of transmitted or reflected light. However, other methods such as fluorescence have become widely used. Fluorescence is a phenomenon in which a photon (or multiple) is absorbed, then after a few nanoseconds another photon is emitted, which has lower energy as some is lost in the process [6]. The main advantage of this process is that it is dependent on molecules, named fluorophores. Thus, the process can be localised by having these fluorophores only in specific structures of the sample, imaging only specific areas of interest, such as a cell membrane for example. In addition, fluorophores can also be used for revealing the function of the cell and observe cellular activity [7]. The process can be implemented in microscopic systems such as the confocal microscope described above. The emitted light, which is at a different wavelength to the illumination, can then be filtered through the use of a dichroic mirror, separating the optical paths.

The emission of light from fluorescence is dependent on the density of photons in the illuminated area. Processes such as two-photon fluorescence are non-linearly dependent on the illumination intensity due to being a second-order process, as using light with double the wavelength compared with 1-photon fluorescence requires the use of two photons to excite the same fluorophore. The advantage of two-photon fluorescence is reduced out-of-focus emission and larger penetration depth as a longer wavelength is less susceptible to scattering.

2.2 *In vivo* imaging

In the past 100 years, neuroscience has strived to understand the processes taking place inside the brain which give rise to cognition. While these processes can be studied at behavioural and computational level, they are the output of a complex neural network [8]. *In vivo* cellular imaging has provided the means for observing individual neurons while keeping intact the surrounding tissue and connections. Advancements in imaging technologies have extended the limits of *in vivo* observation to what was previously only achievable *in vitro* [9].

One of the limitations of *in vivo* imaging is the strong light scattering of different tissue components. Multi-photon fluorescence differs from single-photon, by utilising multiple photons of longer wavelength to achieve the same amount of energy required to excite the fluorophore. The advantage is that longer wavelength light is less susceptible to scattering, hence can penetrate further into tissue than shorter wavelength light. With the use of two-photon fluorescence microscopy, imaging depths of up to 1.6 mm have been achieved in cortex vasculature [10]. In the case of neuronal imaging, the focus power decreases drastically after 700 μm due to scattering in the white matter [11]. Three-photon fluorescence provides a better alternative. The drawback is that for larger depths, in order to keep the focal energy high, as required for multi-photon fluorescence, cortex heating can pose a problem [1]. A longer excitation wavelength also leads to a lower imaging resolution due to the diffraction limit. However, if scattering is the main limitation in imaging, using a waveguide to transmit the excitation light deep inside the brain eliminates the problem. The drawback is that this method is invasive.

An alternative approach is to use an imaging probe that is inserted into the tissue which minimises invasiveness. The best choice for minimising the footprint of the probe is to use an optical fibre [1]. The minimum invasiveness is of paramount importance in order for the biological system observed to perform as close as possible to homeostasis.

In order for a multimode optical fibre to be used for imaging, the transmission through it needs to be characterised, due to the light being scrambled by the fibre. This can be achieved by empirically measuring the fibre properties prior to implanting inside the brain [1]. One of the limitations of optical fibres is the sensitivity of light transmission to changes in the fibre's conformation. Thus, if the fibre bends, the prior calibration can become useless [12]. Compensating for this limitation is a main requirement in the quest for deep brain *in vivo* imaging in awake, behaving animals. Creating the technology necessary to enable the acquisition of *in vivo* images in a behaving animal is the main objective of this doctorate project. Imaging neuronal structures and monitoring activity within them will allow for a better understanding of how the brain functions. While it is possible to produce images from animals where the head is fixed, or while the animal is under anaesthesia, as both approaches limit movement, neither strategy is as valuable as permitting an awake animal to move and behave freely.

2.3 Optics and fibre optics

2.3.1 Light propagation

This subsection follows the work presented in Chapter 1 of [13].

Light is electromagnetic radiation. Thus, its evolution can be described with the use of Maxwell's equations. In the form shown below, an assumption is made that the media contains no free charge, which is generally the case in microscopy. Here $\vec{E}$ and $\vec{H}$ are the electric and magnetic field vector, respectively, ϵ is the permittivity of the medium and μ is the permeability of the medium.

$$
\begin{aligned}
\nabla \times \vec{E} &= -\mu \frac{\partial \vec{H}}{\partial t} \\
\nabla \times \vec{H} &= \mu \frac{\partial \vec{E}}{\partial t} \\
\nabla \cdot \epsilon \vec{E} &= 0 \\
\nabla \cdot \mu \vec{H} &= 0
\end{aligned}
\tag{2.1}
$$

The relations above can then be transformed into the wave equations below, where n is the refractive index of the media, which could vary spatially, and c is the speed of light in vacuum.

$$
\begin{aligned}
\nabla^2 \vec{E} - \frac{n^2}{c^2} \frac{\partial^2 \vec{E}}{\partial t^2} &= 0 \\
\nabla^2 \vec{H} - \frac{n^2}{c^2} \frac{\partial^2 \vec{H}}{\partial t^2} &= 0
\end{aligned}
\tag{2.2}
$$

In the case of a non-varying refractive index, further simplifying approximations can be made. More specifically, that there is no coupling between vector components of the fields. Thus, the wave equation above can be applied individually to the field's components. For example, below is shown the formulation for the x-component of the electric field.

$$
\nabla^2 E_x - \frac{n^2}{c^2} \frac{\partial^2 E_x}{\partial t^2} = 0 \tag{2.3}
$$

Thus, in order to avoid deriving similar solutions for every component, a scalar field u can be used instead, as shown below. It is important to note that the assumption is not valid if the refractive index varies. Scalar approximation also can induce errors at the interface between two media, where different boundary conditions might apply to different components. Later in the report, when describing light propagation through a fibre, the analysis will consider the full vectorial approach. However, for beams propagating in free space, these assumptions are practical.

$$\nabla^2 u - \frac{n^2}{c^2}\frac{\partial^2 u}{\partial t^2} = 0 \tag{2.4}$$

Through the use of a Fourier transform in the time domain, the wave equation above can be modified into the Helmholtz equation form shown below, where $k^2 = -\frac{\omega^2 n^2}{c^2}$ is the wave number, $\omega = 2\pi\nu$ and ν is the temporal frequency of the light. As in the case of monochromatic light the periodic temporal component is constant across the optical field during propagation, it is usually omitted in derivations.

$$\nabla^2 u + k^2 u = 0 \tag{2.5}$$

2.3.2 Diffraction and Fourier optics

This section summarises the work presented in Chapters 3 and 4 of [13].

A general plane wave can be described as $u(x, y, z) = U_0 \exp[i(k_x x + k_y y + k_z z)]$, which is a solution to the Helmholtz equation, where (k_x, k_y, k_z) are the wavenumber components, which satisfy $|\vec{k}|^2 = k_x^2 + k_y^2 + k_z^2 = \left(\frac{2\pi}{\lambda}\right)$, and U_0 is a complex number describing the amplitude and phase offset of the plane wave. The reason for introducing plane waves is the possibility of decomposing a complex field into a superposition of such plane waves.

In imaging, it is of interest to describe the change in the optical field from one plane to another. Mathematically, we are interested in the transformation $u(x, y, z = 0) \rightarrow u(x, y, z = z)$, where the starting position can be considered at $z = 0$ without loss of generality.

The method in which a field can be decomposed into planar waves is through the use of Fourier transform. Applying the Fourier transform to the field at $z = 0$, result in the equation below, where $A(k_x, k_y, z = 0)$ is the transverse angular frequency spectrum of the field.

$$A(k_x, k_y, z = 0) = \iint_{-\infty}^{\infty} u(x, y, z = 0) e^{-i(xk_x + yk_y)} dx dy \tag{2.6}$$

If the inverse Fourier transform is applied, as shown below, the equation shows that the field $u(x, y, z = 0)$ is a superposition of plane waves.

Due to the restriction $|\vec{k}|^2 = k_x^2 + k_y^2 + k_z^2 = \left(\frac{2\pi}{\lambda}\right)$ being applied, any plane wave defined by (k_x, k_y) has a k_z associated. Thus, each plane wave will have a direction of propagation associated.

$$u(x, y, z = 0) = \iint_{-\infty}^{\infty} A(k_x, k_y, z = 0) e^{i(xk_x + yk_y)} dk_x dk_y \tag{2.7}$$

Repeating the Fourier transforms for the field at position z and applying the Helmholtz equation leads to the result below. This is a multiplication with a transfer function in the angular domain.

$$A(k_X, k_y, z = z) = A(k_x, k_y, z = 0) \exp\left[iz\sqrt{\frac{4\pi^2}{\lambda^2} - k_x^2 - k_y^2}\right] \tag{2.8}$$

The term under the square root is not always positive. More specifically, it is negative for $k_x^2 + k_y^2 > \frac{4\pi^2}{\lambda^2}$, which introduces another i term into the exponential, thus transforming it from an oscillation to decaying function. In other words, plane wave components corresponding to high frequency values become an evanescent wave, which does not propagate. For this reason, there is a diffraction limit to the achievable resolution in an imaging system.

The Fresnel approximation can be made if the distance between planes is comparably larger than the wavelength, such that $\lambda^2 k_x^2,\ \lambda^2 k_y^2 << 4\pi^2$, as the angles of interest of the component plane waves are small. Thus, a first order approximation using the Taylor expansion of the square root can be done: $\sqrt{1-\frac{\lambda^2 k_x^2}{4\pi^2}-\frac{\lambda^2 k_y^2}{4\pi^2}} \approx 1-\frac{\lambda^2}{8\pi^2}(k_x^2+k_y^2)$.

Thus, the transfer function exponent becomes:

$$H(f_x, f_y; z) = \exp\left[i2\pi z\frac{1}{\lambda}\left[1-\frac{\lambda^2}{8\pi^2}(k_x^2+k_y^2)\right]\right] = \exp\frac{i2\pi z}{\lambda}\exp\left[-i\frac{z\lambda}{4\pi}(k_X^2+k_y^2)\right] \tag{2.9}$$

The first term is a constant global phase which can be ignored. Applying the inverse Fourier transform to the transform function and convolving the result with the $u(x, y, z = 0)$ field leads to Fresnel's diffraction integral.

One application of this theory is for lenses. The change in field between entering and exiting a lens can be generally described though the use of a multiplication, as shown below, where $t_{lens}(x, y)$ is the modulation of the field done by the lens.

$$u_{exit}(x, y) = t_{lens}(x, y)u_{entry}(x, y) \tag{2.10}$$

In the paraxial approximation, the modulation is given by the form below, where f is the focal length of the lens. This modulation can also include a pupil function which blocks light passing outside the lens facet.

$$t_{lens}(x, y) = \exp\left[-\frac{ik}{2f}\frac{x^2+y^2}{2}\right] \tag{2.11}$$

The application of interest is the transformation of the field from a focal plane to the other. The form of such transformation in the angular spectrum domain would be in the form shown below, where the H transform is applied twice for the diffraction to and from the focal planes and a convolution at the lens.

$$A(k_x, k_y, z = +f) = H(k_x, k_y; f)\left[T_{lens}(k_x, k_y) \otimes [H(k_x, k_y; f)A(k_x, k_y, z = -f)]\right] \tag{2.12}$$

The same relationship can be written in the spatial domain by using the inverse Fourier transforms versions of the functions and swapping multiplication with convolution.

The final result in the spatial domain is shown below, where (x,y) are the transversal spatial coordinates of the input plane and (v,w) are the transversal spatial coordinates at the output plane.

$$u(v, w, z = +f) = \frac{1}{i\lambda f} \iint_{-\infty}^{\infty} u(x, y, z = -f) \exp\left[-i\frac{2\pi}{\lambda f}(xv + yw)\right] dxdy \tag{2.13}$$

This result is a Fourier Transform, where the output spatial coordinates are proportional to the spatial frequencies of the input field. More specifically: $k_x = \frac{2\pi v}{\lambda f}$, $k_y = \frac{2\pi w}{\lambda f}$. This allows for access to the Fourier plane of an optical field by passing it through a lens.

2.3.3 Optical fibres

When describing the transmission through an optical fibre, due to the circular symmetry of an ideal fibre, a cylindrical coordinate system is best suited. Thus, the parameters used are r (radius coordinate), ϕ (azimuthal angle coordinate), z (axial coordinate) and t (time coordinate). Limiting the analysis to only one specific value of the optical field in z-component of the spacial frequency k_0 and one value in the temporal frequency ω (eliminating the Fourier transform integrals), the electric field can be described as below, where the propagation constant $\beta = nk_0$ is used instead. The same relationship can be written for the magnetic field $\vec{H}$.

$$\vec{E}(r, \phi, z, t) = \vec{E}(r, \phi) \exp[i(\omega t - \beta z)] \tag{2.14}$$

As the unit vectors in the radial and azimuthal direction are not constant, solving the Maxwell equations is hard. However, this is not true for the z-component, where the usual form of the resultant Helmholtz equation $(\nabla^2 + k^2)E_z = 0$ still holds, where ∇^2 is the Laplacian operator in cylindrical coordinates and k is the wavenumber. The same relationship applies to the magnetic field component H_z. Solving the partial differential equation and applying the boundary conditions will lead to a set of propagating fibre modes. The details described above and the subsequent derivation for a step-index optical fibre is described in Chapter 3 of Amnon Yariv's book [14]. However, these modes, while they describe the propagation in an optical fibre, are difficult to work with, especially in an experimental setting, because the polarisation of light is not uniform across the transverse plane $(r - \phi)$.

Working under the assumption that the difference between the core and cladding refractive indices is small (weakly guiding fibres), the boundary continuity conditions can be simplified and the propagation modes can be approximated to a set of linearly polarised modes (LP modes), which have the property of uniform polarisation. For the x-polarisation state, the transverse electric field takes the form: $E_x = AJ_l(hr) \exp il\phi \exp[i(\omega t - kz)]$, where A is a constant given by boundary conditions, J_l is the Bessel equation of first kind of order l, l is azimuthal index taking integer values $(\ldots, -2, -1, 0, 1, 2, \ldots)$, $h^2 = k^2 - \beta^2$. The magnetic transverse field takes the form: $H_y = \frac{\beta}{\omega\mu} E_x$, where μ is the permeability of the fibre core. As the light is linearly polarised, $E_y = 0$,$H_x \approx 0$. The y-polarisation state analysis is identical, as the azimuthal symmetry of the fibre can be used to approach the problem with a rotated frame of reference, leading to the same results.

One situation which arises is that the x-polarisation and y-polarisation modes are degenerate, in other words, their propagation constant β is equal. This results in coupling between the two modes even in an ideal straight fibre. However, as the transversal field envelope is identical, coupling between the two modes only changes the direction of the linear polarisation. For a short length of the fibre, the coupling between polarisation states is small, thus, the light can be assumed to maintain its linear polarisation and the scalar approximation becomes a reasonable model, by only focusing on the component of the electrical field on which the polarisation is aligned with. Mathematically, instead of working with the vector $(E_x, E_y = 0)$, E_x can be used alone.

Polarisation coupling can present an issue experimentally, for example when measuring the phase of a field using interferometry. However, while keeping the property of uniform polarisation, circularly polarised (CP) modes can be used instead. Plöschner et al. [1] have shown that CP modes have the same profile as the LP modes, however, due to spin-orbit interaction between the polarisation and orbital angular momentum generated by the phase profile, the propagation constants of the modes with different polarisation are different. Thus, the modes are not degenerate anymore. This leads to circular polarisation being preserved. The specific propagation constants can be approximated to the first order from the LP propagation constants. The project has used CP modes.

The general case described above is of the multimode fibre (MMF). A specific case which arises, is the single-mode fibre (SMF), where there is only one propagating fibre mode. The number of modes in a fibre is determined by specifications such as core diameter, numerical aperture (NA), wavelength of the light propagated through the fibre and its refractive index profile. In terms of the latter, different versions can be constructed: step-index fibre, where the core and cladding have different but uniform refractive indices, or graded-index fibre where the refractive index of the core gradually decreases from a maximum value to the cladding value [15].

The advantage of SMFs, is that there is no modal scrambling, as there is only one propagation mode. This can be important in communications applications, as it allows for a larger bandwidth of data transmission. In imaging applications, where controlling the position of the output focus is required, using one SMF is not useful. Multiple SMFs can be used in endoscopic applications in the form of a bundle of fibres, where each fibre corresponds to a pixel in the final image. However, the large size of the fibre bundle defeats the purpose of minimising invasiveness in neurological applications. Thus, a MMF is a better choice. However, a SMF can still be used for example to carry the reference beam required for the interferometry used in calibrating the MMF.

In terms of refractive index profile, it was shown that graded-index fibres are more robust to changes in transmission due to bending [16] and that they are a good candidate to use in imaging. However, for graded-index fibres to be as resistant to changes in propagation due to bending, a precise refractive index profile is required. Unfortunately, current manufacturing precision is still not at a desired level. Thus, commercially available fibres still require correction to bending to be used in imaging. This project has only focused on the step-index fibre correction. However, the correction procedure is applicable to graded-index fibres, the only requirement being a correct description of the graded-index fibre modes.

2.3.4 Calibrating an optical fibre

Input light to a MMF couples into the different fibre modes and in the ideal case is transmitted without coupling to the output. However, due to the propagation

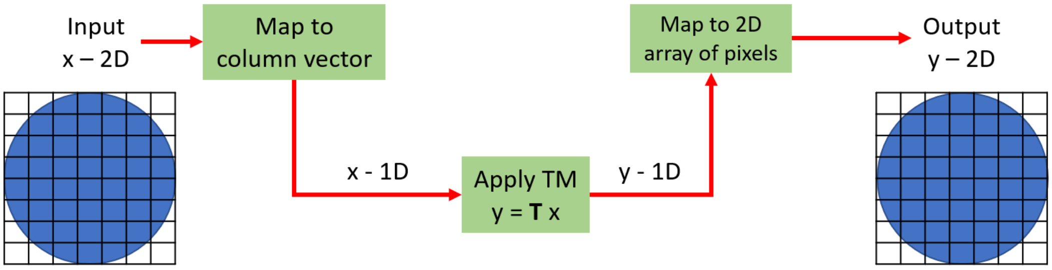

Figure 1: Diagram illustrating the procedure to apply a given TM to relate an input field to the output of the fibre.

constants of the modes being different, the phases of the output components are desynchronised, which leads to observation of a seemingly random speckle pattern. However, this scrambling is not stochastic, but deterministic. The transmission can thus be measured empirically in an experimental setting.

Such measurement is usually formulated as a matrix, coined the transmission matrix. In order for a matrix to be used, the optical fields at the input and output of the fibre need to be composed of a finite number of sampled locations. Then, the transmission matrix describes the transmission of light from every input sample location to every output sample location. Mathematically, it can be described by a matrix multiplication: $\mathbf{y} = \mathbf{T}\mathbf{x}$, where $\mathbf{x}$ and $\mathbf{y}$ are the input and output fields respectively, each represented as a vector that maps onto the a Cartesian space of pixels, and $\mathbf{T}$ is the transmission matrix. An illustration of the process undergone in the application of the TM to relate the input to the output of a fibre is shown in figure 1.

The matrix approach is similar to describing the propagation of light through a lens. Between the input and the output focal planes there is a Fourier transform relationship, which can be described through the use of a discrete Fourier transform matrix. Thus, changing the objective lens of a microscope system for a MMF leads to a similar approach to describe light transmission, through the use of a matrix multiplication.

A description of the calibrating algorithm is given in [17]. The process works by focusing light at the input facet into one sample location at a time. At the output end of the fibre, a camera captures the pattern observed. In order for phase information to be extracted, the output facet is interfered with a reference beam. Then the global phase of the input light is changed, by adding a constant phase across the spatial light modulator (SLM), scanning in the range of $[0, 2\pi)$. As the reference beam has a constant phase and the output pattern only has its global phase changed, the relative phase information between output pixels can be retrieved by observing the interference pattern. One iteration of this process relates one input to all outputs. Thus, a column of the TM is measured. The process is then repeated for all the other input pixels, until the entire TM is measured.

In order to generate a focus at the output facet, the values of the input pixels is chosen such that their complex summation of their individual contribution to the output pixel maximises intensity (absolute value). This can be achieved by setting the input phases such that their output contributions are in phase at the output pixel location. One important note to mention is that the algorithm does not require the output plane to be at the fibre facet. The acquisition camera can be set such that it focuses away from the facet. Calibrating the fibre in such a manner allows for the generation of a TM which relates the input field to an output field at the focal plane of the acquisition camera.

2.3.5 Matrix representation of the transmission through an optical fibre

For a given fibre mode of index k, let its profile be described as a column vector ψ_k, where each element represents the optical field value sampled at a given location. The locations are taken to be a Cartesian mesh-grid to better overlap with what a camera might observe or how an SLM might modulate the light field. Thus, for a specific mode coefficient A_k, the optical field in the Cartesian pixel basis can be described as: $\mathbf{x_C} = \psi_{\mathbf{k}} A_k$.

The light propagating through an optical fibre, is a superposition of propagation modes, each with an associated coefficient. Thus, the superposition equation $\mathbf{x_C} = \sum_{k=0}^{M} \psi_{\mathbf{k}} A_k$, where M is the number of propagation modes, can be represented as a matrix multiplication, where $\mathbf{\Psi}$ is the mode matrix and $\mathbf{x}_M$ is the column vector of mode coefficients, or in other words, the optical field in the fibre mode basis:

$$\mathbf{x}_C = \begin{pmatrix} \psi_{\mathbf{1}} & \psi_{\mathbf{2}} & \dots & \psi_{\mathbf{M}} \end{pmatrix} \begin{pmatrix} A_1 \\ A_2 \\ \vdots \\ A_M \end{pmatrix} = \mathbf{\Psi} \mathbf{x}_M \tag{2.15}$$

Thus, $\mathbf{\Psi}$ represents the matrix transformation from the modal basis to the Cartesian basis. As the fibre modes form an orthogonal basis, then a normalisation can be chosen for the fibre mode profiles such that $\psi_k^\dagger \psi_k = 1$ and $\psi_k^\dagger \psi_j = 0$ for $k \neq j$, where † represents the conjugate transpose. Thus leading to the relationship:

$$\mathbf{\Psi}^\dagger \mathbf{\Psi} = \mathbf{I}_M \tag{2.16}$$

Multiplying equation 2.15 by $\mathbf{\Psi}^\dagger$ on the left side leads to:

$$\mathbf{\Psi}^\dagger \mathbf{x}_C = \mathbf{\Psi}^\dagger \mathbf{\Psi} \mathbf{x}_M = \mathbf{x}_M \tag{2.17}$$

Thus, $\mathbf{\Psi}^\dagger$ represents the matrix transformation from the Cartesian basis to the modal basis. It is important to note that $\mathbf{\Psi}\mathbf{\Psi}^\dagger \neq \mathbf{I}_M$. More specifically, this matrix transformation represents the projection of an arbitrary optical field into the modal basis. Thus, components of the optical field which do not couple into the fibre modes are lost. Specifically, it is the transformation from Cartesian basis to modal basis which generates this projection ($\mathbf{\Psi}^\dagger$). However, if the Cartesian optical field is already entirely within the mode basis space, then the matrix transformation has the same effect as an identity matrix (no transformation).

An ideal fibre will generate no coupling between the modes as light propagates through it and the propagation is defined by the propagation constants of the modes only. This relationship can be described in terms of a transmission matrix $\mathbf{TM}_M$, where $\mathbf{x}_M$ and $\mathbf{y}_M$ represent the input and output optical fields in the mode basis, β_k represents the propagation constant of mode k and L represents the length of the fibre:

$$\mathbf{y}_M = \begin{pmatrix} e^{i\beta_1 L} & 0 & \dots & 0 \\ 0 & e^{i\beta_2 L} & \dots & 0 \\ \vdots & \vdots & \ddots & \vdots \\ 0 & 0 & \dots & e^{i\beta_M L} \end{pmatrix} \mathbf{x}_M = \mathbf{TM}_M \mathbf{x}_M \tag{2.18}$$

Making use of the Cartesian to mode basis transformation and considering that the output optical field is assured to be entirely within the mode basis space, thus, the projection to mode basis is acting as an identity matrix, a relationship can be described between the Cartesian based TM and the modal based TM.

$$\mathbf{\Psi}^\dagger \mathbf{y}_C = \mathbf{TM}_M \mathbf{\Psi}^\dagger \mathbf{x}_C$$

$$\mathbf{y}_C = \mathbf{\Psi} \mathbf{TM}_M \mathbf{\Psi}^\dagger \mathbf{x}_C \tag{2.19}$$

$$\mathbf{TM}_C = \mathbf{\Psi} \mathbf{TM}_M \mathbf{\Psi}^\dagger \tag{2.20}$$

Multiplying by $\mathbf{\Psi}^\dagger$ on the left side and with $\mathbf{\Psi}$ on the right side and using the orthogonality of the modes gives the mode base TM as a function of Cartesian base TM:

$$\mathbf{TM}_M = \mathbf{\Psi}^\dagger \mathbf{TM}_C \mathbf{\Psi} \tag{2.21}$$

2.3.6 Analytical description of the transmission through a bent multimode fibre

Once the propagation through a MMF is formulated, a closer look at the bending effects can be taken. M. Plöschner et al. [12] stated that there are two main effects which take place: geometric and compressive. The geometric bending effect occurs due to a change in the optical path length through the fibre, as light propagating on the inside of the bending travels a shorter path than on the outside. The compressive bending effect occurs due to stresses in the fibre which change its refractive index, thus affecting the optical path length as well. These effects were formulated theoretically for the case of a circular fibre bend of a given curvature radius.

The specific analysis can be found in the methods section of the cited article, however, the main conclusion is that the bent fibre will have a different set of propagation modes, with a different set of propagation constants associated. While these could be computed, it would need to be done for all bending radii, individually. A more straightforward approach is to keep the straight fibre mode basis, but acknowledge that due to the change in actual propagation mode basis, the transmission is no longer without mode coupling.

The transmission through the circularly bent fibre in the x-z plane can be formulated though the use of a helper matrix $\mathbf{B}$ whose elements are given below, where β_k is the straight fibre propagation constant of mode k, $\delta_{kj} = 1$ for $j = k$

and 0 otherwise, n_core is the core refractive index, k_0 is the vacuum wavenumber, ρ is the bending radius, ψ_k and ψ_j are the mode profiles of modes k and j, respectively. $\xi = 1-(1-2\sigma)\frac{n_{core}-1}{n_{core}}$ is a factor which arises due to the compressive bending effect, where σ is the Poisson ratio of the core material.

$$B_{kj} = \beta_k \delta_{kj} - \frac{n_{core} k_0}{\rho} \langle \psi_k | x\xi | \psi_j \rangle \tag{2.22}$$

The bra-ket term can be expanded into:

$$\langle \psi_k | x\xi | \psi_j \rangle = \frac{\iint_{-\infty}^{\infty} \psi_k^* x \xi \psi_j dxdy}{N_k N_j} \tag{2.23}$$

where:

$$N_k = \sqrt{\iint_{-\infty}^{\infty} |\psi_k|^2 dxdy} \tag{2.24}$$

Finally, the mode base transmission matrix on the bent fibre is given by the matrix exponential:

$$\mathbf{TM}_{M,bent} = e^{i\mathbf{B}L} \tag{2.25}$$

An arbitrary shape could then be approximated as a series of small circularly bent sections, thus allowing for the calculation of the transmission through a fibre with a specific shape.

In the case where the bending is not done in the x-z plane, but at an angle θ counter-clockwise with respect to x-axis, the same approach can be used, but substituting x in the bra-ket term with $x\cos\theta + y\sin\theta$ (equivalent to an axis rotation).

2.3.7 Correcting for bent optical fibres

S. Farahi et al. [18] have implemented a method for measuring the conformation of a fibre by delivering light at the distal end of the fibre, the end further from the laser source, through the use of micro-optics. The output at the proximal end, towards the laser source, was measured and compared against a large databank of images. The drawbacks of this method are the large dataset required before imaging and the need for access to the distal end. The latter would be impossible in an in vivo biological imaging context as it would be implanted inside the mouse brain.

Ruo Yu Gu et al. [19] have proposed a method to characterise the transmission matrix in a bent fibre with the use of a checkerboard reflector at the distal end of the fibre, which eliminates the need for access at that end. Starting with an initial calibration, a new transmission matrix is calculated continuously to measure the change. The drawback is that the new calibration needs to be fast in order to account for the continuous change in fibre shape. This can prove difficult for a large number of modes, as the matrix itself is large. Noise can also prove to be an obstacle, as increasing the number of modes leads to a requirement for better signal to noise ratio.

G. Gordon et al. [20] have described a method which builds on the previous one. It relies on stacking multiple checkerboard reflectors, which provide further encoding based on polarisation and wavelength. This is a more general approach as it would a apply to non-unitary transmission matrices, which would occur in cases where energy is lost during transmission. The matrix is inferred by using an iterative algorithm based on a first order model approximation from recording done at different wavelengths. The main drawback is the time requirement, as in their case 14.5 minutes were needed for convergence. This is extremely slow if the technology target is to strive for correcting rapid changes in fibre shape, which might arise during imaging of more active specimens.

Given that the main limitation in the above-mentioned two methods is the time requirement for correction during imaging, a better approach could be through the use of machine learning. In this way, computational time is shortened at the expense of lengthy training, which can be done prior to imaging.

Y. Liu et al. [21] have trained a convolutional neural network on speckle patterns recorded at the distal end of the fibre, which was deformed by translating the proximal end in the z-dimension (the central axis of the fibre). The data was acquired at 21 different proximal end positions, resulting in 21 classes for which a classifier network was trained. The data was split into a training dataset and a validation dataset. The training result was quantified through measuring the accuracy of inference on both the training dataset and validation dataset, the accuracy being defined as the percentage of correct classifications. While this method uses the distal end, it did show that the accuracy of a trained network can be over 90% for a specific fibre. The authors trained two networks for two different fibres, but did not investigate the network accuracy on data obtained from a different fibre compared to the training dataset.

P. Fan et al. [22] have trained a network on recorded images at the distal end, while inputting at the proximal end a set of binary images using digits or letters. There were three different bending states used, each with its own trained network. The classifier's accuracy was over 90%, but lacked when applied to a state different to its trained one. This shows that there is a low correlation coefficient of the output between the states. This reduces the possibility of using a simple linear regression to determine the correct change in transmission, while at the same time it could increase the chances of a more complex network to differentiate between states, which is my goal.

In order to train a network to correctly calculate the change in transmission, a large amount of data is needed. This could prove difficult and time consuming to do experimentally. Thus, through the use of a simulation, training data can be generated. While the project will not focus on the use of machine learning, the simulation program can be used for a network approach.

2.3.8 Experimental optical system

The project, while heavily focused on theoretical and computational approaches, was meant to have a experimental application on an existing optical system capable of imaging through a MMF. A simplified schematic of the microscope system is illustrated in figure 2. The system can be split into three modules: the laser module, the MMF module and the calibration module. The purpose of the laser module was to split the light from the laser and send it to the other two stages. The laser (CrystalLaser DL488-030-SO) generated a continuous waveform beam of linearly polarised light with a wavelength of 488 nm. The halfwave plate (HWP1) changed the direction of the linear polarisation, such that the following polarising beam splitter (PBS) was able to send two orthogonal linearly polarised beams to the optical fibres for light transport.

Light to the MMF module was sent through a polarisation maintaining optical fibre (PMF), as the light reaching the SLM needed to be aligned with the polarisation axis of the SLM. An iris was placed in the Fourier plane of the SLM in order to filter only one diffraction order of the light reflected by the modulator. The filtered light then passed through a quarter-wave plate (QWP1) which changed the polarisation of light from linear to circular. The reason for using circularly polarised light through the MMF was due to circular polarisation being better preserved than linear polarisation (section 2.3.3). The filtered light was then passed through a 4f system to properly couple the light into the proximal facet of the MMF.

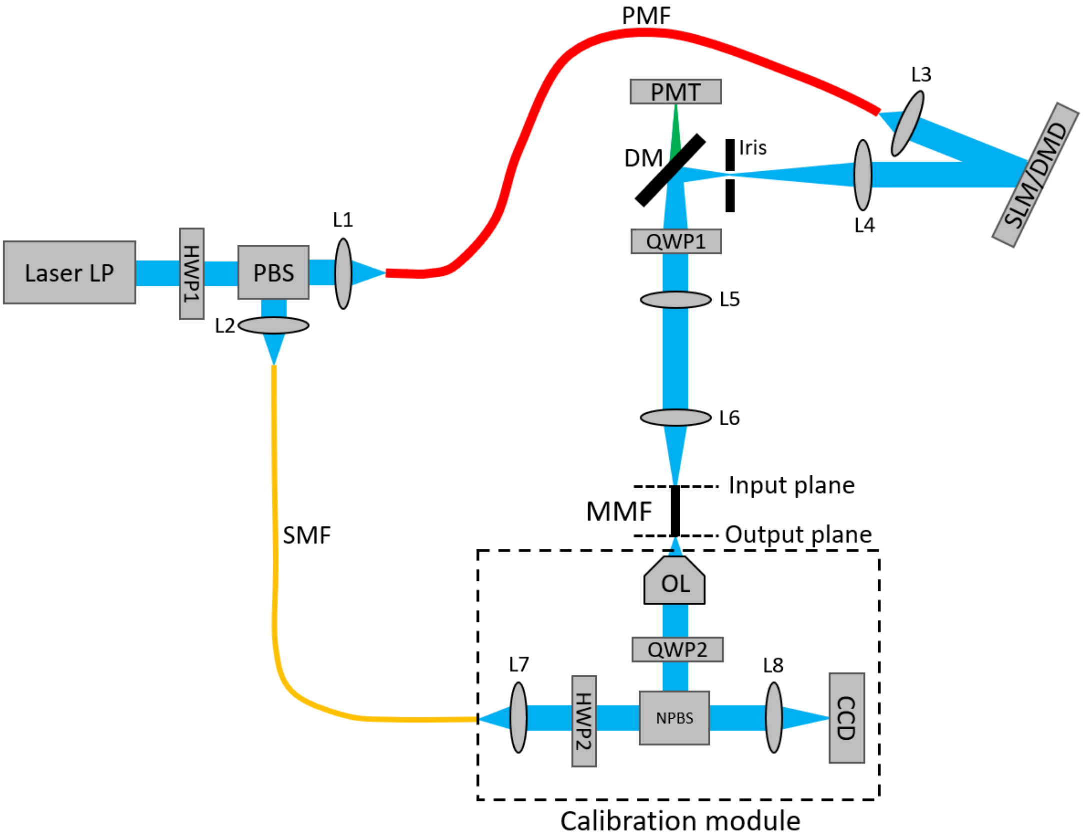

Figure 2: Simplified schematic of the optical system target for which the computational simulations were used. Abbreviations are defined in the main text.

During calibration, a calibration module was placed at the output of the MMF. Light from the MMF was magnified by an objective lens (OL) after which it passed through another quarter-wave plate (QWP2) which changed the polarisation from circular to linear, which then was interfered with a reference beam onto a non-polarising beam splitter (NPBS). The reference beam was delivered from the laser module by a single-mode fibre (SMF). While the single-mode fibre maintained the linear polarisation, it did not maintain its direction. Thus, before the reference beam was interfered on the NPBS, a half-wave plate (HWP2) was used to change the polarisation direction to match the light received from the MMF. The resultant interference pattern was imaged onto a charged-coupled device (CCD) camera. During imaging, the calibration module was replaced by the animal to be observed, by implanting the MMF in the brain tissue. At the output plane of the MMF, laser light was focused onto the tissue. Emission of fluorescent light was captured by the MMF and passed back through the 4f system. A dichroic mirror (DM), which only reflected light at 488 nm was used to filter the emitted light, which was at a different wavelength. The emitted light was captured and measured by a photo-multiplier tube (PMT). Each measurement of the PMT represented the intensity of one pixel in the final image.

2.3.9 Simulation environment

The thesis is based on a simulation environment created in Matlab, which allows for the numerical simulation of light propagating within a multimode fibre.

The first step in the program development has been to generate the linear polarisation modes in an optical fibre. For this step the function present in the GitHub repository created by Szu-Yu Lee have been used [23]. However, this is the only code in the simulation program which has been taken from an external source.

Then, using the mathematical approaches in article [12], functions were written to compute the changes in propagation constants and profile of the CP modes, allowing for future simulations to be done in a circular polarisation basis. Furthermore, using information from the same article, the functions computing the mode coupling for a circularly bent fibre were also written.

These functions represent the basis of the simulation program. Further additions are described in future chapters.

3 Refocusing using sensorless adaptive optics

3.1 Introduction

Adaptive optics (AO) is a technology used in optics to correct for aberrations which might arise in the optical system. It has been initially developed for astronomy applications, in order to correct for aberrations introduced by atmospheric turbulence [24]. While telescopes, such as Hubble and James Webb, can be sent into space, where the problem of imaging through the atmosphere is avoided, there are limitations, mainly in size and weight. Having larger telescopes is beneficial, as the resolution of imaging is directly related to the size of the capturing mirror/antenna. Atmospheric turbulence can be minimised by carefully choosing the location of such telescopes, for example on top of a mountain such as the Mauna Kea Observatories in Hawaii. However, aberrations can not be entirely avoided, some even arising from wind generating vibrations in the telescope structure.

Over time, adaptive optics has also found its use in high resolution microscopic imaging [25]. Optical aberrations in microscopy mainly arise due to specimen structure, due to changes in refractive index distribution, which hinder the formation of a high quality focus, which in the best case is limited by diffraction, a target of high resolution imaging. This non-uniform refractive index leads to changes in the optical wavefront as it passes through the sample. The fundamental principle upon which AO works is modulation of the wavefront in order to compensate for any aberrations which might arise. If the inverse effect of the aberrations is applied onto the optical field, then it cancels out with the sample aberrations leading to a high-quality focus. In practice, such wavefront modulations are achieved using devices such as liquid crystal spatial light modulators (SLM), deformable mirrors or digital micromirror devices (DMD).

The second main component of AO is a method for characterising the aberrations, such that the correct modulation is applied. Sensor based AO relies on the use of a wave-front sensor, which measures the amount and spatial distribution of aberrations, information which is then used to infer the required modulation for correction. One example of such sensor is the Shack-Hartmann wave-front sensor [26], which uses an array of lenslets to sample the optical field by focusing small sections onto a camera device. The displacement of the focus from the centre is then proportional to the phase gradient of the optical field, which can then be approximated using a set of local tip/tilts. Tip and tilt are linear phase gradients applied to the optical field in perpendicular transversal directions. The name arises from the possibility of inducing such changes by tipping or tilting a mirror on the optical path.

While such methods are able to directly describe the nature of the aberrations, they typically involve an increase in complexity of the optical system. The more stringent requirement is access to the aberrated optical field, which needs to be observed by the sensor. In the *in vivo* imaging case, it might not be possible, as the aberrated fields occur inside the specimen.

An alternative is sensorless based AO, which uses the image acquired to infer the state of the optical field. The method functions by measuring a chosen parameter, such as intensity or contrast, and modulating the input light field, the chosen parameter is optimised.

The modulation to the field is usually represented in a basis which suits the aberrations intended to be corrected. One such basis is Zernike polynomials [27], which describe usual aberrations such as tilt, defocus, astigmatism, etc. However, in the case of the bent fibre, the aberrations introduced do not come in the usual forms described by Zernike polynomials. As the modulation applied is phase-only in nature and sampled in a pixelated format, a basis which is defined using these constraints is more appropriate, such as the basis defined by Walsh-Hadamard modes [28].

In this chapter, recovering the focus at a reflector at the distal facet of the optical fibre was investigated. This was done in preparation for using the memory effect to achieve correction over the entire distal facet and later over the entire target focal plane, as described in the following two chapters.

3.2 Mathematical description of Walsh mode modulation

Correcting for the change in light transmission through a bent MMF requires the observation and description of the optical field. Although in its raw representation, the field is sampled on pixels measured by a camera, it is usually best to represent the field using a modal expansion, as explained above. However, such Cartesian grid is inherently two-dimensional. In this configuration, any linear transformation on the optical field, such as phase modulation, would be 4-dimensional in nature, as a mapping from one 2D space to another 2D space. The easiest simplification of the problem is to map the 2D arrangement of pixels onto a 1D vector. For example, this can be achieved by restructuring the data in a column only, by concatenating consecutive columns from the grid vertically. The advantage of using the mapping is that linear transformations can now be represented by a 2D matrix, which is easier to work with. This representation is not unique, any permutation of the pixel values is usable. However, whichever representation is used, it needs to be adhered to for any calculations going forward.

The field itself is of complex value. However, the modulation device (SLM) only changes the phase parameter. This is modelled by multiplying the original field elements with phase-only complex values, as illustrated in equation 3.1, where x_c is the corrected field, x_1,x_2,...,x_p are the original field elements and

$e^{i\theta_1}$,$e^{i\theta_2}$,...,$e^{i\theta_p}$ are the modulations applied to each pixel. The element-wise multiplication can be represented as a linear transformation of the field, represented as a column, by matrix multiplication with a diagonal matrix representation of the modulation. Conversely, as the object of interest is the modulation and not the previously calibrated field, which is a starting constant during the correction procedure, the diagonal matrix and column representation can be switched in the form below.

$$x_c = \begin{pmatrix} x_1 \cdot e^{i\theta_1} \\ x_2 \cdot e^{i\theta_2} \\ \vdots \\ x_p \cdot e^{i\theta_p} \end{pmatrix} = \begin{pmatrix} x_1 & 0 & \cdots & 0 \\ 0 & x_2 & \cdots & 0 \\ \vdots & \vdots & \ddots & \vdots \\ 0 & 0 & \cdots & x_p \end{pmatrix} \begin{pmatrix} e^{i\theta_1} \\ e^{i\theta_2} \\ \vdots \\ e^{i\theta_p} \end{pmatrix} \tag{3.1}$$

The optical field is in itself a highly dimensional set of data, each pixel representing a dimension. One method of characterising the change of such field on the output of the optical system, is to modulate one dimension at a time. However, modulating a single pixel has minimal effect on the intensity at the output. Thus, it is better to use a modal representation in which all input pixels are modulated in every dimension. One such basis transformation can be done with the use of Walsh-Hadamard transform [28]. The optical field modulation can be represented as a superposition of Walsh modes, which in terms have a phase coefficient associated.

The Walsh modes are a set of orthogonal basis functions which take only binary values of +1 and -1, on sub-intervals defined by dyadic fractions (the denominator is a power of 2). In other words, in the 2-dimensional representation, if a row/column of one Walsh function is considered, the length of each consecutive sequence of identical valued pixels must be a dyadic fraction of the length of the row/column. For example, in the 8×8 case shown in figure 4, all bands have a vertical/horizontal length of 1, 2, 4 or 8 pixels, associated with 1/8, 1/4,

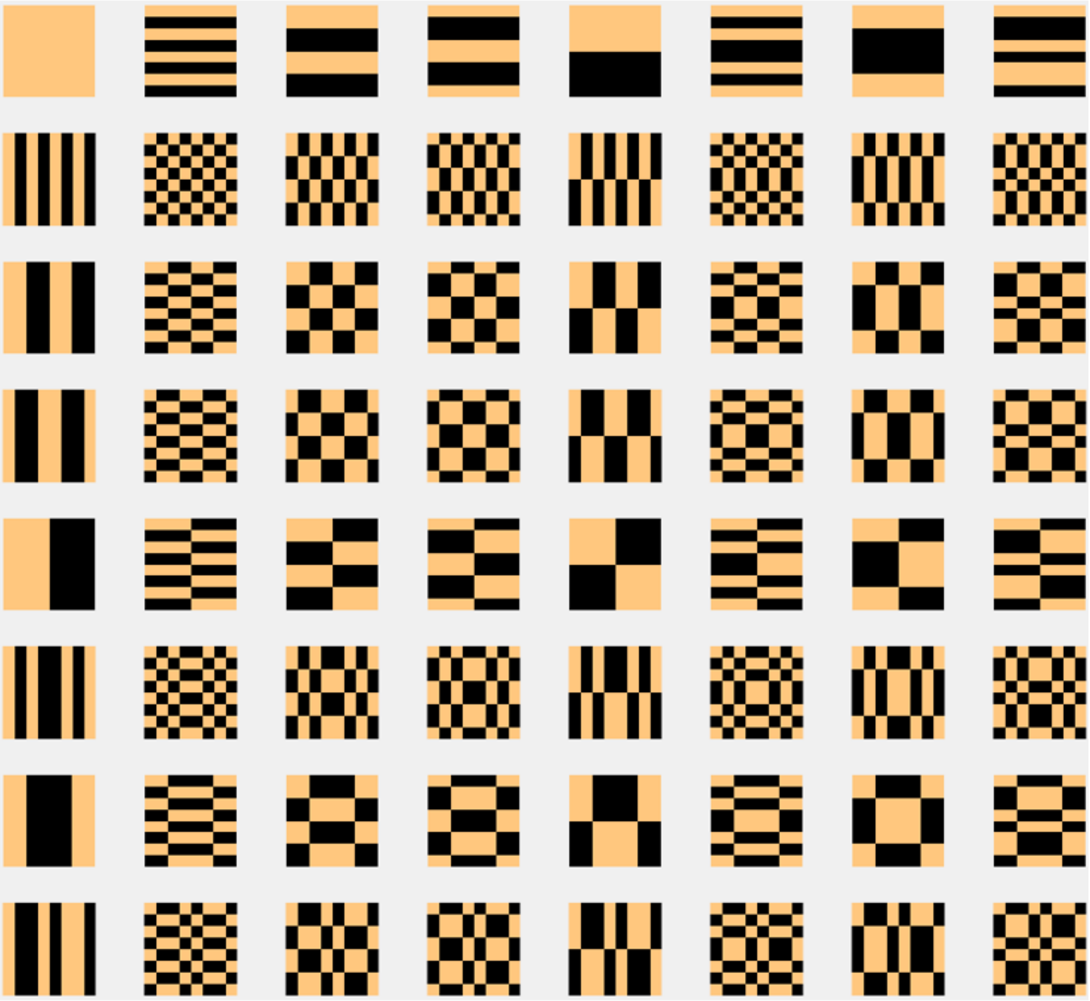

Figure 3: All the 8 × 8 size Walsh modes. Black represents a value of -1 and brown represents a value of +1.

1/2 and 1/1 dyadic fractions respectively. One of the limitations that Walsh mode representation introduces is the size of the optical field. As the modes are generated using dyadic functions, the size of the field in pixels, must be a power of 2, such as 8 × 8 shown in figure 3.

Through the mapping between a 2D matrix and a column vector, there is an equivalence between the inherent 1D representation of Walsh modes and the 2D representation in Fig. 3. The 1D column representation can be stacked into a square matrix, leading to the generation of the Walsh-Hadamard matrix, usually denoted with **H**. Multiplying it with a column vector containing the coefficients, the phase field is generated in the pixel domain is calculated. This is represented in equation 3.2, where $\theta_1,\ldots,\theta_p$ are the phase values of the optical field pixels, $\phi_1,\ldots,\phi_W$ are the Walsh mode coefficients attributed to each Walsh mode, p is the number of pixels and W is the number of Walsh modes ($p = W$).

$$\begin{pmatrix} \theta_1 \\ \theta_2 \\ \vdots \\ \theta_p \end{pmatrix} = \mathbf{H} \begin{pmatrix} \phi_1 \\ \phi_2 \\ \vdots \\ \phi_W \end{pmatrix} \tag{3.2}$$

It is important to note that the Walsh transformation is applied to the numerical phase values of the optical field ($\theta_1,\theta_2,\ldots$), while the modulation to the field is done using the complex equivalent ($e^{i\theta_1}$, $e^{i\theta_2},\ldots$).

The main advantage of using Walsh modes basis instead of the pixel basis, is that changing one coefficient is equivalent to a phase change across the entire optical field. Thus, changes in the output intensities are larger and measurement is easier to perform. It is important to note that the Walsh-Hadamard basis is by no means the only basis which has the properties of modulating a large area of the input field, however, due to the basis generation being readily available in MatLab, it has been chosen to be investigated.

In the next steps, the Walsh mode representation is applied to the optical field transmitted through a MMF. It will be shown that changing only one Walsh mode coefficient leads to a sinusoidal evolution of the intensity of a chosen output pixel. This is not a property specific to the Walsh modes, but rather to any modulation between two arbitrary wavefronts, where only the global phase of one of the wavefronts is changed. This property will be useful in creating an optimisation algorithm to correct the change of transmission through a bent fibre. Introducing the modulation, as described in equation 3.1, into the TM representation leads to the following equation, where $\mathbf{y}$ is the output field, $\mathbf{T}$ is the transmission matrix between the modulated field and the output field and $\mathbf{x_0}$ is the unmodulated input field:

$$\mathbf{y} = \mathbf{T}\mathrm{diag}(\mathbf{x_0}) \exp i\theta = \mathbf{T_{x0}} \exp i\theta \tag{3.3}$$

This is the general form of a phase-only modulation for the transmission of light through a MMF. This can alternatively be expressed using a Walsh mode representation, as defined using the form in equation 3.2, where ϕ_1,ϕ_2,... are the phase coefficients of the Walsh modes and $\mathbf{H}$ is the Walsh-Hadamard matrix.

As the target of the optimisation is a specific output, the next step is to focus on one output pixel (of index s), and focus equation 3.1 to the specific row of $\mathbf{T}$, associated with the chosen output. In the equations below, y_s is the output at pixel s, $(t_{x0})_{sk}$ is the element at position (s, k) in the matrix $\mathbf{T}\mathrm{diag}(\mathbf{x_0})$ and $(h)_{kq}$ is the element at position (k, q) in $\mathbf{H}$, the Walsh-Hadamard matrix. P is the number of pixels and W is the number of Walsh modes. While P and W are equal, they are still noted with different letters in order to differentiate between summation over pixels and summation over Walsh modes.

$$y_s = \sum_{k=1}^{P} (t_{x0})_{sk} \cdot e^{i\theta_k} \tag{3.4}$$

$$\theta_k = \sum_{q=1}^{W} (h)_{hq} \phi_q \tag{3.5}$$

$$y_s = \sum_{k=1}^{P} (t_{x0})_{sk} \cdot \exp\left[i \left(\sum_{q=1}^{W} (h)_{kq} \cdot \phi_q \right) \right] \tag{3.6}$$

Combining the TM expression for a specific output in eq. 3.4 with the sum expression of the matrix multiplication in eq. 3.2, reduced to a specific pixel as given in eq. 3.5, results in the form in eq. 3.6 which expresses a specific output in terms of the Walsh coefficients which form the modulation.

As described previously, the point of interest of Walsh mode optimisation is the evolution of the output pixel as a function of only one Walsh mode coefficient. Hence, the desired Walsh mode coefficient (of index v, coefficient ϕ_v) is extracted out of the summation in eq. 3.6 as the other terms are independent of this coefficient.

$$y_s = \sum_{k=1}^{P} (t_{x0})_{sk} \cdot \exp\left[i \left((h)_{kv} \cdot \phi_v + \sum_{q=1, q \neq v}^{W} (h)_{kq} \cdot \phi_q \right) \right] \tag{3.7}$$

$$y_s = \sum_{k=1}^{P} (t_{x0})_{sk} \cdot \exp\left[i \left(\sum_{q=1, q \neq v}^{W} (h)_{kq} \cdot \phi_q \right) \right] \cdot \exp[i \cdot (h)_{kv} \cdot \phi_v] \tag{3.8}$$

Addition in the exponential function in eq. 3.7 is expanded to multiplication of exponential functions in eq. 3.8. The first two elements of the multiplication in eq. 3.8 are constant with respect to Walsh coefficient ϕ_v. Thus, for simplicity, they can be collapsed into a general term z_k.

$$y_s = \sum_{k=1}^{P} z_k \cdot \exp[i \cdot (h)_{kv} \cdot \phi_v] \tag{3.9}$$

The next step is to make use of the property of a Walsh mode, that it contains a set of $+1$ and a set of -1 (h) terms. These can be separated into two summations (set of k_+ and set of k_- indices, which indicate the $+1$ and -1 terms, respectively), as it allows for the $(h)_{kv}$ terms to be substituted with $+1$ or -1, allowing for the exponent terms to be taken out of the summation, the final summations over k containing only the constant terms described before. The result in eq. 3.10 is only the sum of two terms, where the only variable is ϕ_v:

$$y_s = \sum_{k_+} z_{k_+} \cdot \exp[i \cdot (+1) \cdot \phi_v] + \sum_{k_-} z_{k_-} \cdot \exp[i \cdot (-1) \cdot \phi_v]$$

$$y_s = \exp(i \cdot \phi_v) \cdot \sum_{k_+} z_{k_+} + \exp(-i \cdot \phi_v) \cdot \sum_{k_-} z_{k_-}$$

$$y_s = \exp(i \cdot \phi_v) \cdot z_+ + \exp(-i \cdot \phi_v) \cdot z_- \tag{3.10}$$

The next steps to follow have the aim of proving the sinusoidal evolution of the output pixel intensity as a function of Walsh mode coefficient ϕ_v. The expression in equation 3.10 describes the evolution of the output pixel as a function of the coefficient of Walsh mode v. z_+,z_- are two complex numbers which arise from the summation and are dependent on the TM, non-corrected input and the coefficients of the other Walsh modes. The value of interest is the intensity of output y_s, which is independent of the global phase. Thus, the global phase reference value can be chosen such that the phases of z_+ and z_- are opposites in order to make the calculations simpler.

$$z_+ = |z_+| \cdot e^{i\rho}$$

$$z_- = |z_-| \cdot e^{-i\rho}$$

Substituting the new forms of z_+ and z_- into eq. 3.10 and solving for the output intensity leads to:

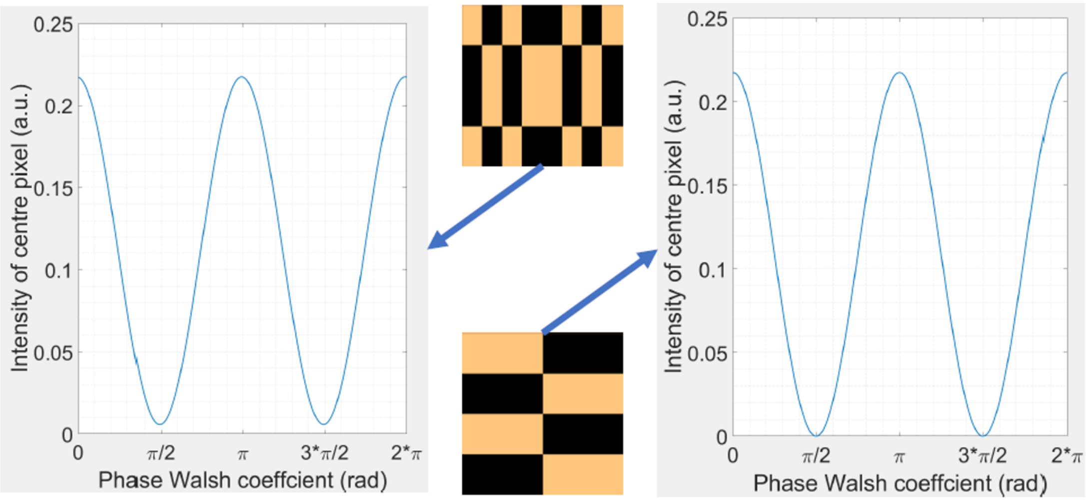

Figure 4: Simulated output intensity variation with respect to a Walsh mode coefficient. Modulation done at the proximal facet plane. The results illustrate the predicted sinusoidal variation.

$$
\begin{aligned}
y_s &= \exp(i \cdot \phi_v) \cdot |z_+| \cdot e^{i\rho} + \exp(-i \cdot \phi_v) \cdot |z_-| \cdot e^{-i\rho} \\
y_s &= (|z_+| + |z_-|) \cdot \cos(\phi_v + \rho) + i \cdot (|z_+| - |z_-|) \cdot \sin(\phi_v + \rho) \\
|y_s|^2 &= (|z_+|^2 + |z_-|^2) + 2 \cdot |z_+| \cdot |z_-| \cdot \cos[2(\phi_v + \rho)] \qquad (3.11)
\end{aligned}
$$

The equation above describes a sinusoidal evolution with fixed frequency (2 radians/Walsh mode coefficient), irrespective of fibre and input parameters, but variable offset ($OF = |z_+|^2 + |z_-|^2$), amplitude ($A = 2 \cdot |z_+| \cdot |z_-|$) and phase offset ($PH = 2\rho$).

$$|y_s|^2 = OF + A \cdot \cos(2\phi_v + PH) \qquad (3.12)$$

The sinusoidal evolution of the target intensity was verified using the simulation program and it is shown in figure 4 for two example chosen Walsh modes.

The derivation in this section of the chapter proved the sinusoidal evolution of the intensity of a chosen output location with respect to the variation of a single Walsh mode coefficient. The modulation was done at the proximal facet plane. However, the same applies for the modulation at the SLM plane as well.

It is assumed that the SLM is in the Fourier plane of the proximal facet. Thus, the propagation between the SLM and proximal facet planes can be described through the use of a Fourier transform. In finitely sampled square 2D planes (same number of samples in both dimensions), the Fourier transform can be described through the use of a matrix transformation. Specifically, $\mathbf{FT} = \mathbf{F}_{shift} \cdot (\mathbf{DFT}_P \otimes \mathbf{DFT}_P)$, where $\mathbf{FT}$ is the matrix describing the Fourier transform, $\mathbf{F}_{shift}$ represents the matrix describing the Fourier shift function applied to a 2D sampled plane, $\mathbf{DFT}_P$ represents the discrete Fourier transform matrix of size $P \times P$ (P being the number of samples along either dimension) and $\otimes$ being the Kronecker product.

The only change to the derivation in this subsection is that the matrix $\mathbf{T}_{x0}$ now is changed from $\mathbf{T}_{x0} = \mathbf{T} \cdot \mathrm{diag}(\mathbf{x}_0)$ to $\mathbf{T}_{x0} = \mathbf{T} \cdot \mathbf{FT} \cdot \mathrm{diag}(\mathbf{x}_0)$. Thus, the rest of the derivation is the same and the result is the same as well, though with different parameters (OF, A and PH).

3.3 Calculating and applying the correction

The target of the sensorless AO optimisation procedure in this case is to maximise the output intensity of a target pixel. Having described the form of the output intensity as a function of Walsh mode coefficient in the previous section, the next step is to calculate the required Walsh mode coefficient in order to maximise the output intensity. In order to maximise the output intensity, the coefficient ϕ_v has to be set to $\frac{-PH}{2}$, a value which needs to be determined.

As there are three unknown terms (OF,A,PH), at least three measurements are required to determine them. This approach is named phase-shifting interferometry. While three measurements are the theoretical minimum number, in practice, the optimisation procedure is susceptible to noise. Thus, optimisation procedures with a larger number of measurements have been created (see chapter 6.7 in [29]). However, introducing a larger number of measurements increases the time required for an iteration of the optimisation procedure, which leads to an overall increase in the total amount of time required for the procedure. Thus, the desired number of measurements will need to be chosen in practice based on a balance between the time required and the amount of noise. In this chapter, I limited the number of measurements to three, as the procedure is mostly intended to be used in a simulation environment where noise is not added.

In order to simplify the calculations, by working with simpler forms of the function, the three values to be measured are chosen as: $\phi_v = 0, -\frac{\pi}{4}, \frac{\pi}{2}$, which will result in three measurements I_1,I_2 and I_3 respectively.

$$I_1 = f(0) = OF + A \cdot \cos(PH) \tag{3.13}$$

$$I_2 = f(-\frac{\pi}{4}) = OF + A \cdot \cos(PH - \frac{\pi}{2}) = OF + A \cdot \sin(PH) \tag{3.14}$$

$$I_3 = f(\frac{\pi}{2}) = OF + A \cdot \cos(PH + \pi) = OF - A \cdot \cos(PH) \tag{3.15}$$

Using the three measurements the unknown variables can be calculated.

$$OF = \frac{I_1 + I_3}{2} \tag{3.16}$$

$$A = \sqrt{(I_1 - OF)^2 + (I_2 - OF)^2} \tag{3.17}$$

$$PH = \pm \cos^{-1}\left(\frac{I_1 - OF}{A}\right) \tag{3.18}$$

PH has a ± in its form because ‘cos’ is an even function. The correct sign is identical to the sign of $\sin(PH) = \frac{I_2 - OF}{A}$.

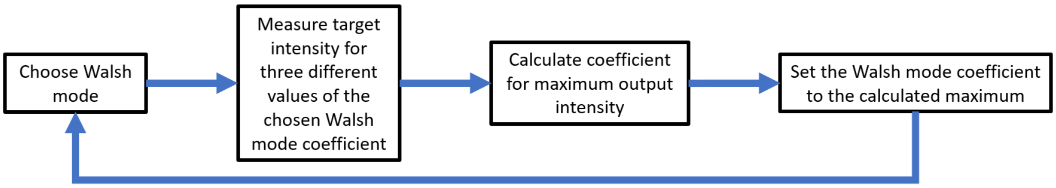

Figure 5: Diagram description of the steps undertaken in one Walsh mode correction iteration.

As the non-corrected case is when $\phi_v = 0$, on the sinusoidal function, it is assured that the correction will result in an intensity which is higher or, in the worst case, equal to the starting intensity. The procedure is then repeated in an iterative process for a chosen order of Walsh modes.

The advantage of this Walsh mode correction approach is that access to the distal facet is not required. If a reflector is placed at the target output location, maximising for the total reflected intensity is identical to maximising for the focus intensity at the reflector. The disadvantage is that the Walsh mode algorithm only corrects for one focus. However, the correction can be extended from one location, through the use of memory effect, discussed in more detail in chapter 4.

3.4 Simulating the Walsh mode optimisation

3.4.1 Methodology

While the Walsh modes represent an orthogonal basis for representing the phase modulation applied by the SLM, the order the Walsh modes are iterated through has an effect on the optimisation result.

The SLM in the optical system is a liquid-crystal phase-only type and has a resolution of 512 × 512 pixels. However, for the simulation smaller sizes have been used. Initially, a set of 4096 Walsh modes were used (64 × 64), then this was later extended to a set of 16384 Walsh modes (128 × 128). Smaller sizes of

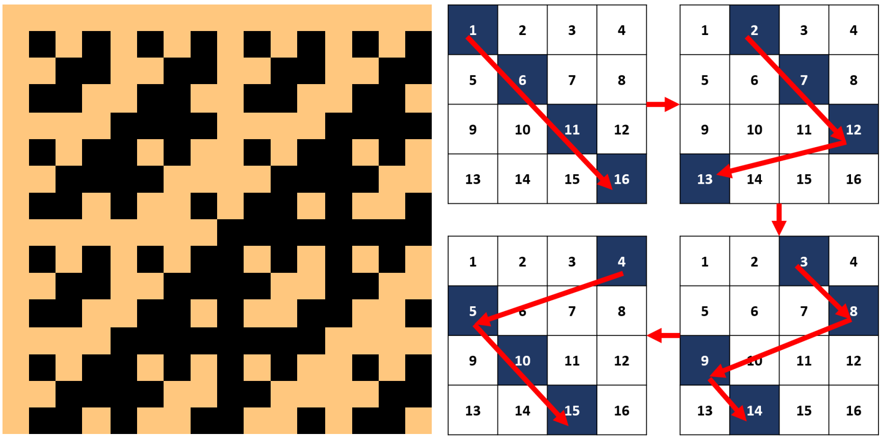

(a) Image of a 16×16 Hadamard matrix. Each column/row is a Walsh mode of size 4×4. Black represents -1 and brown represents +1.

(b) Diagram showing the diagonal permutation used in the Walsh mode optimisation simulations. The numbers represent the Walsh mode indices.

Figure 6: The Walsh modes were generated in natural order. Three permutations were used in the simulations. The diagonal permutation is illustrated here.

Walsh modes can be used on the SLM, as tiling the SLM can easily be done (i.e. 64×64 Walsh modes can be used on a 512×512 SLM, by expanding each pixel of the Walsh mode to a 8×8 size tile on the SLM).

The base order of the Walsh modes used is the natural (or Kronecker) order. This was generated with the use of the "hadamard" function in MatLab. While it is not specified in the description of the function, this order is usually generated through a recursive process. An illustration of the Hadamard matrix in the natural order is given in figure 6a.

Three permutations were simulated: the original order of the modes, a "diagonal" permutation and a random permutation. The diagonal permutation was generated by iterating along the main diagonals of the matrix of indices, as shown in figure 6b. The motive for choosing the permutation is in order to try to limit any decrease in optimisation efficiency due to similarities which might arise between Walsh modes which are either consecutive in the original order or $\sqrt{\text{Number of Walsh modes}}$ indices apart (i.e. a supposed order along the columns of the indexes matrix), due to symmetries in their profile. The random permutation was obtained by using the function "randperm" in MatLab.

The parameters of the simulation were: light wavelength of 488 nm, a core diameter of 50 μm, a core refractive index of 1.45, NA of 0.22 and a fibre length of 1.5 cm. The window size was set to 62.5 μm x 62.5 μm (2.5 x core radius).

The target of the optimisation was chosen at close to the edge of the fibre core (0.9 x core radius). This was chosen such that the focus location is generated by a larger number of fibre modes.

The SLM pattern for the generation of a focus at the desired location through a straight fibre (inverse radius of 0 m^{-1}) was used as the starting point of the optimisation process. The correction was repeated for a set of inverse bending radii: $\{0.5, 1, 2, 3, 4, 5, 7.8, 8.6, 9.2, 10, 12.5, 15, 17.5, 20, 25, 30, 35, 40, 45, 50\}$ m^{-1}. More samples were used for smaller bends.

Working with the inverse bending radius is easier than with the bending radius itself, as the straight fibre case is represented at 0 m^{-1} rather than ∞ m, thus, facilitating both the calculations involved in the simulation as well as plotting the data.

3.4.2 Results

The first step in the simulation process was to observe the achievable intensity if a classic phase-only calibration is used, as described in section 2.3.4, assuming the amplitude at the SLM is uniform. The SLM is assumed to be in the Fourier plane of the proximal facet. Thus, the propagation from the SLM plane to the proximal facet plane is simulated by using an inverse 2D Fast Fourier Transform (FFT).

First, the TMs for the different bending inverse radii were computed. Starting with a delta function at the distal facet (1 at the focus location and 0 everywhere else) and back propagating through the fibre, using the TM inverse, the desired optical field at the proximal facet was computed. A 2D FFT was then applied to the desired proximal field to find the desired SLM plane optical field. As mentioned previously, the amplitude of every pixel in the SLM plane was set to 1 and the phase information was kept. This is the full correction SLM field.

The first result to be computed was the full correction output intensity of at the target location. This was done by forward propagating the full correction SLM field.

The first results are in figure 11

The results are in figure 7. The intensity varies at different inverse bending radii, however, the variation is on the order of 1%, which is most likely due to variations in the amount of light coupling into the fibre and numerical error. These values were later used as normalisation for the optimisation process results.

Next, the optimisation process for the 64×64 size Walsh modes was simulated. This process was repeated for all inverse bending radii. Three examples are given in figure 8. The first apparent observation is that the different permutation perform differently, as expected. furthermore, the general evolution for all permutations is that there is larger improvement at the start of the optimisation process, which reduces over in the latter stages.

Another value of interest which can be plotted, is the enhancement factor. This value is defined as the ratio between the output pixel intensity and the total energy, being a good measure of the focus quality. Figure 9a plots the resulting enhancement factor and normalised pixel intensity as a function of iteration number. It is clear that the plot approximately follows the same envelope, but with a variable scaling. Thus, in figure 9b the ratio between the enhancement factor and the normalised pixel intensity is shown. In terms of what this ratio means, it is $\frac{\text{pixel intensity}}{\text{total energy}} / \frac{\text{pixel intensity}}{\text{fully corrected pixel intensity}}$. Thus, as the fully corrected pixel

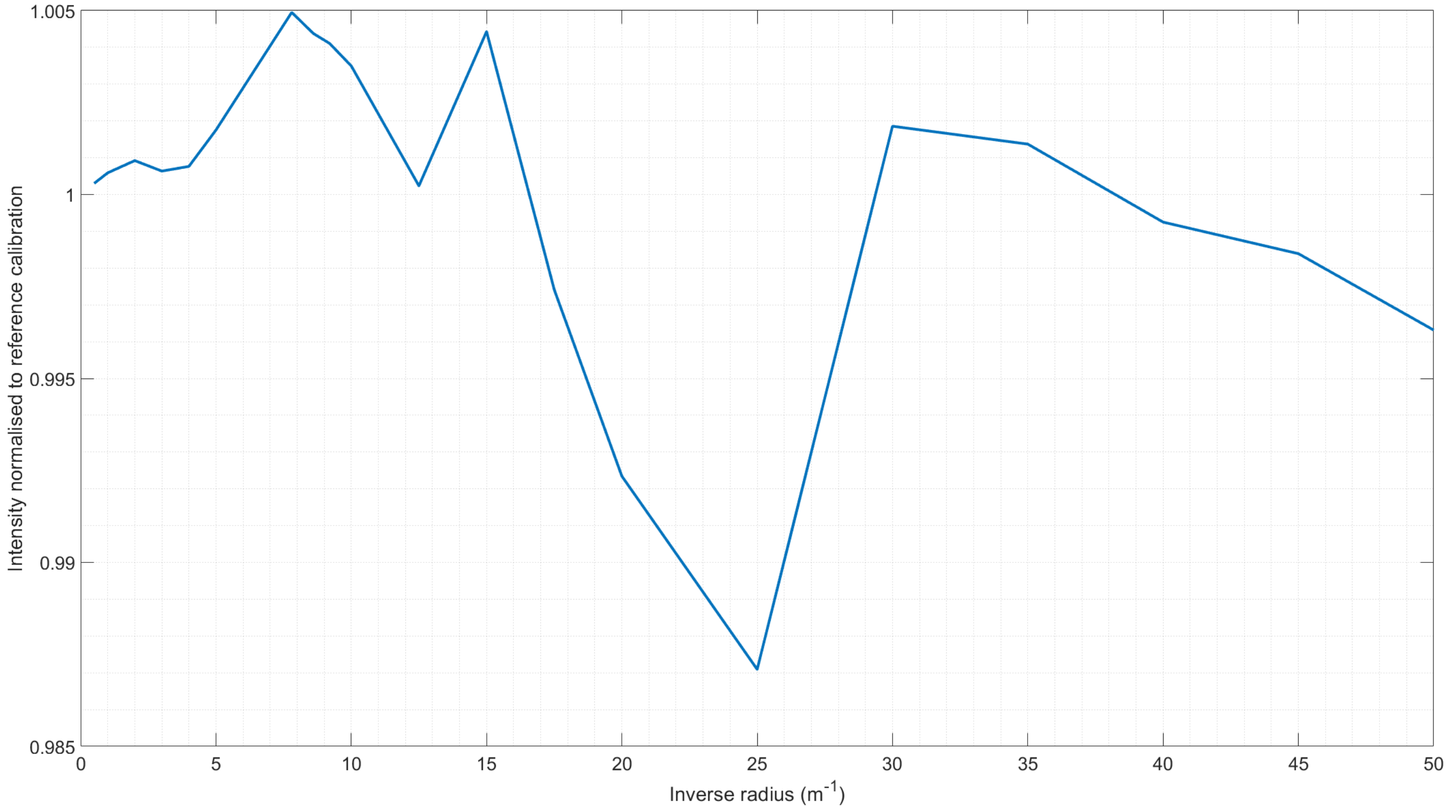

Figure 7: The output intensity of at the target location normalised to the straight fibre case for different inverse bending radii.

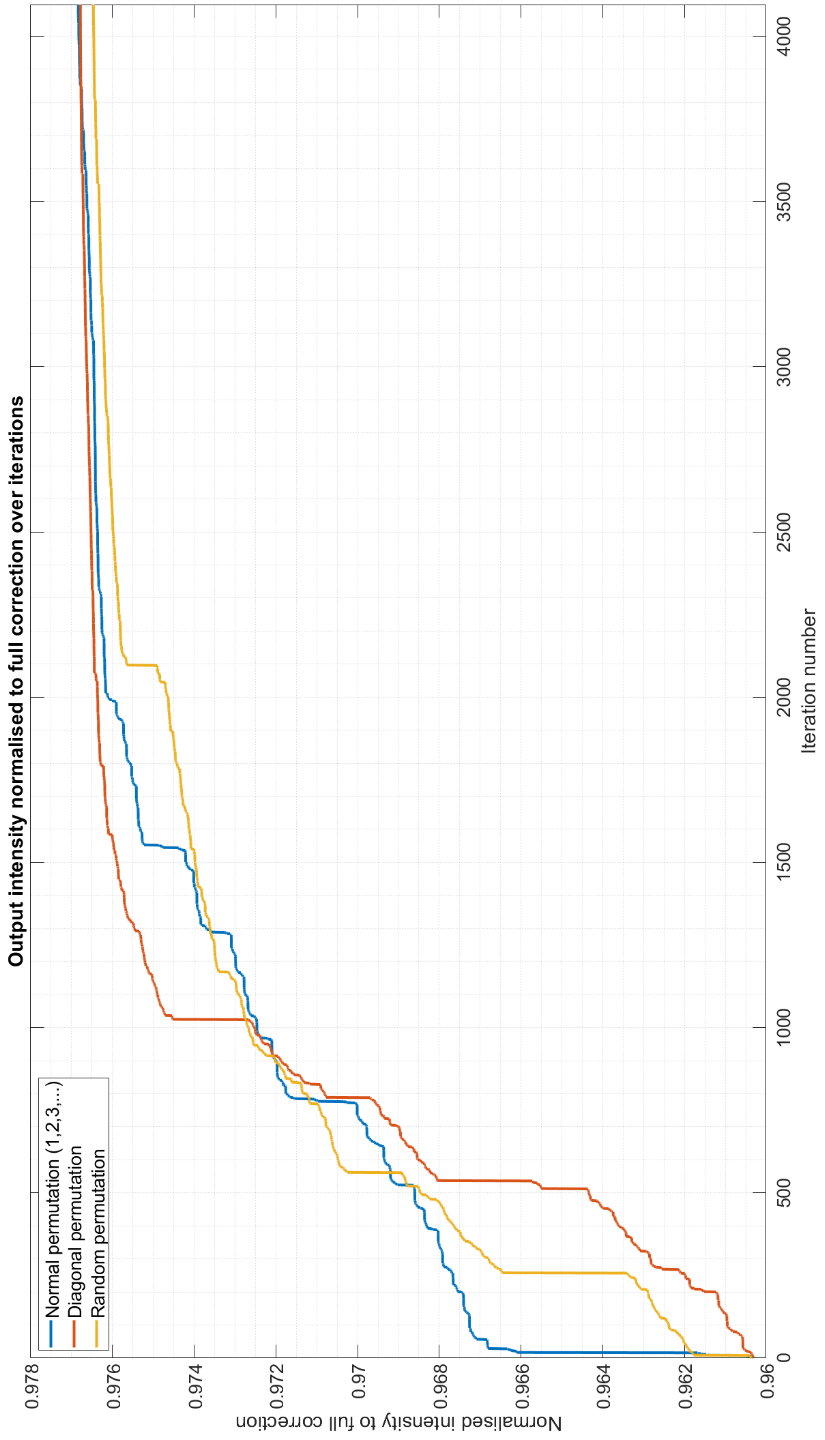

(a) Inverse radius: $2\ \mathrm{m}^{-1}$

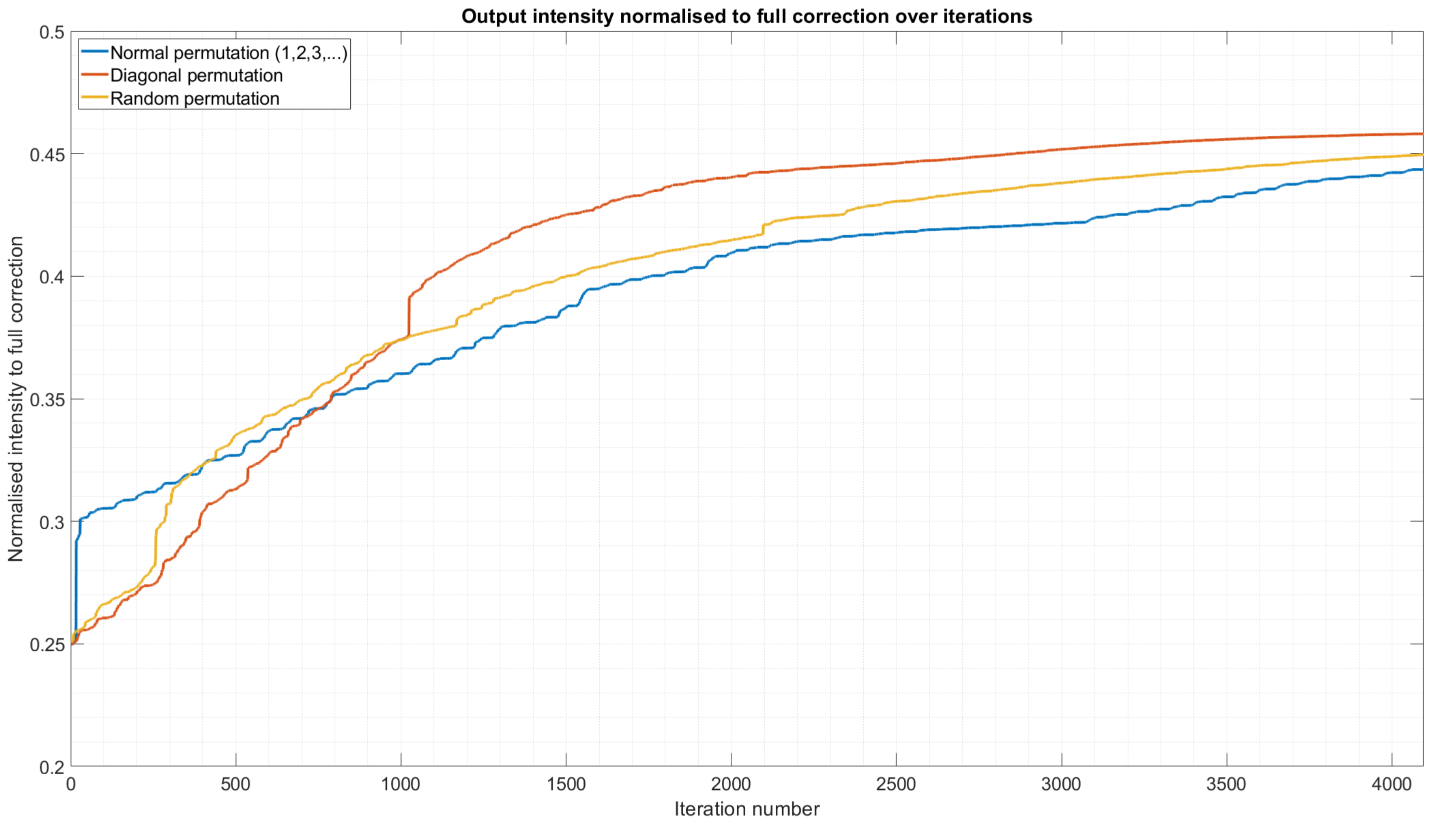

(b) Inverse radius: $12.5\ \mathrm{m}^{-1}$

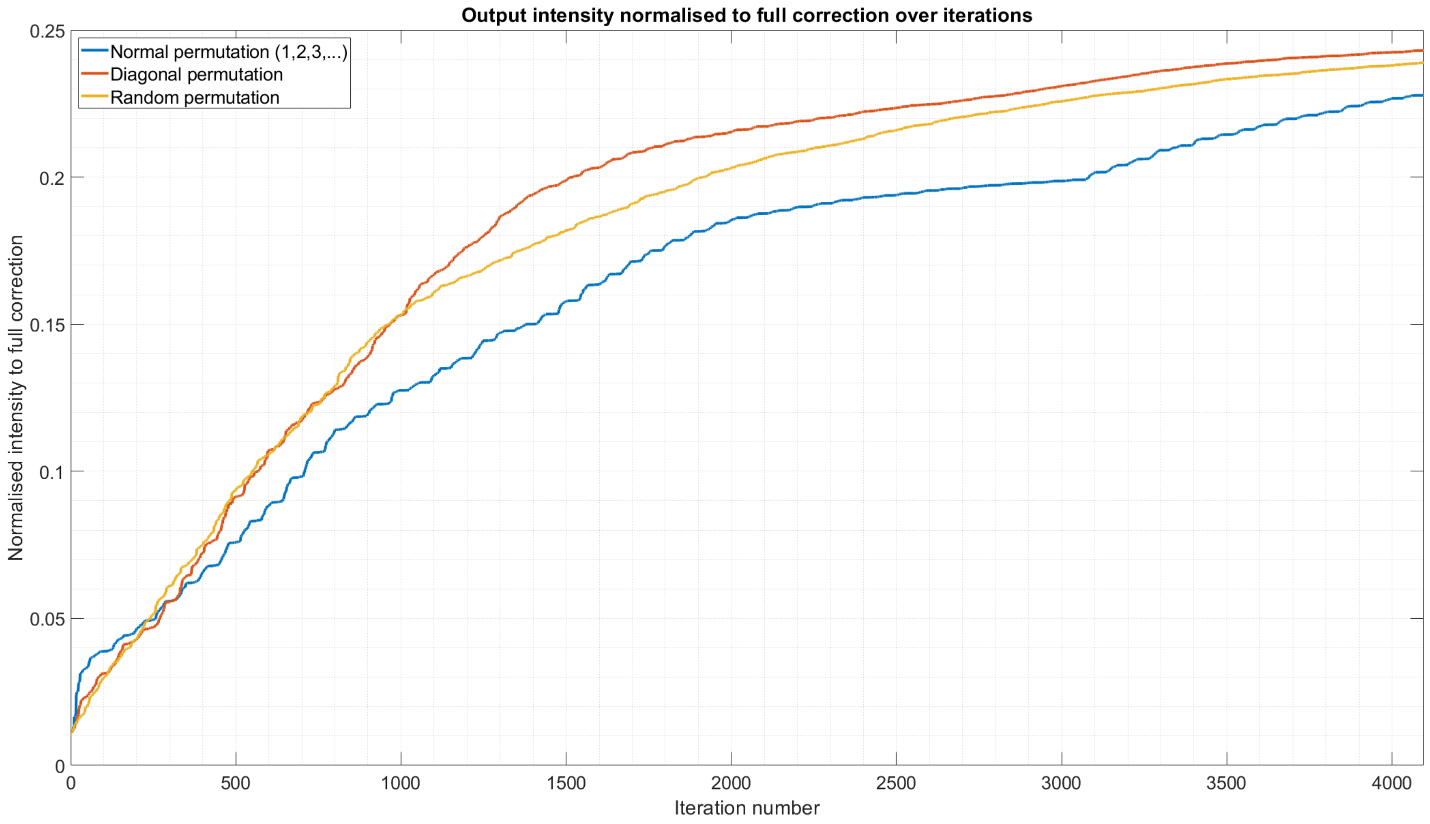

(c) Inverse radius: 30 m^{-1}

Figure 8: Intensity evolution at the target output location normalised to the full correction value, over the Walsh mode optimisation process's iterations. Results for different inverse radii.

intensity is a constant and the variable pixel intensity terms cancel, the ratio represents an inversely-proportional envelope of the total energy in the output optical field. As this value increases with iteration number, is signifies that with added Walsh mode modulation, the total energy in the output field decreases up to a point where it plateaus. Thus, the amount of light which couples into the fibre decreases with added modulation. This is an important results to consider, as, while the focus quality increases with respect to the background, the total amount of light coupled into the fibre decreases.

Figure 10 shows the final intensity achieved at the output target location after the optimisation process. To better illustrate the amount of correction, the initial intensity was also plotted with a dashed black line. As expected, the initial non-corrected intensity decreased with a larger bend. However, the optimisation procedure had better results for larger bends. In the worst case investigated the normalised intensity increased from almost 0% to 20% and 45% for the 4096 and 16384 iterations cases, respectively. This is a drastic improvement. Furthermore, it seems that the amount of improvement plateaued, thus, larger and larger bends do not negatively impact the final result of the optimisation procedure.

Another observation is that while continuing with the optimisation process by re-iterating through the permutation did increase the final intensity result, the change is not as much as using larger Walsh modes. This is to be expected, as larger Walsh modes have higher dimensionality, which covers the SLM field space better. Thus, if a larger number of iterations are necessary, it is better to increase the size of the Walsh modes, rather than repeat the iterations with smaller Walsh modes. Though, this is limited by the size of the SLM.

A final observation is that the original permutation performed worse, while the other two permutations performed similarly. Thus, while the diagonal permutation might not be the best option, and an investigation into which is the

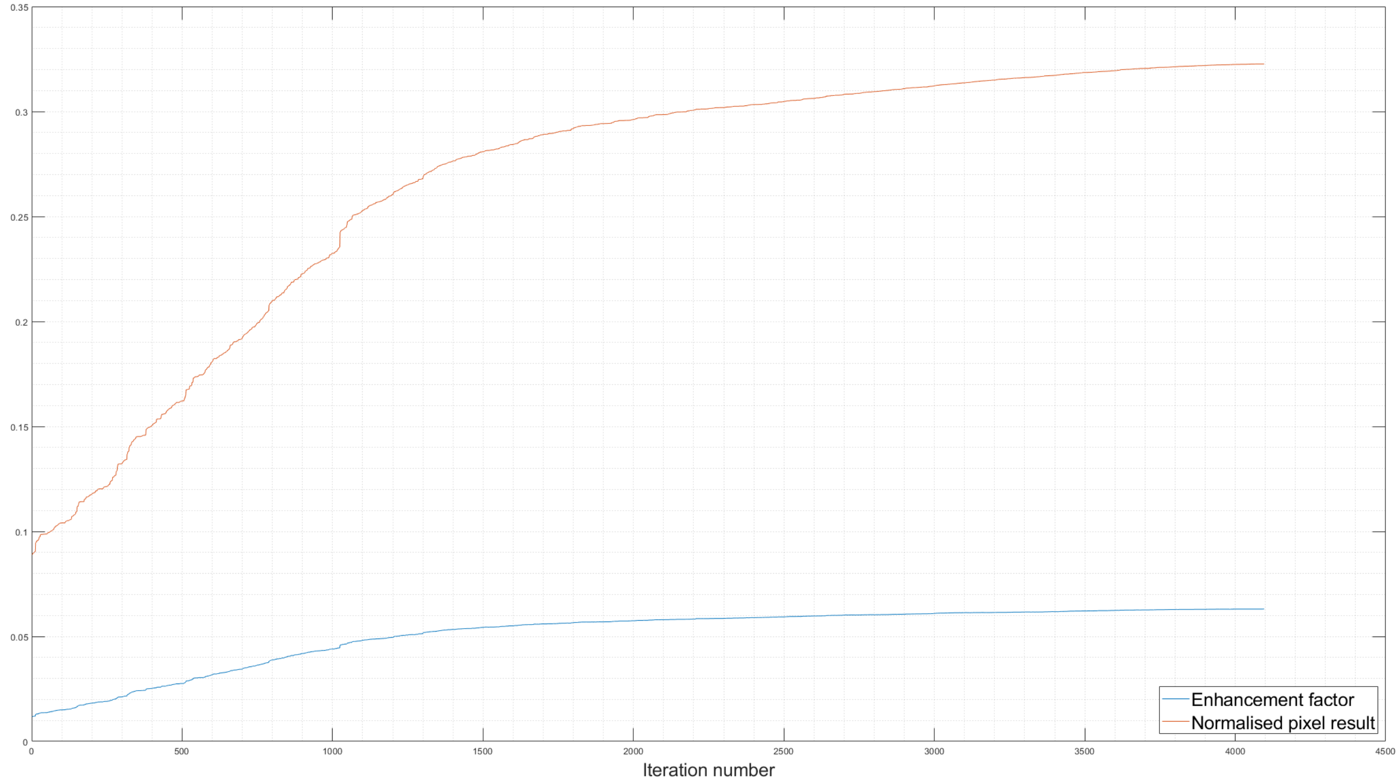

(a) Plots of enhancement ratio and the normalised output pixel intensity.

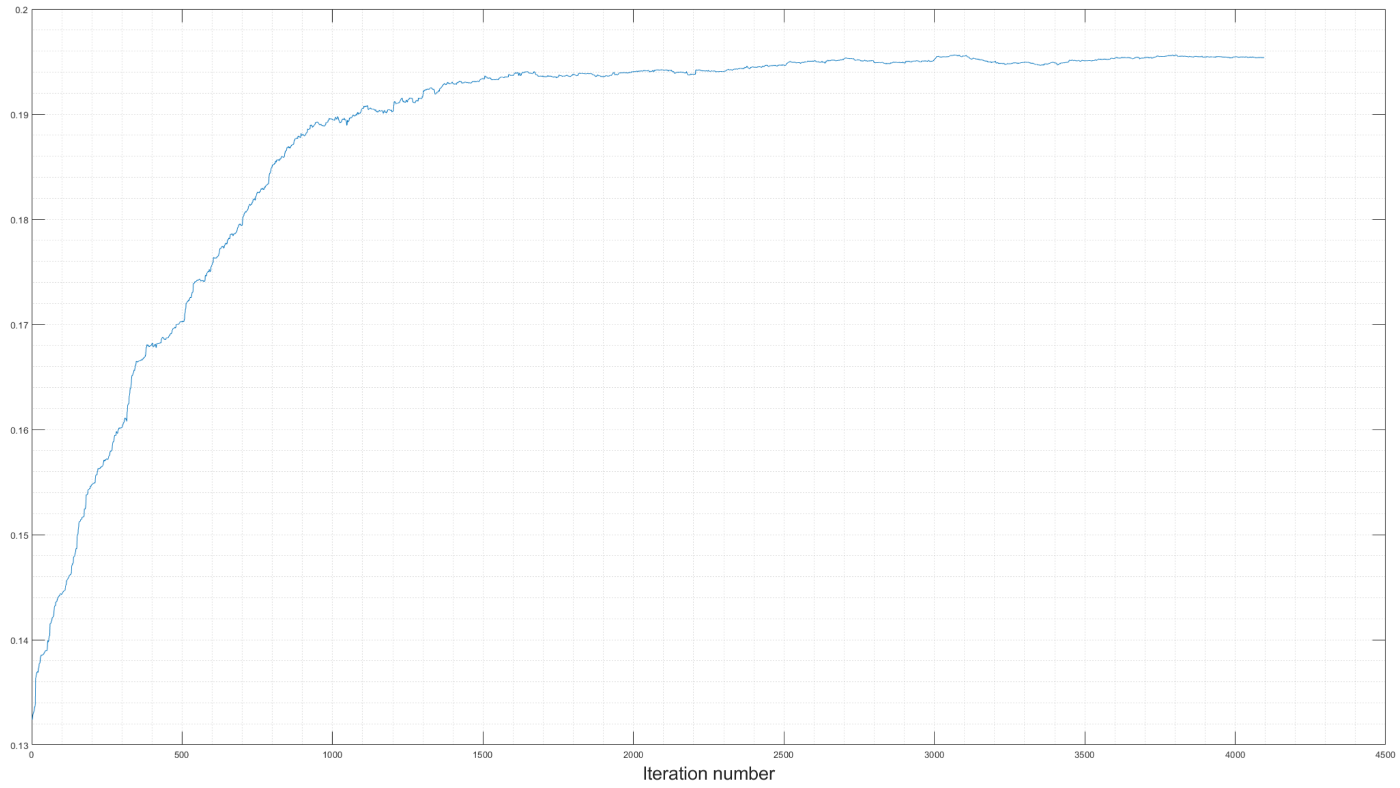

(b) Plots of the ratio between the enhancement ratio and the normalised output pixel intensity.

Figure 9: Comparison between the enhancement ratio and the normalised output pixel intensity. Data generated for a inverse bending radius of 18.25 m^{-1} using an optimisation with 4096 iterations of 64x64 size Walsh modes. First subfigure plots both evolutions as a function of iteration number. The second subplot, plots the ratio between the enhancement factor and iteration number as a function of iteration number.

best permutation might be desirable, it is a good choice.

Finally, a comparison of the foci before bending, after bending with no correction and after correction is given in figure 11 for the case of optimising with Walsh modes of size 128x128 over 16384 iterations at an inverse radius of 18.25 m^{-1}.

3.5 Experimental results

The Walsh mode optimisation process was implemented into the optical system described in section 2.3.8.

The modulation on the SLM is being controlled thorough the use of a graphical processing unit (GPU), through the use of a Cuda and OpenGL program. Thus, loading the entire Hadamard matrix into the memory of the GPU would be inefficient, as this matrix increases quadratically with respect to the size of the Walsh modes. Thus, each Walsh mode was generated as needed using a Cuda kernel, taking full advantage of the parallelisation strength of a GPU.

Starting from the recursive process of generating a Hadamard matrix, a specific formula for an element of the Hadamard matrix of size 2^mx2^m is found [30] in equation 3.19, where i and j are the row and column indices of the element, i_k and j_k are the bits in the bit-wise (base 2) representation of i and j and k is a bit order index.

$$(\mathbf{H}_{2^m})_{i,j} = (-1)^{\sum_k i_k j_k} \tag{3.19}$$

For example, for element (7,12) [element (0111, 1100) in base 2] in a 16x16 Hadamard matrix, $\sum_k i_k j_k = 0 \cdot 1 + 1 \cdot 1 + 1 \cdot 0 + 1 \cdot 0 = 1$, thus, the element is $(-1)^1 = -1$.

In terms of the algorithm, knowing the index of the Walsh mode generated (j) and the pixel index (i), which can be found from the 2D coordinates of the pixel,

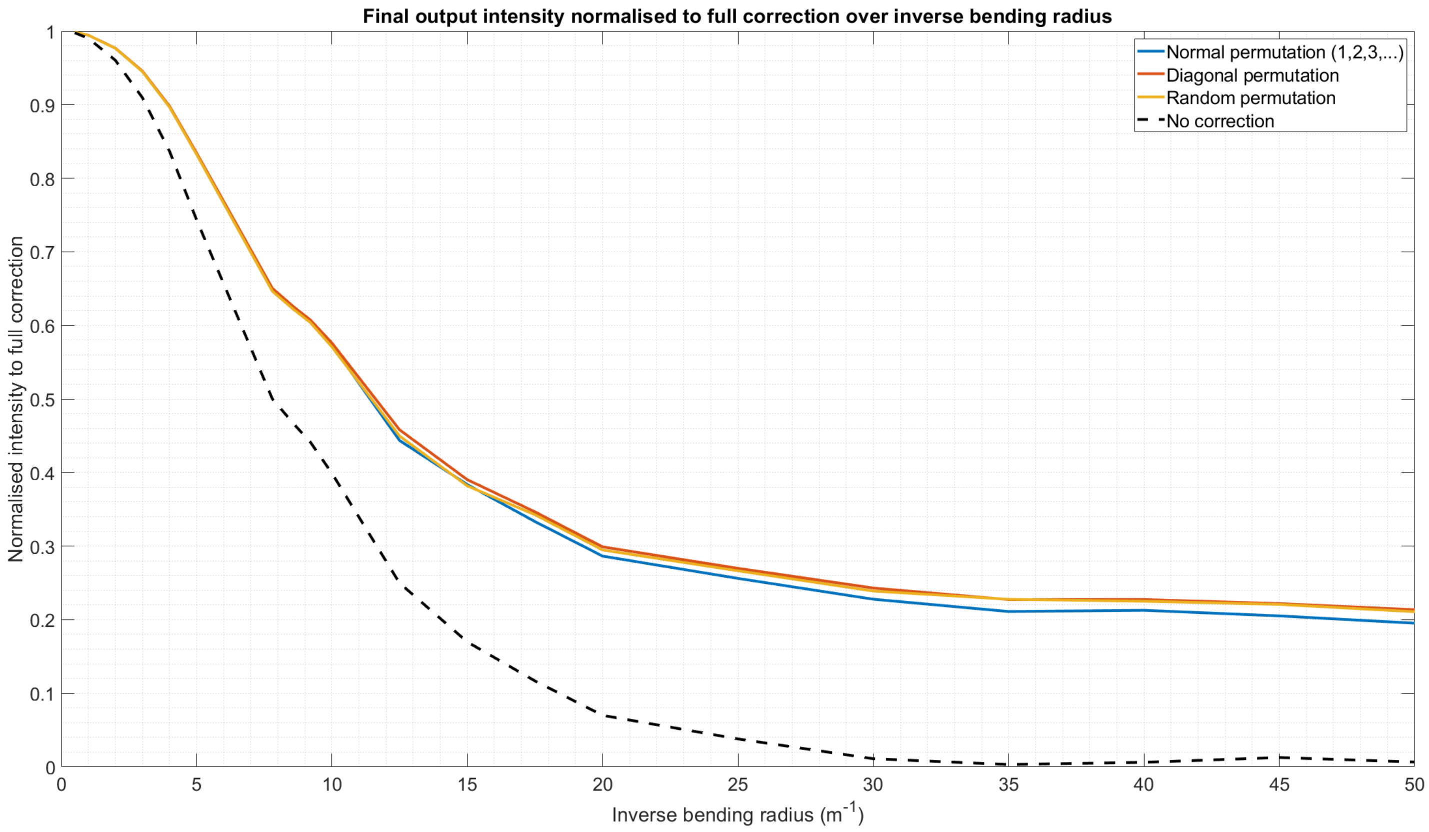

(a) 4096 iterations of the 64x64 Walsh modes

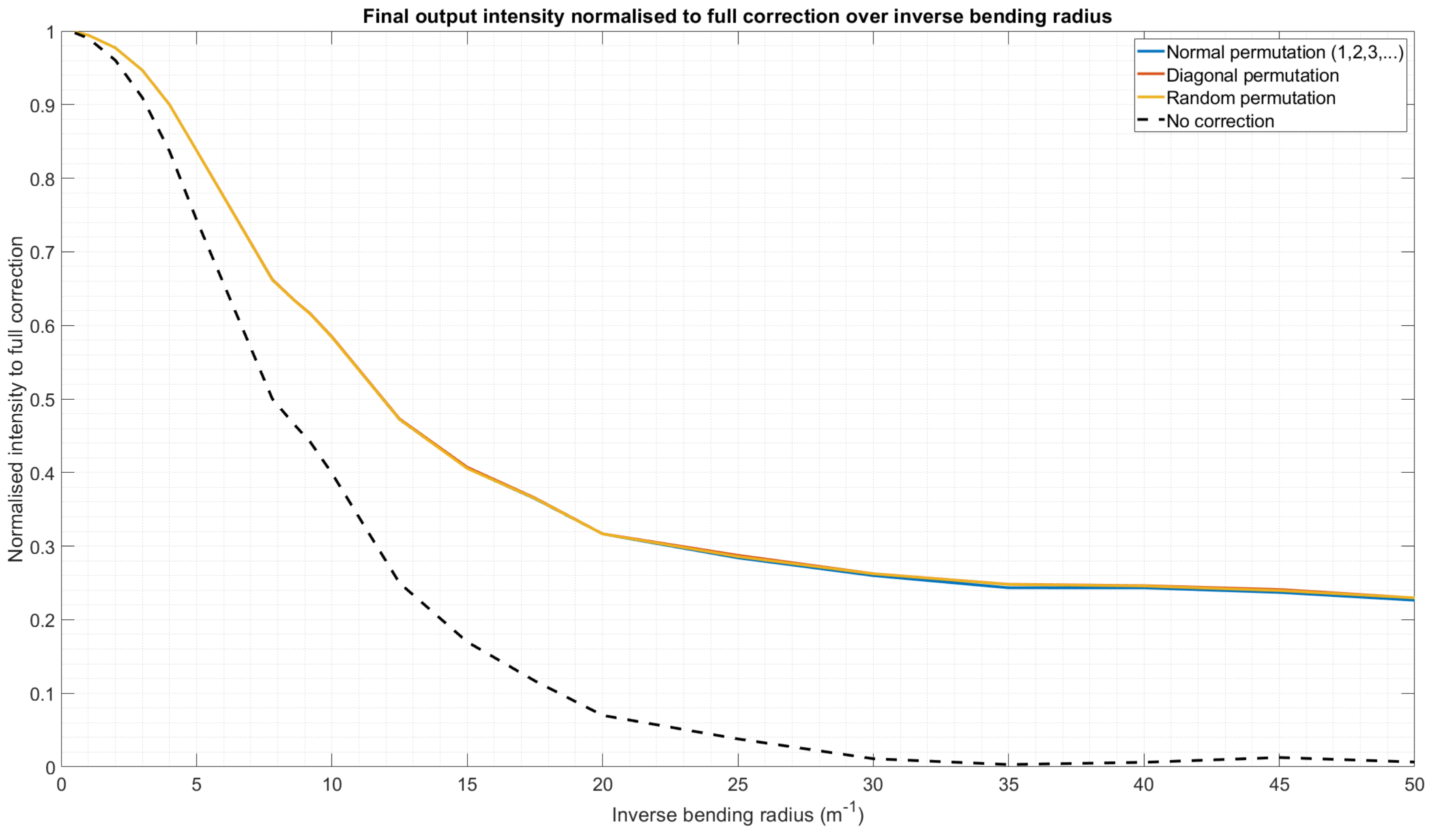

(b) 16384 iterations of the 64x64 Walsh modes

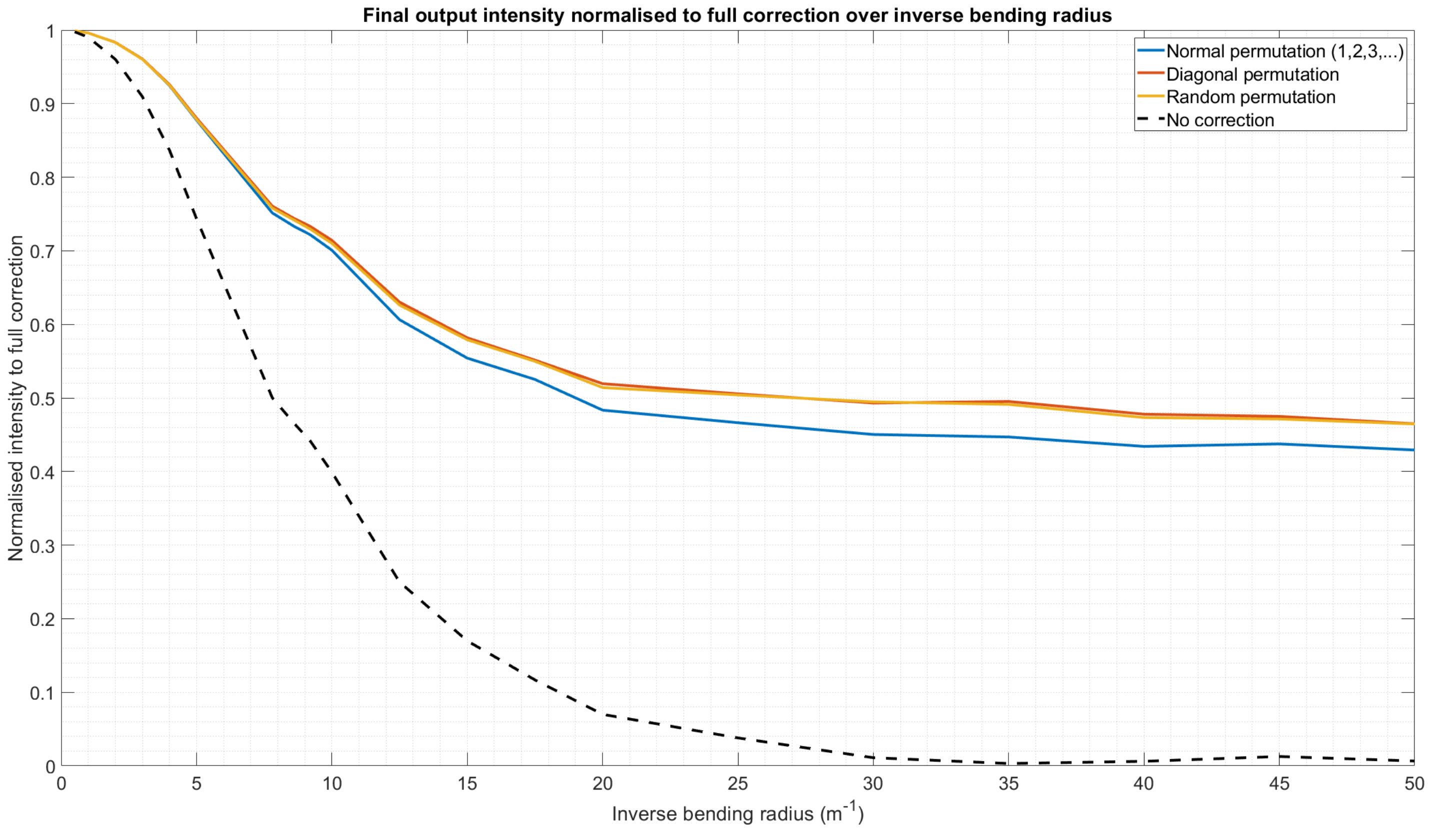

(c) 16384 iterations of the 128x128 Walsh modes

Figure 10: Final output intensity after the optimisation normalised to full correction intensity as a function of inverse bending radius. Dashed black line represents the intensity at the start of the operation.

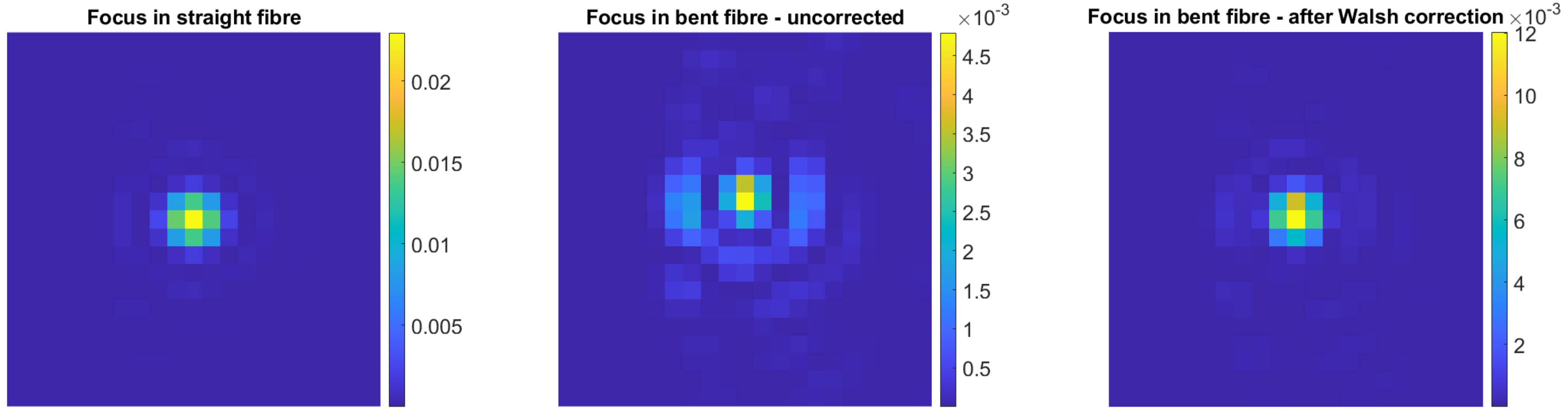

Figure 11: The achieved focus with a straight fibre, with a bent fibre but no correction (same input as in the straight fibre case) and after 16384 iterations of the Walsh correction algorithm with a Walsh mode size of 128x128. The intensity is in arbitrary units and only a crop around the focus is shown.

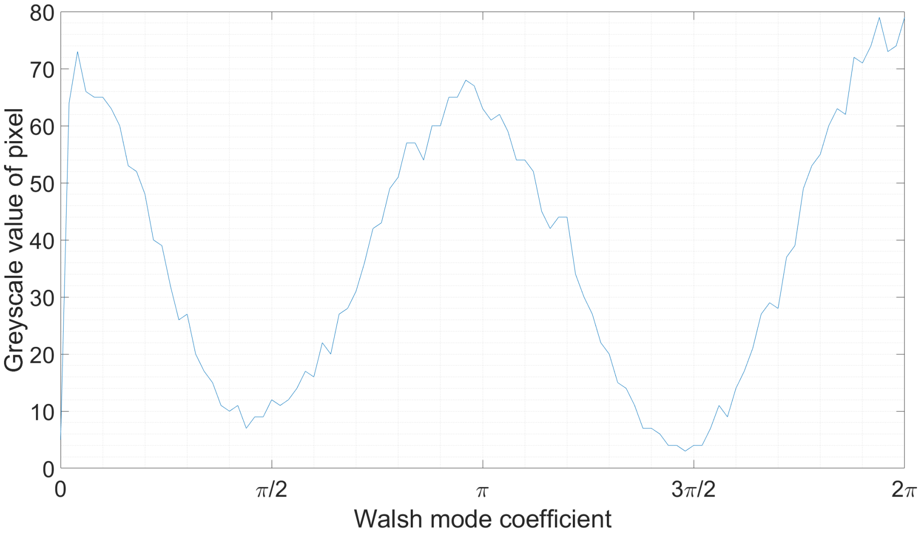

Figure 12: The output intensity of at the target location as a function of a single Walsh mode coefficient. The chosen Walsh mode had index 5.

the value its associated element in the Walsh mode can be readily computed. The kernel was implemented to compute the value of each Walsh mode element in parallel.

The experiment started by calibrating the fibre and choosing a target pixel. The SLM field which generates the focus, calculated based on the calibration results, was used as a base phase modulation field to which the Walsh mode phase modulation was added. The calibration was done to a subpar standard in order to start from an unoptimised focus. The experiment only used the 64×64 size Walsh modes.

The first experiment was to check the sinusoidal evolution of a target output intensity as a function of a single Walsh mode coefficient. The Walsh mode chosen had index 5, however, this evolution appears for any Walsh mode, except the first, which represents only a global change in phase and leads to no change in amplitude (technically, this is a sinusoidal variation with amplitude 0).The results are shown in figure 12. While there is some noise, the sinusoidal variation is apparent.

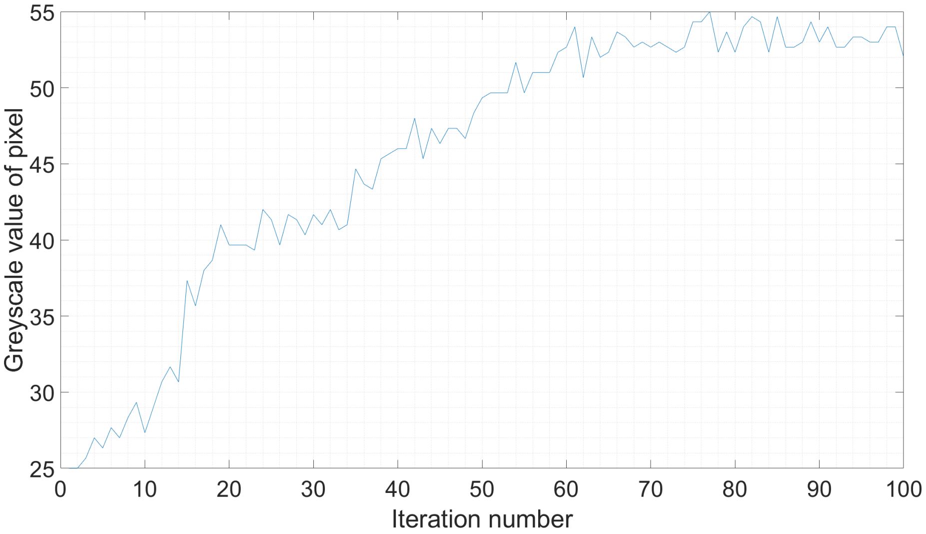

Figure 13: The evolution of output intensity of at the target location over the iterative Walsh optimisation process.

The second experiment was to apply the Walsh mode optimisation procedure. The modes were iterated in the original order. At every iteration, in order to limit noise, three acquisitions are made for each measurement and the result used is the average value. Unfortunately, due to instabilities in the optical system control software, only 100 iterations were able to be computed. However, even 100 iterations clearly show an improvement in intensity, whose rate decreases with larger number of iterations. An observation to be made is that in the real system, unlike the simulations, the intensity does not increase at every single iteration. This was most likely due to noise, thus more measures would be needed to minimise it, especially as the number of iterations increases, as the amount of improvement decreases. Though, at some point the grayscale resolution of the camera will become a limitation.

3.6 Conclusion

The sensorless adaptive optics approach provides a means to recovering focusing capabilities at a desired location at or near the distal facet plane. The approach only requires that the intensity of the focus at the target be measured and the input field be modulated in phase in its Fourier plane through the use of a modulator such as an SLM. The approach was shown, through simulations, to be able to recover a large factor of the lost intensity in the focus due to bending of the optical fibre. However, in order to do so, a large number of iterations are needed, which depending on the application might not be desirable, as the time required for the optimisation to be completed is long.

In conclusion, while it has some limitations, the sensorless approach to recovering a focus at the output of the fibre is a feasible approach, though, it could be improved or replaced with a faster method.

4 Expanding the optical field control using the Memory Effect and free-space propagation

4.1 Memory Effect

This chapter describes the memory effect and its use in expanding the area of control from the reflector location to an isoplanatic patch around it.

The term "memory effect" describes in the optical field, a correlation in terms of tip and tilt in coherent fields. This correlation allows for a some amount of control even after the light undergoes limited scattering, as any tip or tilt modulated into the input light will result in a similar tip and tilt in the output scattered light.

In the area of fibre optics, the general memory effect is less apparent, due to cylindrical boundaries the geometry of an optical fibre introduces. As shown in [2] while limited azimuthal control can be achieved, it is not the case radially, without negatively affecting the output pattern. A different approach, also named memory effect (ME), described in the same publication [2], works by assuming that the TM of a slightly bent fibre remains diagonal, though the phase of the diagonal elements can change. This could be considered a TM memory effect, as the diagonal form of the TM remains with phase-only diagonal elements, while the bending is assumed to only introduce small phase changes in the diagonal elements.

In order to describe the memory effect mathematically and make use of it for bending compensation, the derivation starts with the relationship $\mathbf{y} = \mathbf{T}_{bent}\mathbf{x}$ being expanded into a set of equations for each respective element in the column vectors:

$$y_k = e^{i\phi_k} x_k \tag{4.1}$$

The reason the diagonal elements of the assumed TM have an amplitude of 1 is due to the requirement of the TM being unitary, such that the total energy of the optical field is maintained. The useful property of a diagonal TM is that the diagonal elements can be calculated while only knowing a single pair of $\mathbf{x}$ and $\mathbf{y}$. This allows for the entire assumed TM to be calculated after generating a single focus.

A perfect focus can be described as the projection of a delta function into the modal space:

$$\mathbf{y}_{focus} = \mathbf{\Psi}^{\dagger}\mathbf{\Delta}_h \tag{4.2}$$

where † represents the complex conjugate and

$$\mathbf{\Delta}_h = \begin{pmatrix} \delta_1 \\ \delta_2 \\ \vdots \\ \delta_P \end{pmatrix}$$

$$\delta_j = \begin{cases} 1, & \text{if } j = h \\ 0, & \text{if } j \neq h \end{cases} \tag{4.3}$$

Thus, by expanding the matrix multiplication in 4.2 and, using the definition of $\mathbf{\Delta}_h$ above, the coefficient of a specific fibre mode of index k in the output field can be computed, where $*$ represents the complex conjugate:

$$y_k = \psi^{\dagger}_{k,h} = \psi^{*}_{h,k} \tag{4.4}$$

If a focus has been generated at the DF, then the input optical field $\mathbf{x}_{c,focus}$ which generates said focus can be projected into the fibre mode space to obtain $\mathbf{x}_{focus}$. Then the phase diagonal elements of the assumed TM can be determined:

$$\begin{aligned}\phi_k &= \mathrm{Arg}(y_{focus,k}) - \mathrm{Arg}(x_{focus,k}) \\ &= \mathrm{Arg}(\psi^*_{h,k}) - \mathrm{Arg}(x_{focus,k}) \\ &= -\mathrm{Arg}(\psi_{h,k}) - \mathrm{Arg}(x_{focus,k}) \qquad (4.5)\end{aligned}$$

4.2 Simulating the memory effect

4.2.1 Methodology

As the memory effect approach is based on the assumption that the bent fibre TM is diagonal, it is expected that memory effect's correction ability is dependent on how close the actual bent fibre TM is to a diagonal matrix, a property which can be characterised through the measurement of diagonal energy:

$$D_{energy} = \frac{\sum_{j=1}^{j=N} |t_{j,j}|^2}{\sum_{j=1}^{j=N} \sum_{k=1}^{k=N} |t_{j,k}|^2} \qquad (4.6)$$

This parameter characterises the amount of energy which is kept within modes rather than being coupled out. In the case of the straight fibre TM, which is diagonal, the diagonal energy is 1 (or 100%).

Simulations have been undertaken for an MMF using the following parameters:

- Wavelength: $\lambda = 488$ nm
- Core diameter: $d = 50\ \mu$m
- Core refractive index: $n_{core} = 1.45$
- Numerical aperture: $NA = 0.22$
- Fibre length: $L = 1.5$ cm

These parameters are in line with the fibre that was used in the experimental system. Bending has been modelled as a constant curvature, parameterised through the use of the inverse bending radius ρ. The reason for using the inverse radius is such that a straight fibre is represented by a value of 0 m^{-1} and not ∞ m, allowing for better numerical precision in simulating small bends.

While the desired input field at the proximal facet was computed by inverting the modal space TM, the actual input optical field was computed by back-propagating the desired field into the Fourier plane (the SLM plane) and extracting only the phase information (division with the absolute value) before propagating back into the proximal facet plane. This approach strives to better simulate the real-case scenario, where the input optical field is controlled through the use of a phase-only modulator (SLM).

4.2.2 Results

Figure 14 shows the plot of the diagonal energy as a function of inverse bending radius. As expected, as the bending increases, the amount of coupling between the modes increases, leading to a lower diagonal energy parameter.

The isoplanatic patch represents the area in which focus correction using memory effect approaches the ideal case achievable by recalibrating the entire TM. More specifically, a good threshold would be the area in which through the memory effect the focus generated using the assumed TM reaches 70% of the intensity of a focus generated using the actual TM of the bent fibre. In order to observe the effect of bending on the size of the isoplanatic patch, six inverse radii were chosen to be simulated. The results are shown in figure 15. It is clear from figure 15 that as bending increases, the isoplanatic patch decreases in size as expected.

The location of the reflector was chosen at a radius of $\frac{0.9 \cdot d}{2}$. The reason for

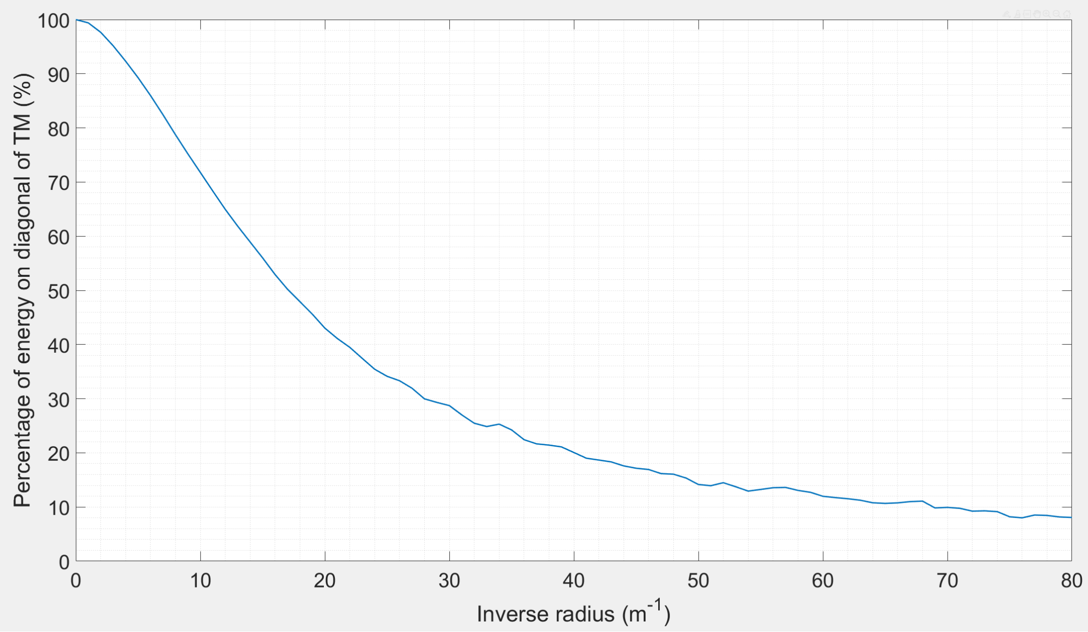

Figure 14: Diagonal energy as a function of inverse bending radius

the location being close to the edge of the facet is due to the requirement that for a good correction, the reflector needs to be in a position where it samples most, if not all, of the fibre modes. The field distributions of higher order fibre modes will have the largest amplitude close to the facet edge, while almost none close to the centre. In the case of lower order modes, while the amplitude is larger closer to the centre, they will also have a number of lobes at a larger radial position. Thus, they will also be sampled by a reflector closer to the edge.

The reason for this mode profile field distributions is due to higher order modes having a profile defined by a higher order Bessel function of first kind (J_n). The field distribution of a fibre mode inside the fibre core follows the function: $AJ_l(hr)e^{il\phi}$, where A is a normalisation parameter, $h^2 = n_{core}^2 k_0^2 - \beta^2$ is a radial magnification parameter dependent on the propagation constant of the mode, l is the azimuthal index of the mode and r and ϕ are the polar coordinates. The higher the order of a Bessel function of first kind, the further from 0 (the centre) the first peak occurs, thus, as the order l of a mode increases, the resulting energy is being concentrated closer to the core facet edge.

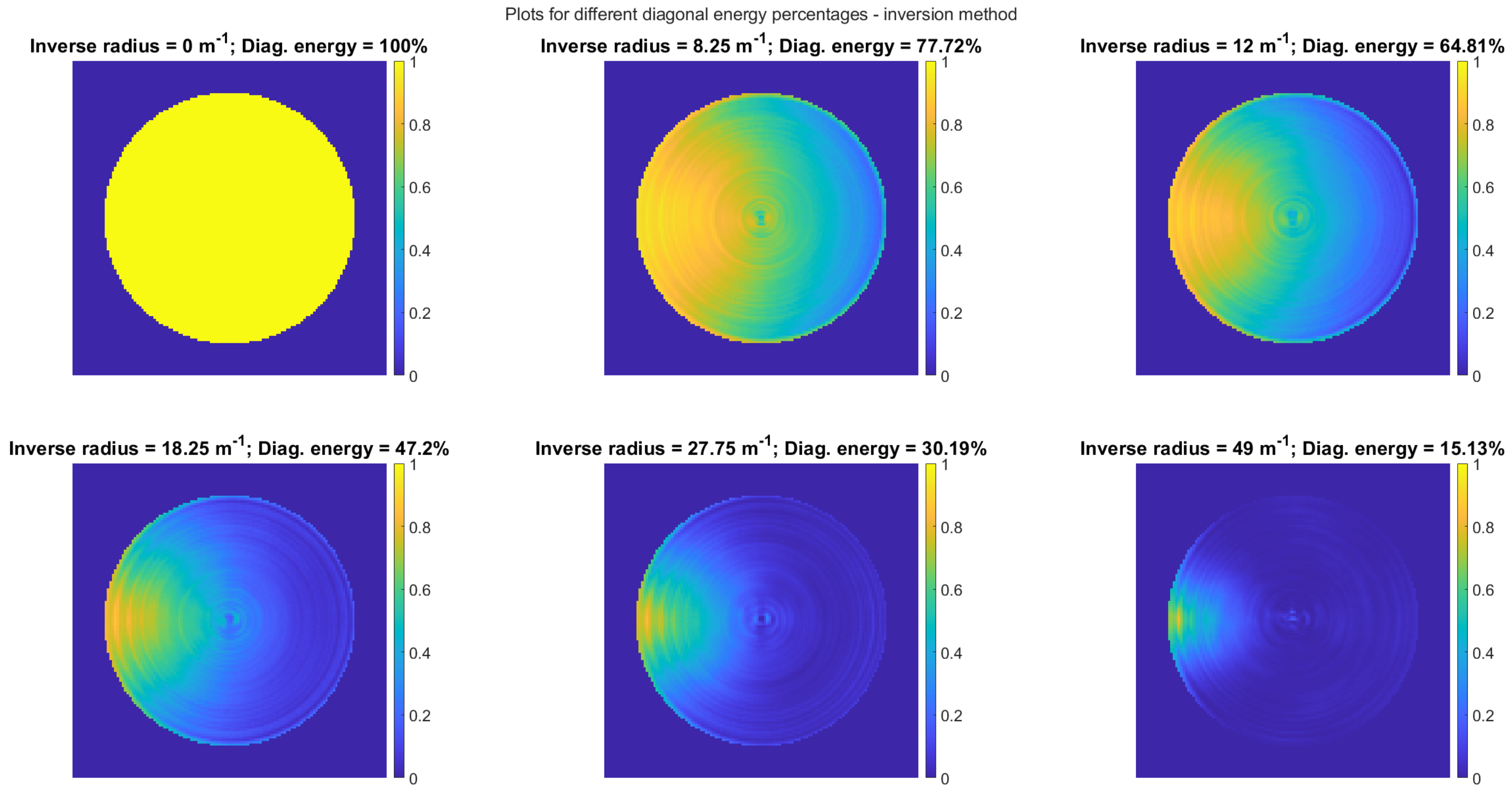

Figure 15: Intensity of the foci generated using memory effect normalised to the intensity of foci generated by inverting the actual bent fibre TM. Results shown for six different inverse bending radii, each with specific diagonal energy associated. The isoplanatic patch is the region where the correction achieves a factor of 0.7.

5 Combining the described techniques into a correction procedure

5.1 Introduction

The target of the correction procedure is to recover the focusing capability in the plane of excitation, during imaging.

The previous chapters have described the procedure to recover the focus at a specific location using sensorless adaptive optics, then expand the area of focusing through the use of the memory effect. This chapter will describe the procedure which combines these techniques to achieve control of the entire optical field at the distal facet by optimising for focusing at multiple reflectors and applying the memory effect on these optimisations then combining the information acquired. Furthermore, the ability to control the optical field over the entire distal facet allows to further expand the focusing capability to a different focus plane than the distal facet.

5.2 Free-space propagation

During imaging, the desired excitation plane can be at a specific axial depth with respect to the distal facet. In the case of a straight fibre, this could be achieved by calibrating the fibre while setting the focal plane of the calibration module at a specific distance away from the distal facet.

The TM measured will describe the relationship between the proximal facet and the excitation plane. However, as the recovered TM using the memory effect approach only describes the transmission up to the reflector plane, a method is needed to relate the optical field in the reflector plane to the optical field in the excitation plane.

Ideally, the reflector plane and the distal facet are identical, but this might

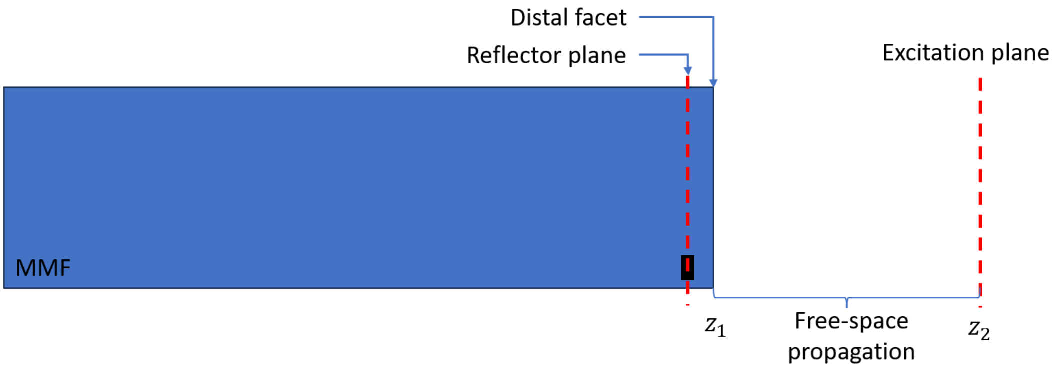

Figure 16: Diagram of the different planes showing the reflector plane, distal facet and excitation plane.

not be the case. However, if the reflector is very close to the distal facet, the fibre between the reflector and distal facet can be assumed straight and the change in the optical field between the two planes can be calculated using the ideal straight fibre case.

However, the change in the optical field between the distal facet and the excitation plane needs to be calculated using a different method. A diagram of the planes is shown in figure 16.

Fourier optics allows for the description of free-space propagation [13]. The change in the optical field between two planes is described by the transfer function in equation 5.1, where A represents the angular spectrum of the optical field, f_x and f_y are the frequency components of the angular spectrum, z is the axial depth of the plane, as shown in the diagram in figure 16, and λ is the wavelength of light.

$$A(f_x, f_y, z_2) = A(f_x, f_y, z_1) \exp\left(i2\pi(z_2 - z_1)\sqrt{\frac{1}{\lambda^2} - f_x^2 - f_y^2} \right) \tag{5.1}$$

The angular spectrum can be calculated using a Fourier Transform: $A(f_x, f_y, z) = \mathcal{F}[u(x, y, z)]$.

It can be seen that in the case of $f_x^2 + f_y^2 > \frac{1}{\lambda^2}$, the square root term becomes imaginary. Thus, some high frequency components of the optical field decay exponentially as an evanescent wave. This phenomenon leads to a diffraction limit to the achievable resolution in an imaging system.

A perfect focus can be modelled by a delta function. The Fourier spectrum of a delta function is a constant function over the entire frequency domain. However, as higher frequency components are evanescent and decay, only the frequency components within a disc centred at (0,0) and radius $\frac{1}{\lambda}$ in the frequency domain propagate. Thus, the achievable focus is in the diffraction limit an airy disc (Fourier transform of a disc), whose radial size up to the first null is $0.61\frac{\lambda}{NA}$, with the numerical aperture of the system also being an additional constraint on the radial size of the disc in the frequency domain.

$$A_{desired}(f_x, f_y, z = z_{exc}) = \text{circ}\left[\mathcal{F}(\delta_{x_{focus}, y_{focus}}), \frac{1}{\lambda^2}\right] \tag{5.2}$$

where

$$\delta_{x_{focus}, y_{focus}} = \begin{cases} 1, & \text{if } x = x_{focus} \text{ and } y = y_{focus} \\ 0, & \text{if } x \neq x_{focus} \text{ or } y \neq y_{focus} \end{cases}$$

$$\iint_{-\infty}^{\infty} \delta_{x_{focus}, y_{focus}} \, dx \, dy = 1$$

$$\text{circ}\left[A(f_x, f_y), \frac{1}{\lambda^2}\right] = \begin{cases} A(f_x, f_y), & \text{if } f_x^2 + f_y^2 \leq \frac{1}{\lambda^2} \\ 0, & \text{if } f_x^2 + f_y^2 > \frac{1}{\lambda^2} \end{cases}$$

The optical field at the distal facet which generates this focus can be found by inverting the free-space propagation transfer function.

$$A_{desired}(f_x, f_y, z_{DF}) = A(f_x, f_y, z_{exc}) \exp\left(-i2\pi(z_{exc} - z_{DF})\sqrt{\frac{1}{\lambda^2} - f_x^2 - f_y^2}\right) \tag{5.3}$$

It can be observed that filtering out the evanescent components prior to inversion is important, as, if they were included, these components would exponentially increase in value.

While the desired field at the distal facet is obtained through inverse Fourier transform, this field would most likely contain components which are not part of the fibre mode space. The actual field achievable at the distal facet is the desired field projected into the modal space, through the use of the mode profile matrix $\mathbf{\Psi}$.

$$\mathbf{y}_{c,desired} = \mathcal{F}^{-1}\left[A_{desired}(f_x, f_y, z = z_{DF})\right]$$

$$\mathbf{y} = \mathbf{\Psi}^{\dagger}\mathbf{y}_{c,desired}$$

$$\mathbf{y}_c = \mathbf{\Psi}\mathbf{\Psi}^{\dagger}\mathbf{y}_{c,desired} \tag{5.4}$$

Finding the field at the proximal facet can then be achieved through inverting the TM of the fibre.

5.3 Free-space propagation results

The first simulations undertaken to showcase the ability to generate foci at a desired excitation plane using free-space propagation were done using a straight fibre. The parameters are identical to the ones described previously in section 4.2. The plane of excitation was chosen at a depth of 100 μm.

As observed in figure 17, where a focus at a radius position of $\frac{0.9 \cdot d}{2}$ was targeted, the free-space propagation approach generates a quadratic phase desired

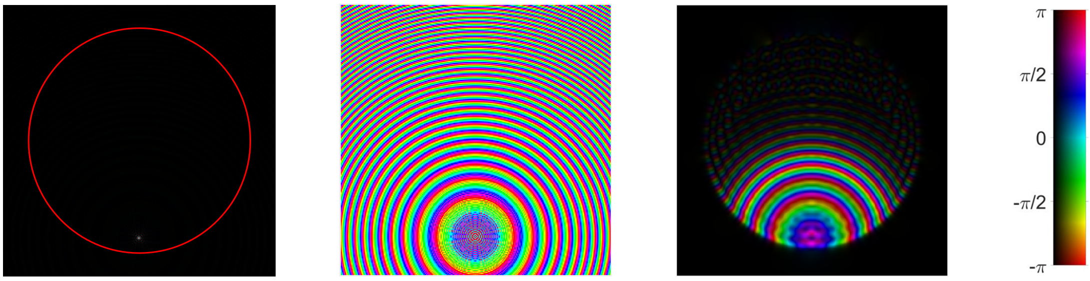

(a) The desired optical field

(b) The phase of the desired optical field

(c) The mode filtered optical field

Figure 17: Optical fields at the distal facet: the desired field determined by back-propagation with the edge of the fibre core outlined in red (a), its phase component (b) and its mode space projection (c). The hue represents phase, as indicated by the colorbar and the value represents the absolute value of the field normalised to its maximum (HSV representation). The maximum absolute value of the filtered field is $\approx 1\%$ of the desired field.

field at the distal facet. This is to be expected, as the back-propagation results in a defocus being applied to the original desired focus.

However, such a field cannot be the output of the fibre, one of the main reasons being that the field extends outside the core facet area. Projecting the desired field into the modal space results in the achievable field at the distal facet. In this case, the maximum absolute value is $\approx 1\%$ of the desired field, the filtered version only containing $\approx 6.3\%$ of the desired total intensity.

The next step is to propagate the obtained filtered field back to the excitation plane. The result is shown in figure 18. While a focus is generated, it does not have a circular shape, due to the effect of the edge of the fibre core edge affecting the amplitude of the input field. The phase inside the fibre core seems not to be affected.

Figure 19a shows a composite image of different foci generated in the excitation plane, at different positions. The foci were generated individually and their vicinity was cropped. Combining the cropped images generated the composite image.

Figure 19b takes a zoomed-in look at the axial shape and extent of the focus

(a) The focus obtained at the excitation plane

(b) Zoomed-in focus at the excitation plane

Figure 18: The resulting focus at the excitation field by propagating the filtered optical field shown in figure 17. The figure shows the intensity of the focus, normalised to the maximum intensity.

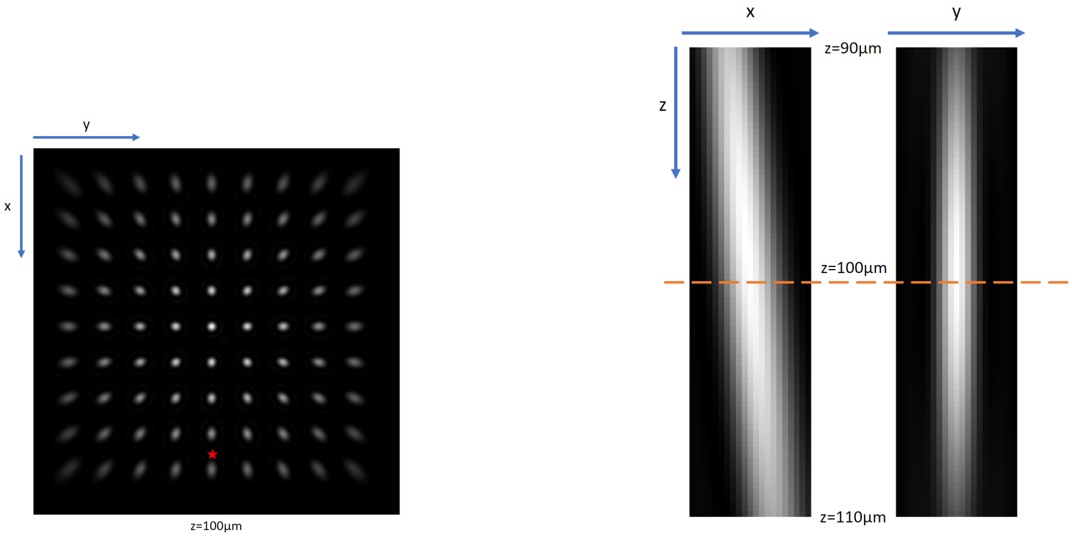

(a) A composite image of foci generated in the excitation plane at different locations. The red star shows the location of the focus generated in figure 18.

(b) The axial shape of the focus at the location of the red star in figure 19a.

Figure 19: A showcase of the foci generated at different positions in the excitation plane. An in-depth look at one of the foci is also included.

generated previously in figures 17 and 18. It is clear that the focus is propagating at an angle away from the centre axis of the fibre facet. This phenomenon of a spatially variant point spread function (PSF) has been observed in practice [31] and it is intrinsic to MMF imaging, as the MMF forms an inherently a non-telecentric system. The accord between the simulation and experimental observations gives confidence in the correctness of the simulation procedure.

5.4 Combining memory effect with free-space propagation

5.4.1 Single correction target

Generating a focus away from the distal facet requires the control of a larger area of the field at the distal facet, as illustrated by figure 17c. Thus, it is expected that the area of the isoplanatic patch decreases with depth of the focus plane.

A set of simulations were done to investigate the effectiveness of the memory effect at different depths and the results for three different depths of 20 μm, 50 μm and 100 μm are shown in figure 20. As described above, the isoplanatic patch decreases in size with increasing depth. The simulations were done for the same set of bending inverse radii and fibre length as in chapter 4, leading to the same values for TM diagonal energy.

5.4.2 Multiple correction targets

The isoplanatic patch generated by a reflector using memory effect does not cover the entire distal facet. As during imaging foci need to be generated over the entire field of view, a single reflector would not suffice. Furthermore, as can be seen in figure 17c, generating a focus further away from the distal facet requires the generation of a desired optical field at the distal facet which is not confined to a single focus.

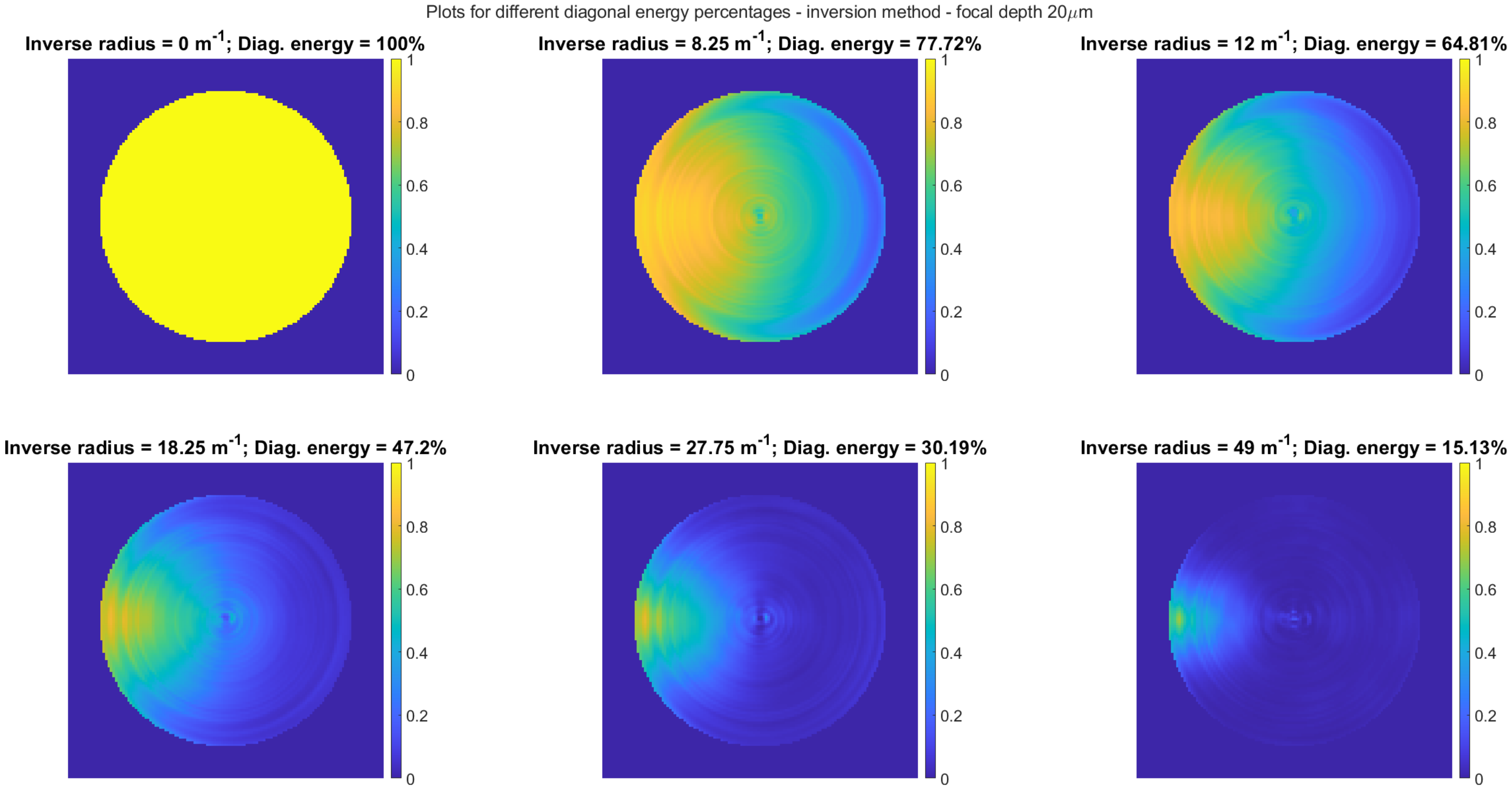

(a) The isoplanatic patch at a focus depth of 20 μm

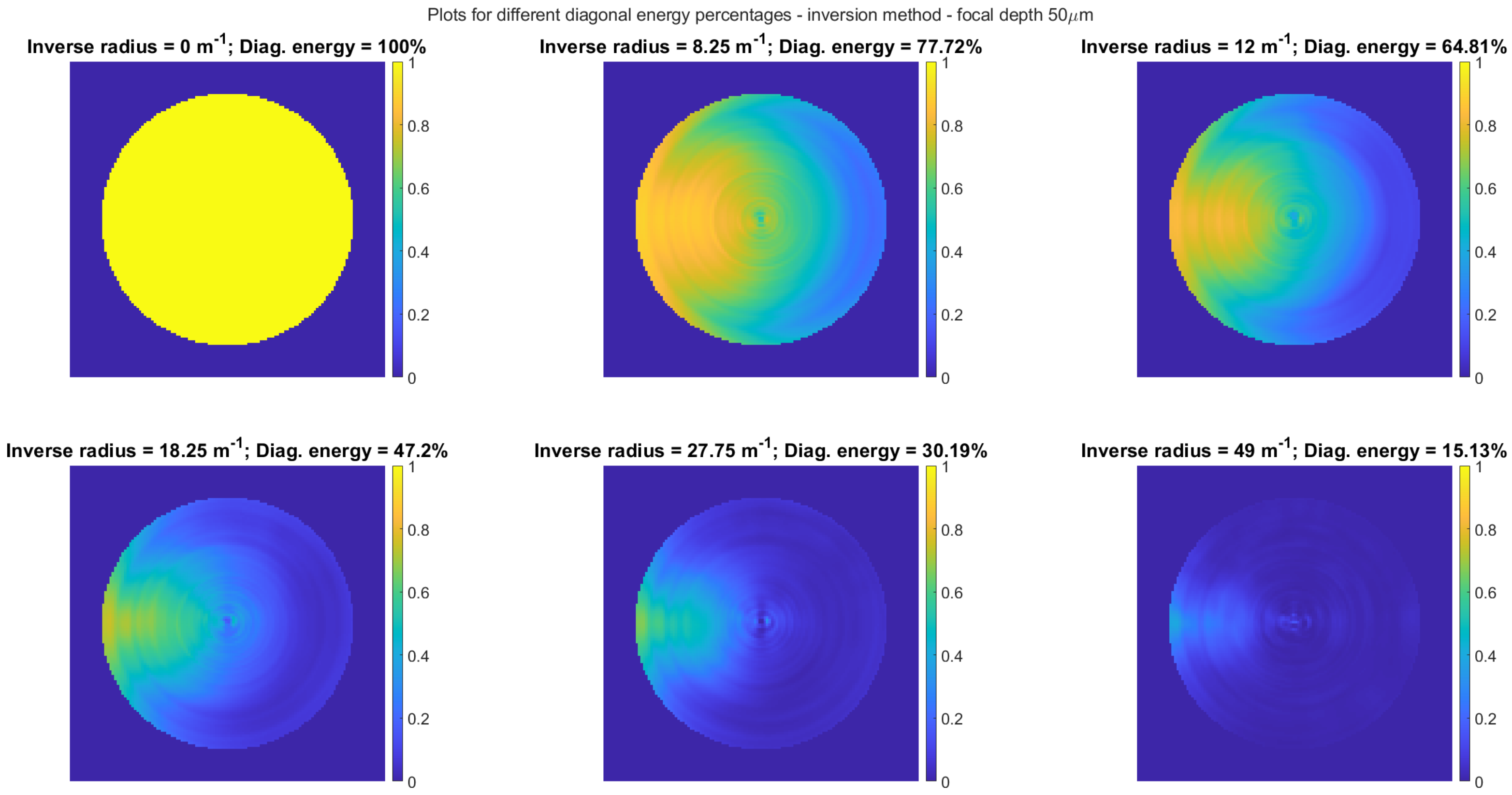

(b) The isoplanatic patch at a focus depth of 50 μm

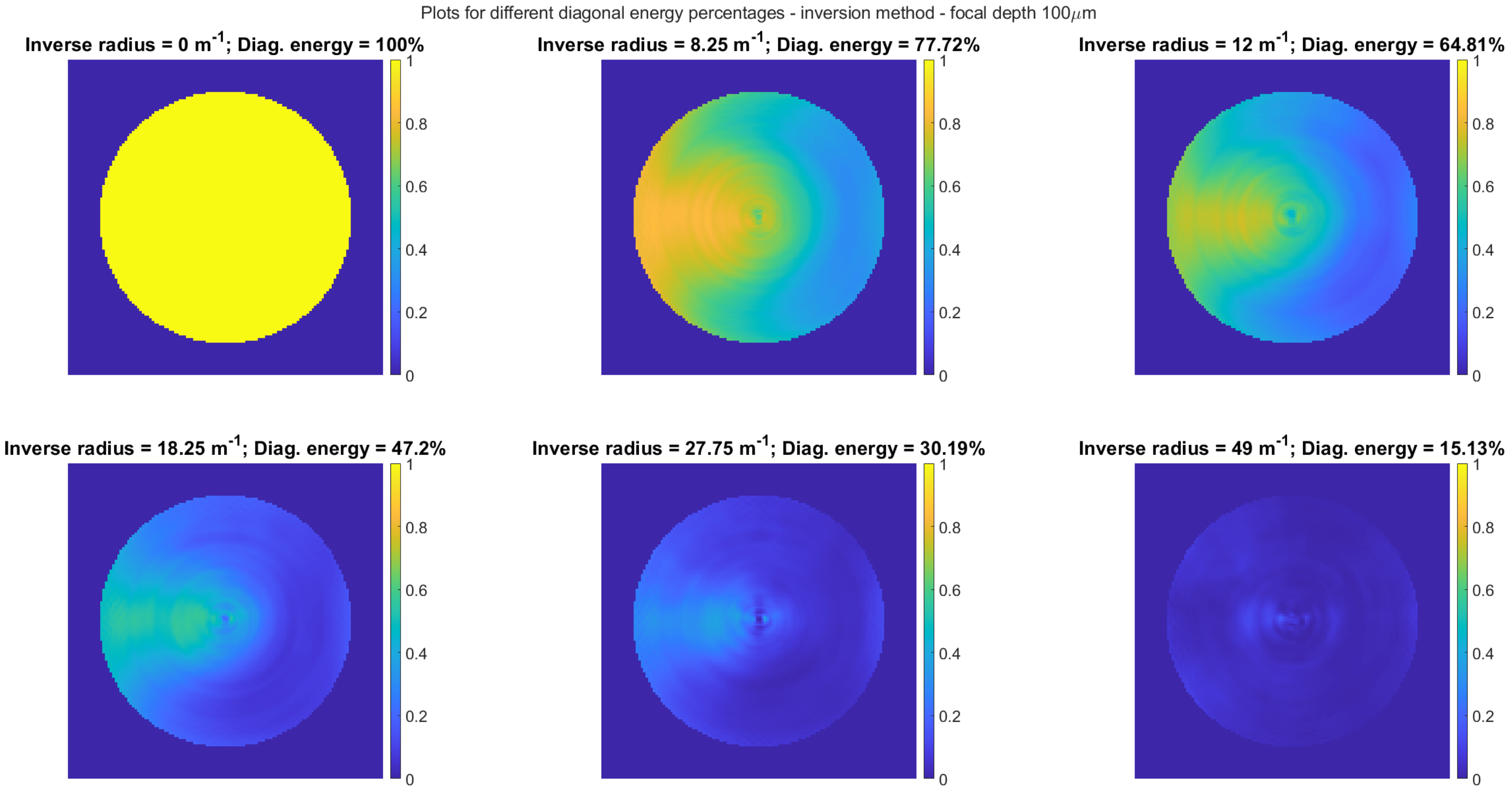

(c) The isoplanatic patch at a focus depth of 100 μm

Figure 20: Intensity of the foci generated using memory effect at different focus plane depths normalised to the intensity of foci generated at the same focus plane by inverting the actual bent fibre TM. Results shown for six different inverse bending radii, each with specific diagonal energy associated. The isoplanatic patch has been defined as the region where the correction achieves a factor of at least 0.7.

Based on the results in figure 15, if a limit to the bending during imaging is assumed, such as $\approx 10\ \mathrm{m}^{-1}$, it would be possible to correct for the entire facet, while only using four reflectors. The value of $10\ \mathrm{m}^{-1}$ of the inverse bending radius for a 1.5 cm of fibre represents a translation of the tip of the fibre by ≈ 1 mm. This would be within the expected deviations which would occur at the brain level during implantation and imaging.

Applying the memory effect to four reflectors results in the generation of four assumed diagonal TMs, each being applicable to to its associated isoplanatic patch. Thus, the desired optical field at the distal facet needs to be split into four regions, each with its own TM. Thus, any desired optical field was considered to be a superposition of the four regions.

In order to calculate the desired input field at the proximal facet, each region component was treated independently and the inverse of its associated diagonal TM was applied. The resulting proximal facet optical fields were then added together, making use of the linearity property of a matrix described transmission to generate the necessary input field to be used.

Simulations were undertaken by choosing four target foci at a radial coordinate of $\frac{0.9 \cdot d}{2}$ and azimuthal coordinates of 0, $\frac{\pi}{2}$, π and $\frac{3\pi}{2}$, where an azimuthal angle of 0 is down as shown on the axis definition in figure 19a. The associated regions were chosen by cutting the optical field diagonally, as shown in figure 21a.

In order to consider an edge case scenario, the focus to be generated has been chosen at a position on the edge of two regions (1 and 2) at a radial coordinate of $\frac{0.9 \cdot d}{2}$ and azimuthal coordinate of $\frac{\pi}{4}$. The calculated desired distal facet field using free-space propagation is illustrated in figure 21b.

Figure 21 shows the splitting of the optical field. Even though the complete optical field is the superposition of the 4 components, it is important to note that these components lose the property of being entirely in the fibre mode space. Thus, even with an entirely known TM, generating the individual components can only be done approximately. This is similar to the previous phenomenon where the quadratic phase field was filtered by the fiber modes, though in this case, the desired field lies entirely within the core area, thus, the approximation will be more similar to the desired field. In figure 22 the projection of the individual components into the fibre mode space is shown. While there is not a large amount of change in the output optical fields, there is some leakage present between the regions. However, this is negligible compared to the desired optical field itself.

The simulation was then performed to compute the isoplanatic patch at different depths with the use of four targets for the memory effect optimisation. As expected, overall, the system performs similarly to having four different copies of the isoplanatic patch resulted in the case with only one target, though there are some differences.

Firstly, it seems that the direction of bending can influence the amount of correction achieved. In this case, the bending was applied vertically with respect to the image. The two targets which lie along the bending direction have performed worse compared with the two targets which are on the direction perpendicular to bending. The reason for this effect is not completely understood. However, as the bending initially distorts the focus along the bending direction, the reason for the difference might have been due to the foci which lie on the bending direction having had their focus distorted radially, while the other two targets having had their focus distorted in an azimuthal direction. As mentioned in section 4.1, optical fibres are more robust to rotational changes that radial.

Secondly, the location which are at the borders of the regions and the centre of the facet perform worse. This could be due to an effect generated by the splitting

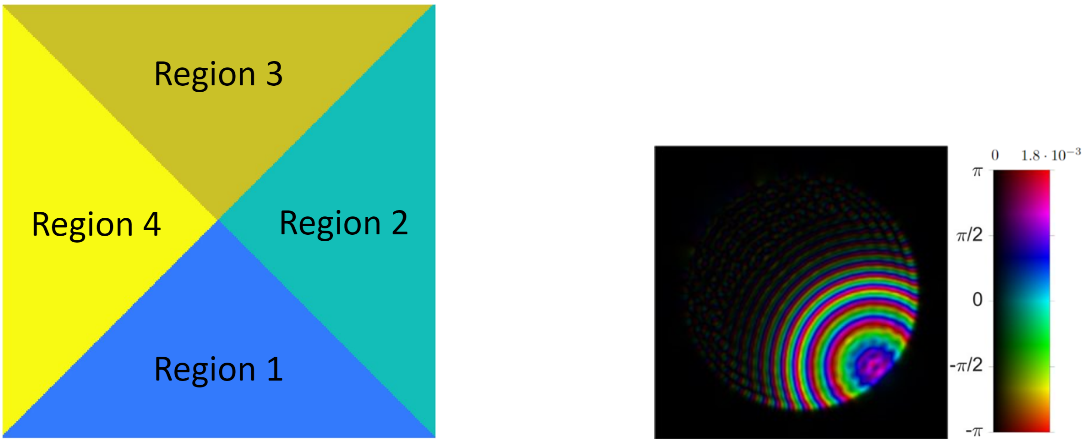

(a) An illustration of the region split of the optical field.

(b) The desired distal facet optical field

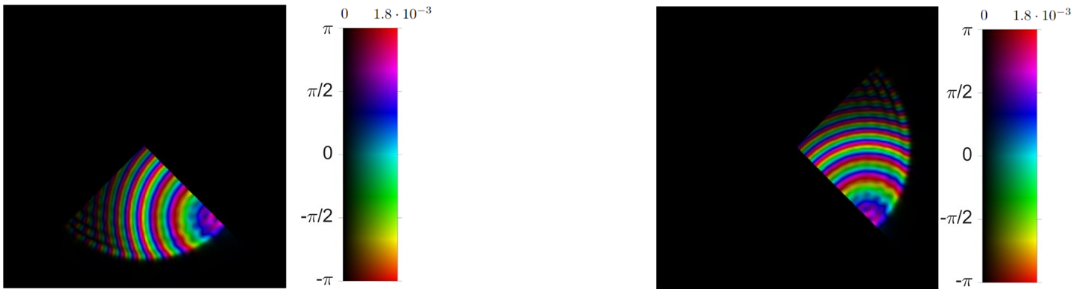

(c) Region 1 component

(d) Region 2 component

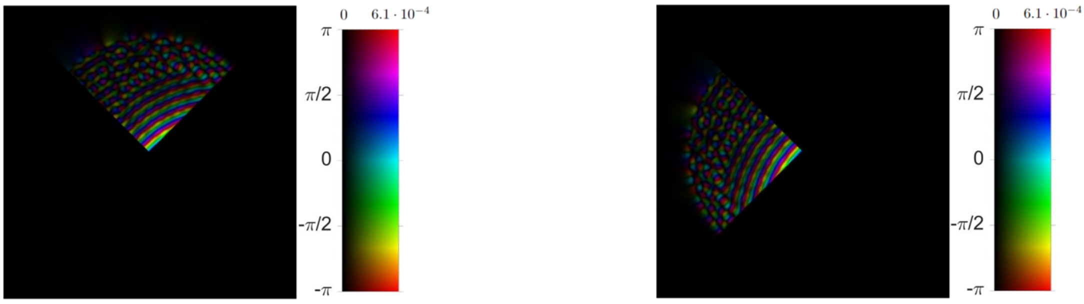

(e) Region 3 component

(f) Region 4 component

Figure 21: The desired optical field at the distal facet for generating a focus at a depth of 100 μm and its division into reflector region components. The location is at a radial coordinate of $\frac{0.9 \cdot d}{2}$ and azimuthal coordinate of $\frac{\pi}{4}$.

(a) Region 1 component, projected into modal space

(b) Region 2 component, projected into modal space

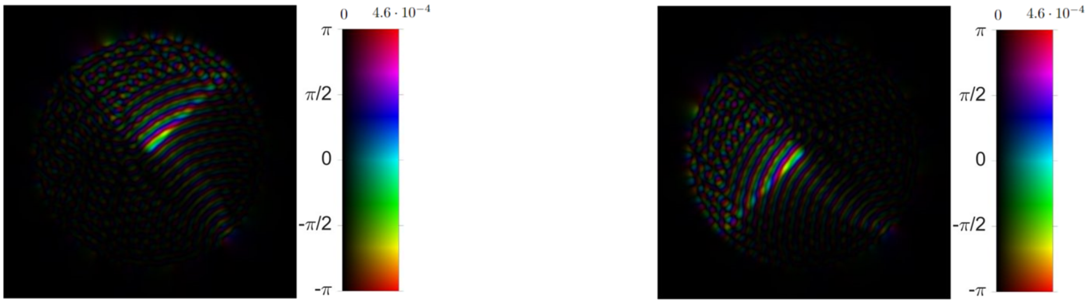

(c) Region 3 component, projected into modal space

(d) Region 4 component, projected into modal space

Figure 22: The optical fields generated by splitting the optical field into reflector regions projecting each region into fibre mode space.

into regions or it could be simply due to the locations being the furthest in the facet from any optimisation target location.

The final result of the simulation was that the approach is usable and could achieve an adequate correction over the entire focus plane.

To further the understanding into the approach, a second set of simulation were done with six targets instead of four, the expectation being that increasing the number of targets will result in a better correction. The targets were uniformly distributed around the facet, while keeping the radial position the same. The regions associated which each target were also generated based on the azimuthal coordinate of each pixel location. The results are shown in figure 24.

As expected, the results are an improvement with respect to using four targets, as each location in the plane has a greater chance of being closer to an

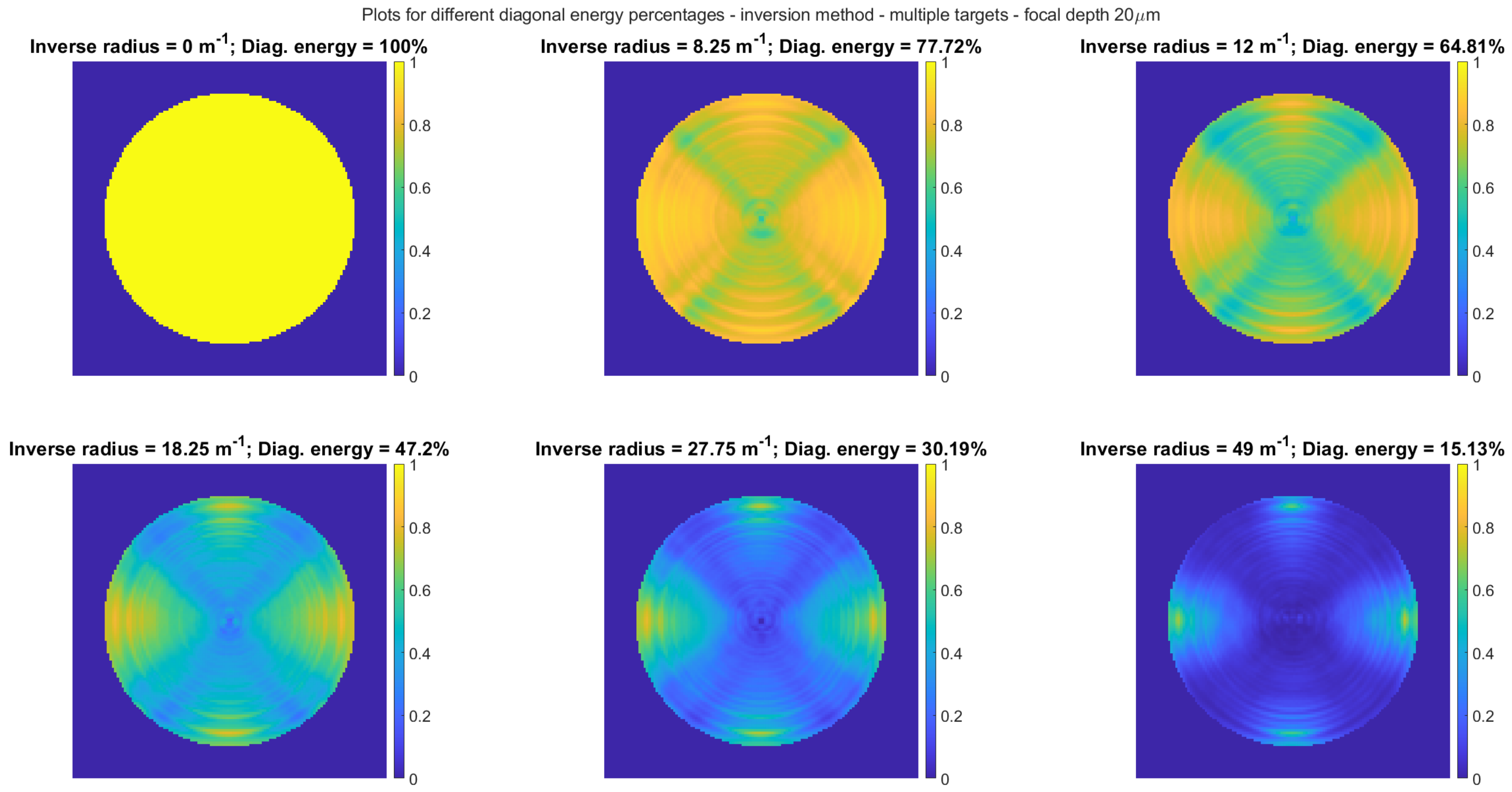

(a) The isoplanatic patch at a focus depth of 20 μm.

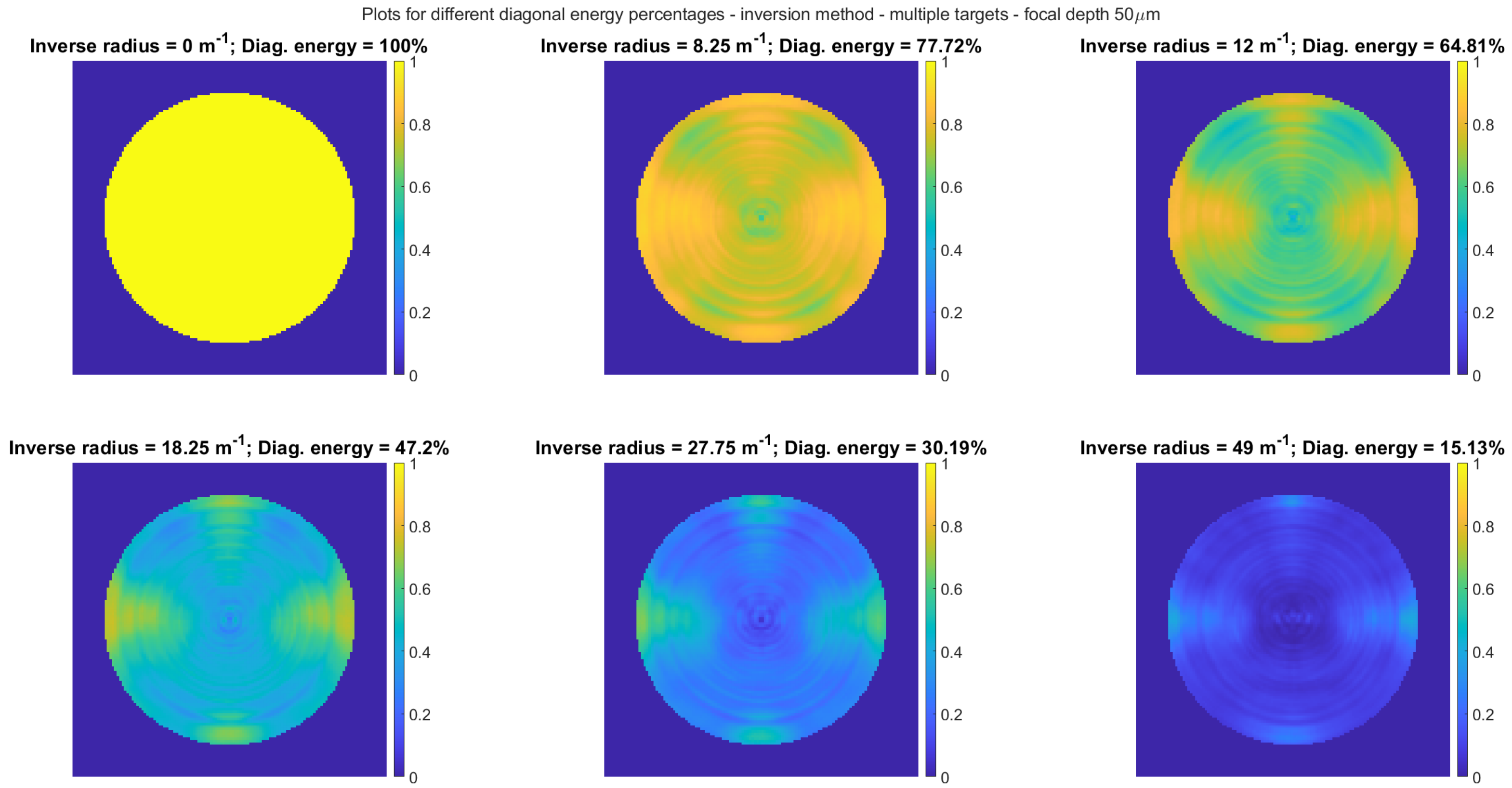

(b) The isoplanatic patch at a focus depth of 50 μm.

Figure 23: Intensity of the foci generated using memory effect at different focus plane depths normalised to the intensity of foci generated at the same focus plane by inverting the actual bent fibre TM. Results shown for six different inverse bending radii, each with specific diagonal energy associated. The isoplanatic patch has been defined as the region where the correction achieves a factor of at least 0.7. Four optimisation targets were chosen spread uniformly over azimuthal range.

optimisation target. This result shows that there is a balancing act which need to be made in the choice of the number of target reflectors, as a larger number leads to better results but also implies more rounds of optimisation being needed to restore focus at each target location.

Finally, in order to showcase the improvement achieved by the correction method, figure 25 shows the resulting isoplanatic patch if no correction is applied. It is clear that even for a smaller amount of bending (inverse radius of 8.25 m^{-1}) the result falls under the 0.7 imposed limit over most of the facet plane.

5.5 Conclusion

In conclusion, the approach described in this chapter has been shown analytically to be feasible in the use for correcting the loss in focusing capabilities of an optical fibre setup generated by bending of said fibre. The approach makes use of the memory effect to infer information about focusing at any location in the excitation plane while only optimising for a small number of locations. Furthermore, it is also able not only to correct but also generate foci at different excitation plane depths without the need to calibrate the fibre numerous times, while changing the calibration arm CCD focus plane.

The number of reflectors used needs to be determined by the amount of bending expected. The more bending is expected, the smaller the isoplanatic patch of the memory effect approach is, thus, leading to a larger number of reflectors being required to cover the entirety of the fibre facet. However, each reflector reduces the amount of light behind it, or even blocks it entirely. Thus, if the focus plane is near the distal facet, there will be blind spots behind the reflectors and in the far-field, some of the spatial frequencies will be blocked, leading to a lower NA. In conclusion, the number of reflectors will need to be chosen in practice taking into consideration this disadvantage.

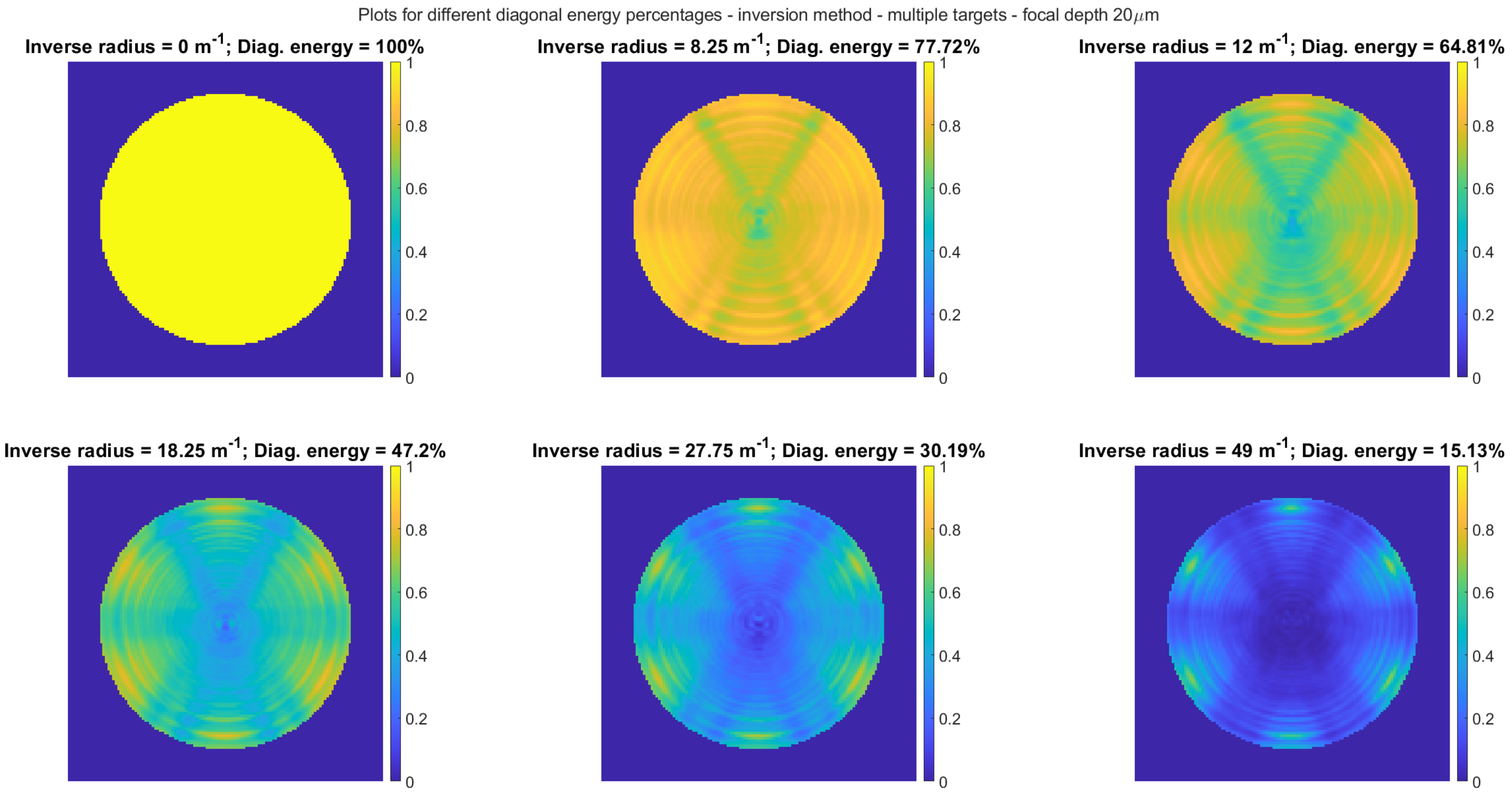

(a) The isoplanatic patch at a focus depth of 20 μm.

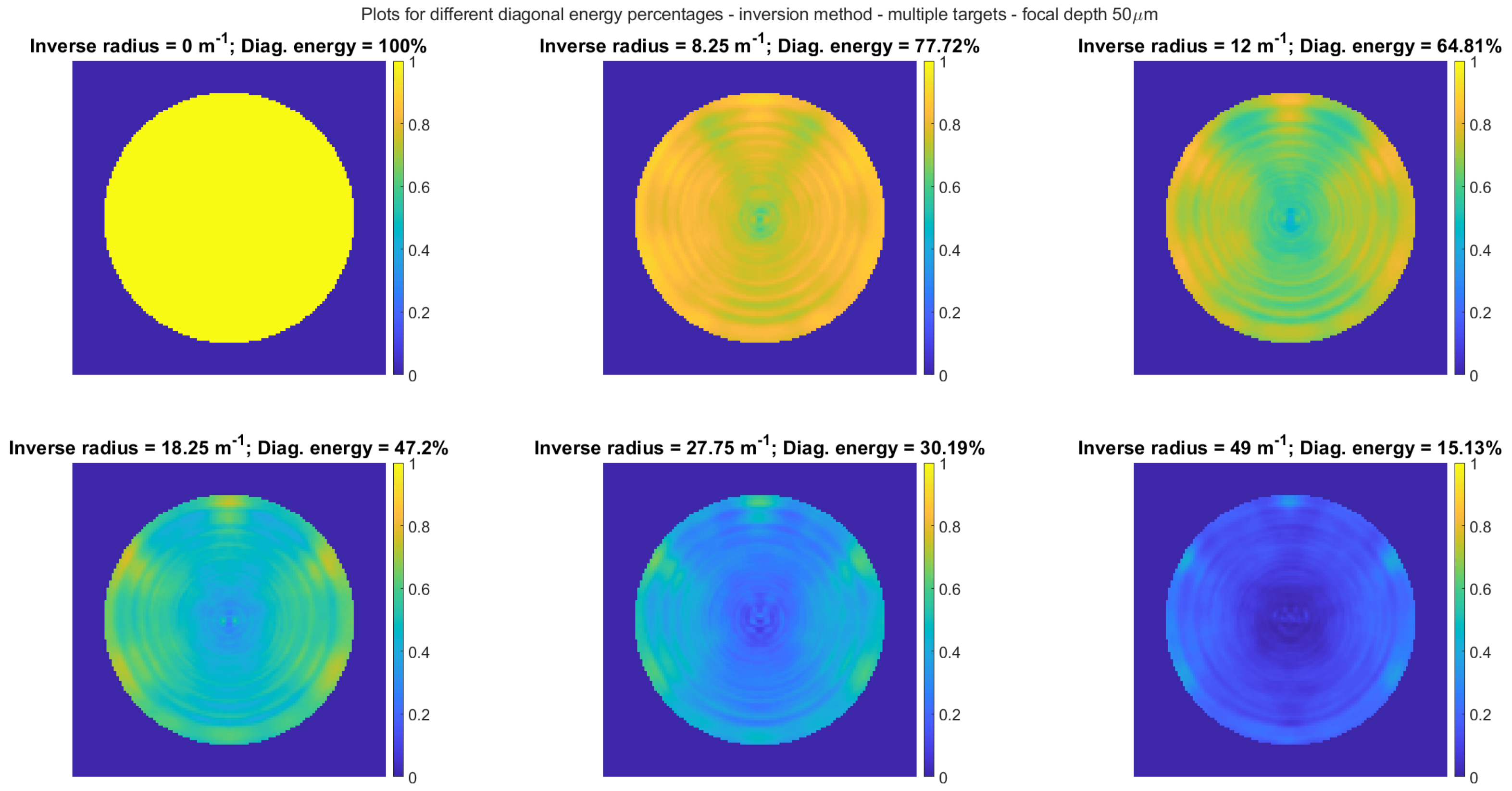

(b) The isoplanatic patch at a focus depth of 50 μm.

Figure 24: Intensity of the foci generated using memory effect at different focus plane depths normalised to the intensity of foci generated at the same focus plane by inverting the actual bent fibre TM. Results shown for six different inverse bending radii, each with specific diagonal energy associated. The isoplanatic patch has been defined as the region where the correction achieves a factor of at least 0.7. Six optimisation targets were chosen spread uniformly over azimuthal range.

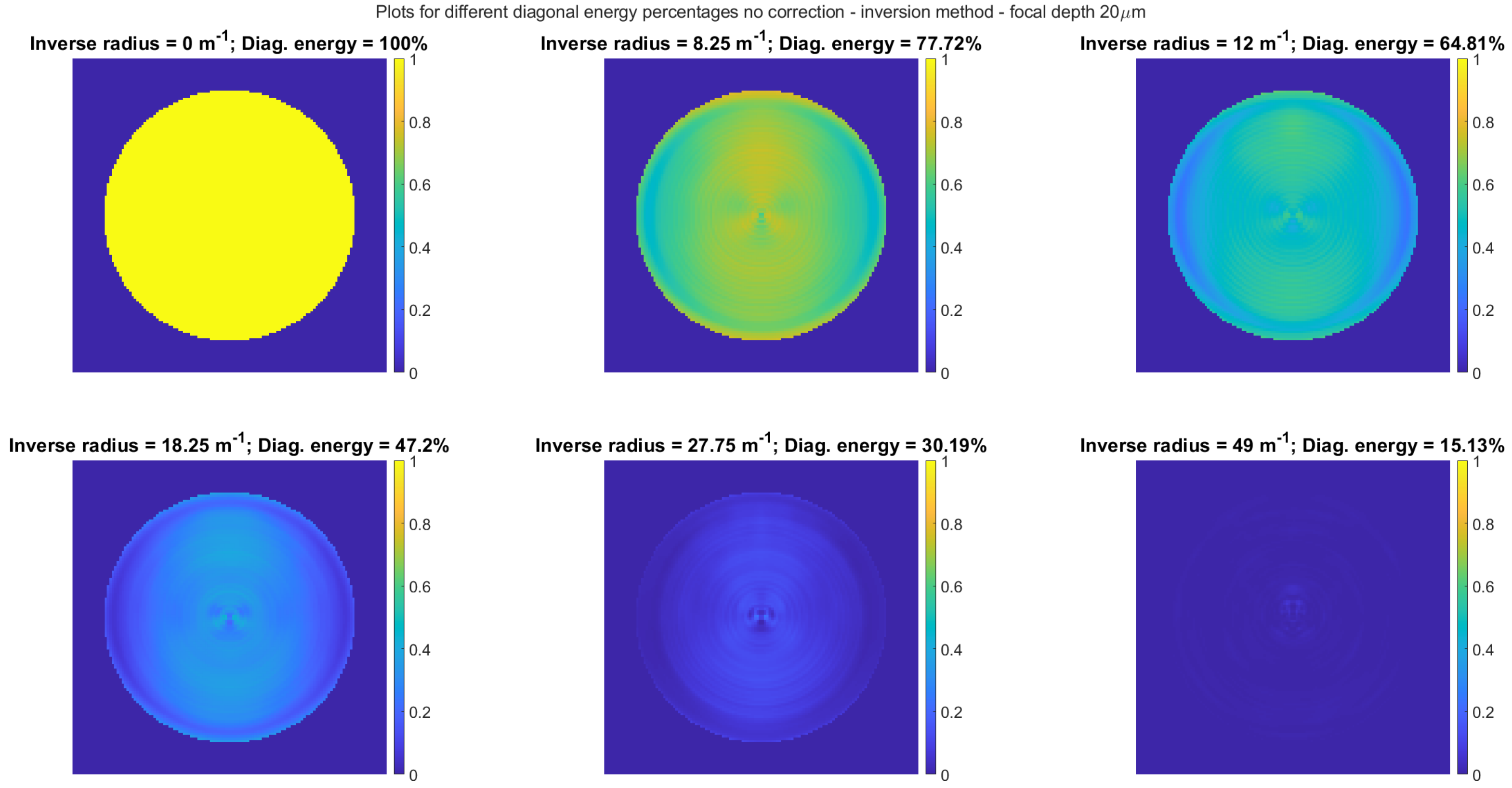

(a) The isoplanatic patch at a focus depth of 20 μm

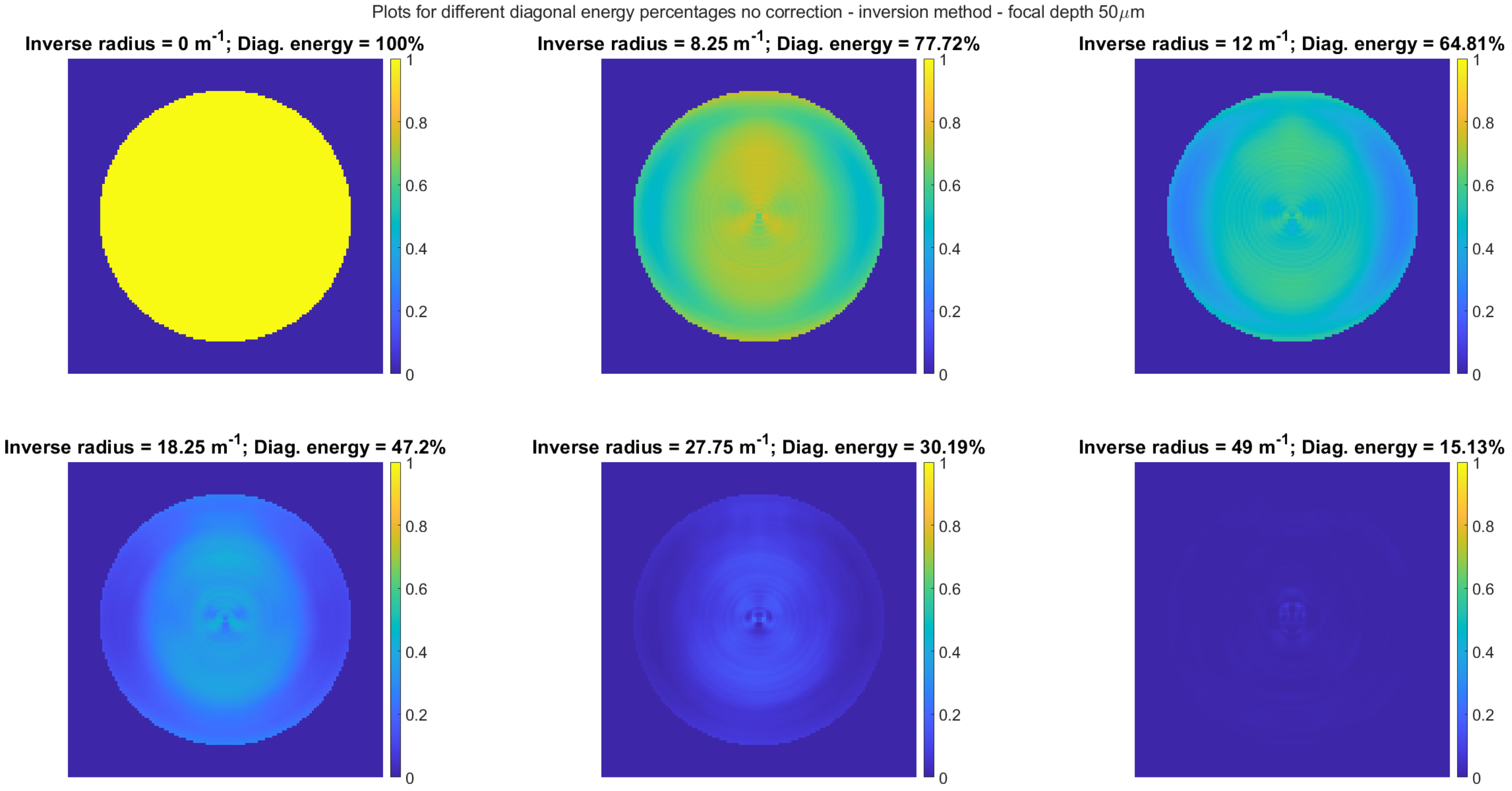

(b) The isoplanatic patch at a focus depth of 50 μm

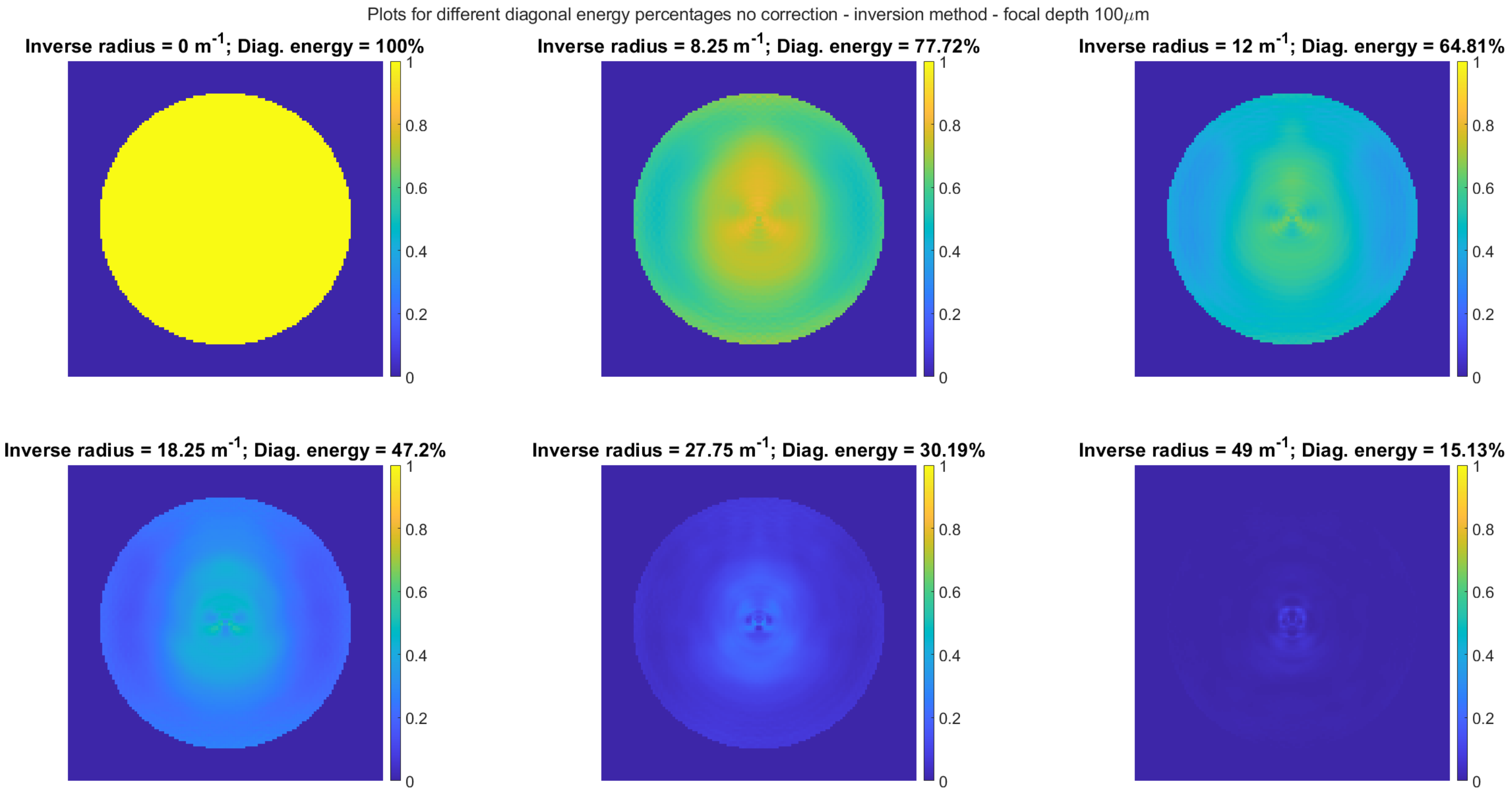

(c) The isoplanatic patch at a focus depth of 100 μm

Figure 25: Intensity of the foci generated without applying any correction at different focus plane depths normalised to the intensity of foci generated at the same focus plane by inverting the actual bent fibre TM. Results shown for six different inverse bending radii, each with specific diagonal energy associated. The isoplanatic patch has been defined the region where the correction achieves a factor of at least 0.7.

6 Bragg gratings as point reflectors in multimode fibres

6.1 Introduction

One of the issues with using multiple reflectors is that the reflected light from each of them needs to be differentiated, in order to achieve a focus at a specific reflector. Using either small mirrors, point scatterers or fluorescent beads could lead to the same amount of reflected or emitted light whether the reflection or emission occurs at a specific location or from multiple locations at the same time. In the case of a reflector that maintains coherence, the phase information is preserved. Thus, phase information can not be used for differentiation as the phase pattern reflected is dependent on bending. As the bending is the scope of the correction, it is unknown and its effect on the change in phase cannot be known.

Bragg gratings can provide the solution to the problem at hand. The reflected light from a Bragg grating can be filtered based on its wavelength, as a function of the grating geometry [32]. This would allow for differentiation by simply using a wavelength based filter to differentiate between light reflected from each grating.

However, two important points will need to be considered. Firstly, the memory effect approach requires focusing at a specific point, which requires that the grating act as a point reflector. Hence, the Bragg grating must be below a characteristic size determined by the physics of the light evolution in the fibre. This could have negative effects experimentally, as the amount of light reflected can also be small. Secondly, being able to achieve a focus at the grating allows for the generation of an assumed TM which is specific to the wavelength of light reflected. Thus, the change in TM due to wavelength needs to be considered before generating the input field for generating an excitation focus, if the focus is to be created using a different wavelength to that for which the Bragg grating was designed.

This chapter focuses on describing a more general approach in simulating a Bragg grating inside a multi-mode fibre. It starts from existing theoretical background and improves the approach to consider coupling between multiple modes, both co-propagating and counter-propagating. The aim is to reduce the problem to a system of de-coupled linear ordinary differential equations, finally, representing the Bragg grating effect on the optical field as a scattering matrix, relating the light exiting the grating section of the fibre to the light entering the grating section of the fibre.

Finally, using this approach, it was investigated whether A Bragg grating can be used as a reflector (localised reflection) and what is the bandwidth of such a grating.

6.2 Existing theoretical background

The theory presented in this subsection follows the coupled-modes approach undertaken in chapter 4 of [32]: ”Theory of Fiber Bragg Gratings” with the aim to describe the coupling between modes generated by the Bragg grating.

The approach starts from the Helmholtz equation for the electric field, where $\mathbf{P}$ is the polarisation field.

$$\nabla^2 \mathbf{E} = \mu_0 \varepsilon_0 \frac{\partial^2 \mathbf{E}}{\partial t^2} + \mu_0 \frac{\partial^2 \mathbf{P}}{\partial t^2} \tag{6.1}$$

The grating can be assumed as an introduced perturbation to the polarisation field, where ‘*up*‘ stands for unperturbed and ‘*p*‘ for perturbed.

$$\mathbf{P} = \mathbf{P}_{up} + \mathbf{P}_p \tag{6.2}$$

The unperturbed polarisation field represents the relative permittivity of the unperturbed material, which is directly related to the refractive index of the material.

$$\mathbf{P}_{up} = \varepsilon_0(\varepsilon_r - 1)\mathbf{E} \tag{6.3}$$

This leads to the modified Helmholtz equation:

$$\nabla^2\mathbf{E} = \mu_0\varepsilon_0\varepsilon_r\frac{\partial^2\mathbf{E}}{\partial t^2} + \mu_0\frac{\partial^2\mathbf{P}_p}{\partial t^2} \tag{6.4}$$

If the perturbation is an isotropic change in refractive index, thus, not introducing any coupling between orthogonal polarisations, then the vector notation can be dropped and the problem can be treated as a scalar field, by looking at only one specific light polarisation.

The total electric field can be represented as a superposition of forward propagating modes (FP), noted with positive index, and backward propagating modes (BP), noted with negative index, where A represents the mode coefficient, ξ_h represents the profile of mode h (mode $-h$ has the same profile, but flipped to overlap transversally with mode h), ω is the angular velocity of the temporal oscillation, β is the absolute value of the propagation constant (identical for modes h and $-h$), N is the number of modes and cc represents the complex conjugate terms (i.e. $\cos(x) = \frac{1}{2}(e^{ix} + cc)$).

$$E = \frac{1}{2}\left[\sum_{h=1}^{N} A_h\xi_h e^{i(\omega t-\beta_h z)} + \sum_{-h=-1}^{-N} A_{-h}\xi_h e^{i(\omega t+\beta_h z)}\right] + cc \tag{6.5}$$

A brief discussion on the modes h and $-h$ is required. As mentioned above, in order for the modes h and $-h$ to couple into each other, they must have the same profile transversally, however, as they propagate in opposite directions, their helicity is opposite. In other words, the modes have the same m index but opposite l index. The same observation can be made about polarisation as well. For the coupling to occur, the transversal polarisation must match, but as the modes propagate in opposite directions, the circular polarisation of the two modes must be orthogonal (one is left-hand while the other is right-hand and vice versa). However, as both the profile helicity and the polarisation is flipped between the modes, the propagation constants of the two modes have the same absolute value, but opposite signs.

Substituting equation 6.5 for E in 6.4, expanding the Laplacian and assuming a slowly varying envelope approximation (equation 6.6) leads to equation 6.7.

$$\frac{\partial^2 A_h}{\partial z^2} \ll \beta_h \frac{\partial A_h}{\partial z} \tag{6.6}$$

$$\sum_{h=1}^{N} -i\beta_h \frac{\partial A_h}{\partial z} \xi_h e^{i(\omega t - \beta_h z)} + \sum_{-h=-1}^{-N} i\beta_h \frac{\partial A_{-h}}{\partial z} \xi_h e^{i(\omega t + \beta_h z)} + cc = \mu_0 \frac{\partial^2 P_p}{\partial t^2} \tag{6.7}$$

The next step is to use the orthogonality relationship of the modes (equation 6.8) by multiplying both sides by ξ_m^* and integrating over the transversal plane (over x and y), which leads to equation 6.9.

$$\iint_{-\infty}^{\infty} \xi_a \xi_b^* dxdy = \frac{2\omega\mu_0}{\beta_a} \delta_{ab} \tag{6.8}$$

$$\frac{\partial A_m}{\partial z} e^{i(\omega t - \beta_h z)} - \frac{\partial A_{-m}}{\partial z} e^{i(\omega t + \beta_h z)} + cc = \frac{i}{2\omega} \iint_{-\infty}^{\infty} \frac{\partial^2 P_p}{\partial t^2} \xi_m^* dxdy \tag{6.9}$$

This new form has allowed for differential terms to be isolated rather than in a sum.

The next step is to look into the form of the perturbed polarisation field.

Writing the perturbed relative permittivity $\varepsilon_{r,total} = \varepsilon_r + \Delta\varepsilon$, using the relationship $P = \varepsilon_0(\varepsilon_{r,total} - 1)E$ and equation 6.2 leads to:

$$P_p = \varepsilon_0 \Delta\varepsilon E \tag{6.10}$$

Using the general relationship $\varepsilon_r = n^2$ and writing the perturbation to the refractive index as $n_{total} = n_0 + \delta n$ leads to:

$$\epsilon_r + \Delta\varepsilon = (n_0 + \delta n)^2 \approx n_0^2 + 2n_0\delta n$$

$$\Delta\varepsilon \approx 2n_0\delta n \tag{6.11}$$

The grating is assumed to be a cosine variation in z such that the change in refractive index is:

$$\delta n = \overline{\Delta n} + \frac{\Delta n}{2}\left[e^{i\frac{2\pi N}{\Lambda}z} + cc\right] \tag{6.12}$$

where:

- $\overline{\Delta n}$ is the mean refractive index change
- Δn is the amplitude of the refractive index change
- Λ is the grating period
- N is the harmonic order
    1. If the grating is sinusoidal, then N can be assumed to be 1.
    2. However, for a non-sinusoidal, but periodic, grating, the refractive index change can be described in terms of a Fourier series expansion, which will have harmonics. Though, a later discussion will show why only one harmonic need be considered.

Combining equations 6.9, 6.10, 6.11 and 6.12 leads to the equation below:

$$\frac{\partial A_m}{\partial z} e^{i(\omega t - \beta_h z)} - \frac{\partial A_{-m}}{\partial z} e^{i(\omega t + \beta_h z)} + cc = \frac{i n_0 \varepsilon_0}{\omega} \iint_{-\infty}^{\infty} \delta n \frac{\partial^2 E}{\partial t^2} \xi_m^* dx dy \tag{6.13}$$

The δn term is composed of a sum between $\overline{\Delta n}$ (the DC term) and a term proportional to Δn (the AC term). Thus, the right-hand side of equation 6.13 can be written as a sum of two integrals, representing the DC and AC terms, respectively.

The book [32] continues the derivation by looking into the coupling between a single FP mode and a single BP mode, deriving the more compact result below. Coupling between modes is heavily dependent on the propagation constants of the modes in question and the grating period. More specifically, in the case of co-propagating modes, the coupling is higher if the propagation constants are closer in value, while in the case of counter-propagating modes, the coupling is higher if the difference in propagation constants is close to a multiple of $\frac{2\pi}{\Lambda}$. A more detailed discussion about detunement is done in sub-section 6.3. Thus, equation 6.13 can be separated into two equations, one for the mode m and another for the mode $-m$ as their propagation constants are very different in value, leading to their coefficient change in z being dependent on different coupling terms. The main assumption made to arrive at the result below is that a specific mode only couples to itself in terms of co-propagation due to DC change in refractive index ($\overline{\Delta n}$) and to only a single counter-propagating mode due to the AC change in refractive index (Δn).

$$\begin{cases} \frac{\partial A_f}{\partial z} &= -i\kappa_{dc,f} A_f - i\kappa_{ac}^* A_{-b} e^{i\Delta\beta z} \\ \frac{\partial A_{-b}}{\partial z} &= i\kappa_{dc,-b} A_{-b} + i\kappa_{ac} A_f e^{-i\Delta\beta z} \end{cases} \tag{6.14}$$

where:

$$\kappa_{dc,-b} = n_0 \omega \varepsilon_0 \iint_{-\infty}^{\infty} \overline{\Delta n} \xi_b \xi_b^* dxdy \tag{6.15}$$

$$\kappa_{dc,f} = n_0 \omega \varepsilon_0 \iint_{-\infty}^{\infty} \overline{\Delta n} \xi_f \xi_f^* dxdy \tag{6.16}$$

$$\kappa_{ac} = n_0 \omega \varepsilon_0 \iint_{-\infty}^{\infty} \frac{\Delta n}{2} \xi_f \xi_b^* dxdy \tag{6.17}$$

$$\Delta\beta = \beta_b + \beta_f - \frac{2\pi N}{\Lambda} \tag{6.18}$$

The terms above describe specific interactions generated by the grating with the two modes. $\kappa_{dc,-b}$ and $\kappa_{dc,f}$ describe how strongly the grating couples the two modes into themselves. κ_{ac} describes how much the modes couple between themselves. The last term, $\Delta\beta$, represents a detunement factor, which also indicates how strongly the modes couple between themselves.

In the case of $f = b$, this set of equations can be solved by eliminating the $e^i \Delta\beta z$ term, then by decoupling the differential equations. $z = 0$ is set to be the beginning of the grating and $z = L$ the end of the grating. The resultant amplitude reflection coefficient becomes:

$$\rho = \frac{A_f(0)}{A_{-f}(0)} = \frac{-\kappa_{ac} \sinh(\alpha L)}{\delta \sinh(\alpha L) - i\alpha \cosh(\alpha L)} \tag{6.19}$$

Where:

$$\delta = \kappa_{dc,f} + \frac{\Delta\beta}{2} \tag{6.20}$$

$$\alpha = \sqrt{|\kappa_{ac}|^2 - \delta^2} \tag{6.21}$$

This results allows for describing the reflection in a simple function which can then be analysed to infer the effect each parameter has on the result. While this is useful for a heuristic description of the coupling between two specific modes, it ignores the coupling between all the other modes.

6.3 Detunement effect on coupling

This subsection will describe the effect on coupling of detunement between two fibre modes. This will provide support for any assumption which can be made going forward about which pairs of modes can be ignored, as their detunement is large enough to assume that the modes do not couple into each other.

The first step in understanding the detunement effect is to understand the effect $\Delta\beta$ has on the coupling. Figure 26 plots $|\rho|$ as a function of $\Delta\beta$ and L. This was done using $\kappa_{dc} = \kappa_{ac} = 1$ as a base value.

It is clear from figure 26, that the reflection coefficient drastically decreases up to that point and limiting the search range for coupling modes up to a $\Delta\beta$ of $1000\frac{\text{rad}}{\text{m}}$ would be a good assumption. It is observed that a longer grating results in larger reflectance, as expected. Additionally, a shorter grating will suffer more from detuning, which is to be expected, as then shorter coupling distances become comparable to the grating length. The plot will be symmetrical about the $\Delta\beta$ axis.

For the fibre parameters $\lambda = 488$ nm, $n_{core} = 1.45$, NA $= 0.22$ of the MMF to be used in practice, calculations lead to $n_{core}k_0 = 1.87 * 10^7\ \frac{\text{rad}}{\text{m}}$ and $n_{cladding}k_0 = 1.845{*}10^7\ \frac{\text{rad}}{\text{m}}$. This result gives a maximum possible $\Delta\beta$ of $216,840\ \frac{\text{rad}}{\text{m}}$ within the set of forward or backward propagating modes. Thus, the range of propagation constants for either FP or BP modes is two orders of magnitude larger that the search range limit placed after observing the result in figure 26. This result shows that an FP mode will only couple into a small subset of BP modes. The significance of this result is that the specificity of the coupling generated by the grating is very high, leading to a good wavelength isolation for the reflection.

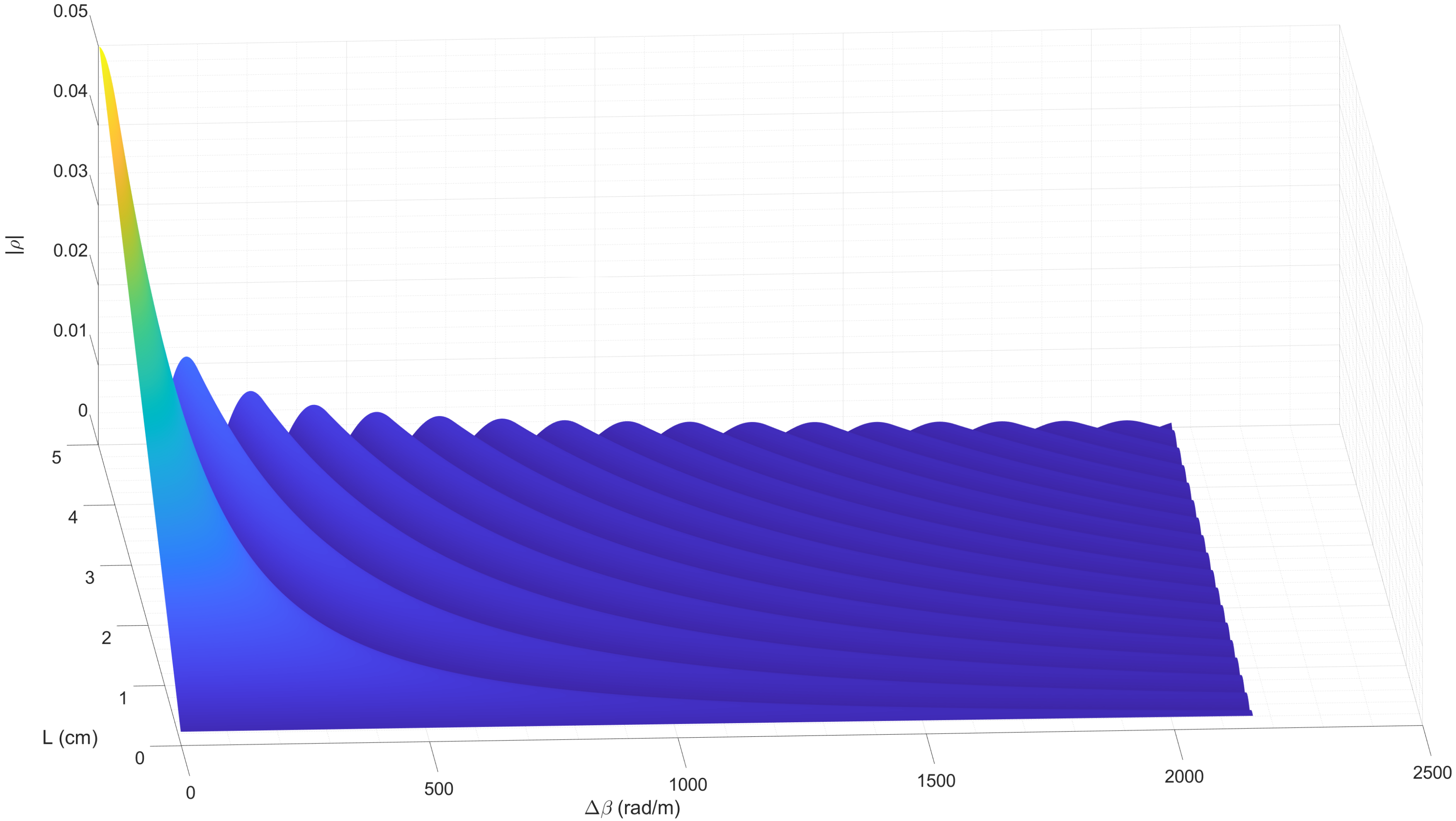

Figure 26: Plot of $|\rho|$ as a function of $\Delta\beta$ and L

6.4 Multi-modal approach

The derivation of the coupling described before only describes the coupling between one forward propagating mode and one backward propagating mode. However, in an MMF, there is a large number of modes propagating in both directions. Thus, in order to analyse how a Bragg grating behaves in an MMF, the interactions between the modes needs to be taken into consideration simultaneously.

The aim of this subsection is to represent the mode coupling as a linear system of ordinary differential equations, where the first order derivative of the mode coefficients with respect to z is equal to a linear summation of the mode coefficients at a specific axial location, which can then be decoupled to allow for solving the system in a straightforward manner.

Following the same approach as in section 6.2, however, this time without any assumptions being made, by expanding both δn and E terms in equation 6.13 and computing the second order partial time derivative of E, the coupled mode equation which arises is given in equation 6.22

$$\begin{aligned}
\frac{\partial A_m}{\partial z}\exp\left[-iz\beta_m\right] - \frac{\partial A_{-m}}{\partial z}\exp\left[iz\beta_m\right] + cc = \\
&- i\sum_{h} A_h \kappa_{dc,(h,m)} \exp\left[iz\left(-\beta_h\right)\right] \\
&- i\sum_{h} A_h \kappa_{ac,(h,m)} \exp\left[iz\left(-\beta_h + \frac{2\pi N}{\Lambda}\right)\right] \\
&- i\sum_{h} A_h \kappa_{ac,(h,m)} \exp\left[iz\left(-\beta_h - \frac{2\pi N}{\Lambda}\right)\right] \\
&- i\sum_{-h} A_{-h} \kappa_{dc,(-h,m)} \exp\left[iz\beta_h\right] \\
&- i\sum_{-h} A_{-h} \kappa_{ac,(-h,m)} \exp\left[iz\left(\beta_h + \frac{2\pi N}{\Lambda}\right)\right] \\
&- i\sum_{-h} A_{-h} \kappa_{ac,(-h,m)} \exp\left[iz\left(\beta_h - \frac{2\pi N}{\Lambda}\right)\right] + cc \qquad (6.22)
\end{aligned}$$

Where:

$$\kappa_{dc,(a,b)} = n_0\omega\varepsilon_0 \iint_{-\infty}^{\infty} \overline{\Delta n}\xi_a\xi_b^* dxdy \tag{6.23}$$

$$\kappa_{ac,(a,b)} = n_0\omega\varepsilon_0 \iint_{-\infty}^{\infty} \frac{\Delta n}{2}\xi_a\xi_b^* dxdy \tag{6.24}$$

As the profile of the FP modes is identical to the profile of the BP modes, then:

$$\begin{aligned}
\kappa_{dc,(a,b)} &= \kappa_{dc,(-a,b)} = \kappa_{dc,(a,-b)} = \kappa_{dc,(-a,-b)} \\
\kappa_{ac,(a,b)} &= \kappa_{ac,(-a,b)} = \kappa_{ac,(a,-b)} = \kappa_{ac,(-a,-b)}
\end{aligned} \tag{6.25}$$

Also, as the only complex parameters in the κ terms are the mode profiles, then it is easy to deduce that:

$$\begin{aligned}
\kappa_{dc,(a,b)} &= \kappa^*_{dc,(b,a)} \\
\kappa_{ac,(a,b)} &= \kappa^*_{ac,(b,a)}
\end{aligned} \tag{6.26}$$

6.4.1 Discussion on the terms of the full-form equation

The amount each term in the full-form equations contribute to coupling one of the modes present on the left side of equation 6.22 is dependent on how close the $\exp(iz)$ terms are. As on the left side of equation 6.22 the exponential terms contain a $-\beta_m$ and a $+\beta_m$ term, there is a very large difference in the propagation constants. Thus, if a specific term on the right hand side is tuned to one term in the left hand side, it will be detuned to the other and not contribute to it, leading to the possibility of treating the coupling into the forward m mode separately from the coupling into the $-m$ mode.

First, an overview of the propagation constants is important. In a multi-mode fibre, the propagation constants of the FP modes are in the range of $-n_{core}k_0$

to $-n_{clad}k_0$ and in the range of $n_{clad}k_0$ to $n_{core}k_0$ for the BP modes. Figure 27 illustrates these intervals, while also providing values for a fibre with $n_{core} = 1.45$ and $NA = 0.22$ transmitting light of wavelength: $\lambda = 488$ nm. The illustration will provide the basis for visualising detunement.

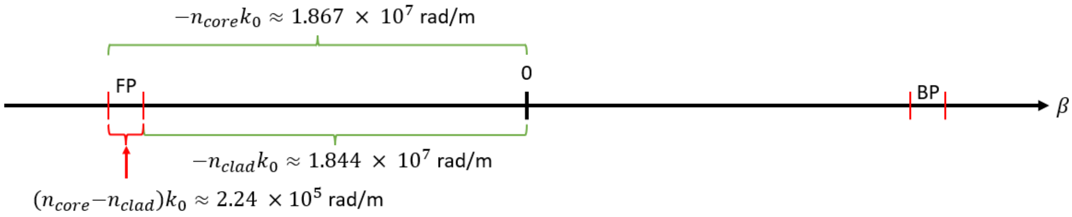

Figure 27: Illustration of the difference between the propagation constants of forward and backward propagating modes

As it can be seen, the range of propagation constants available for propagating modes is much smaller than the absolute value of the propagation constant itself ($\approx 1\%$). Furthermore, based on the figure in section 6.6, appreciable coupling occurs for a detunement range of $\approx (-1000, 1000)\frac{\text{rad}}{\text{m}}$, which is another 2 orders of magnitude lower. Thus, coupling is extremely specific in terms of phase matching compared to the range of propagation constants within a set of fibre modes.

Before discussing which right-hand side terms in equation 6.22 contribute to which left-hand side term or not at all, a discussion is required on what each right-hand side term represents physically.

The terms which contain κ_{dc} components (and implicitly $\overline{\Delta n}$) represent DC coupling generated by the DC component of the grating. Similarly, terms which contain κ_{ac} components (and implicitly Δn) represent AC coupling generated by the AC component of the grating.

In terms of propagation direction, the terms which contain a phase term of $-\beta_h$ represent coupling generated by FP modes, while terms which contain a phase term of $+\beta_h$ represent coupling generated by BP modes.

Lastly, AC terms are also split based on the sign of the harmonic order of the grating in question. Thus, terms with a phase evolution term of $+\frac{2\pi N}{\Lambda}$ represent a positive grating harmonic, while terms with a phase evolution term of $-\frac{2\pi N}{\Lambda}$ represent a negative grating harmonic.

Table 1 provides a concise description of all of the right-hand side terms. The first column shows an index being assigned to each term. This will become useful in the discussion below. The last two columns indicate which terms contribute to coupling into which mode, which is discussed below.

For a term on the right-hand side of equation 6.22 to represent coupling into the forward propagating mode m, it needs to phase match with $\exp\left[-iz\beta_m\right]$. Similarly, for a right-hand side term to represent coupling into the backward propagating mode $-m$, it needs to phase match $\exp\left[iz\beta_m\right]$.

	Right-hand side term	DC/AC	FP/BP	N sign	A_m term	A_{-m} term
1	$-i\sum_h A_h\kappa_{dc,(h,m)} \exp\left[iz\left(-\beta_h\right)\right]$	DC	FP	N/A	Yes	No
2	$-i\sum_h A_h\kappa_{ac,(h,m)} \exp\left[iz\left(-\beta_h + \frac{2\pi N}{\Lambda}\right)\right]$	AC	FP	+	No	Yes
3	$-i\sum_h A_h\kappa_{ac,(h,m)} \exp\left[iz\left(-\beta_h - \frac{2\pi N}{\Lambda}\right)\right]$	AC	FP	-	No	No
4	$-i\sum_{-h} A_{-h}\kappa_{dc,(-h,m)} \exp\left[iz\beta_h\right]$	DC	BP	N/A	No	Yes
5	$-i\sum_{-h} A_{-h}\kappa_{ac,(-h,m)} \exp\left[iz\left(\beta_h + \frac{2\pi N}{\Lambda}\right)\right]$	AC	BP	+	No	No
6	$-i\sum_{-h} A_{-h}\kappa_{ac,(-h,m)} \exp\left[iz\left(\beta_h - \frac{2\pi N}{\Lambda}\right)\right]$	AC	BP	-	Yes	No

Table 1: Table describing the effect of each line of the right hand side of the equation 6.22. The first column assigns an index to each term. The second column shows the right-hand side term in question. The “DC/AC” column describes if the term is generated by DC or AC coupling. The “FP/BP” column indicates if the term represents coupling generated by FP or BP modes. The “N sign” column describes if the term represents a coupling generated by a positive or negative sign harmonic order. This does not apply for DC terms (it could also be considered a harmonic order of 0). The “A_m term” and “A_{-m} term” columns indicate if the term represents coupling into the A_m and A_{-m} modes, respectively.

Due to the large difference in propagation constants (see fig. 27), DC coupling cannot occur between counter-propagating modes (i.e. a FP mode cannot DC couple into a BP mode and vice-versa). Thus, term 1 only contributes to coupling into the A_m mode (if $-\beta_h \approx -\beta_m$), while term 4 only contributes to coupling into the A_{-m} mode (if $\beta_h \approx \beta_m$).

For co-propagation AC coupling to occur (terms 2 and 3 to contribute to coupling into A_m mode and terms 5 and 6 to contribute to coupling into A_{-m}

mode), the requirement is: $\beta_h \approx \beta_m \pm \frac{2\pi N}{\Lambda}$ for terms 5 and 6 and $-\beta_h \approx -\beta_m \pm \frac{2\pi N}{\Lambda}$ for terms 2 and 3.

The diagram in figure 28 provides a visual representation of the requirement for co-propagation AC coupling.

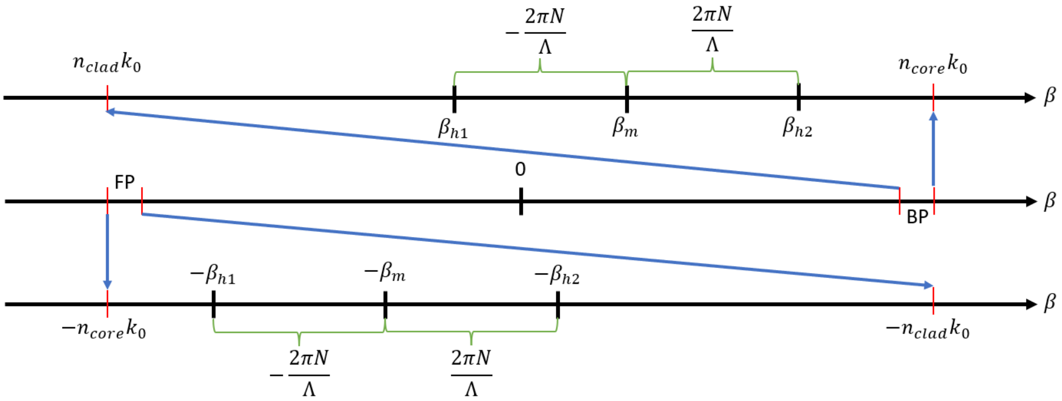

Figure 28: Diagram of co-propagation AC coupling requirement. Middle line shows the entire range of propagation factors for both FP and BP fibre modes. The top and bottom line is a zoomed-in view on the propagation constants range of the BP and FP modes, respectively. The top line illustration shows the requirement for the AC component of the grating to couple a BP mode with propagation constant β_m into other BP modes with propagation constants β_{h1} and β_{h2} which are co-propagating. The bottom line shows the same requirement for FP modes.

It is clear that for co-propagation AC coupling to occur, $\frac{2\pi N}{\Lambda}$ must be small, thus, the grating period must be long. For the fiber parameters given at the beginning of the subsection, in order for such coupling to even be possible the grating period would need to be: $\Lambda \geq \frac{2\pi}{(n_{core}-n_{clad})k_0} \approx 28\mu\text{m}$.

For counter-propagation AC coupling to occur (terms 2 and 3 to contribute to coupling into A_{-m} mode and terms 5 and 6 to contribute to coupling into A_m mode), the requirement is: $-\beta_h \approx \beta_m \pm \frac{2\pi N}{\Lambda}$ for terms 2 and 3 and $\beta_h \approx -\beta_m \pm \frac{2\pi N}{\Lambda}$ for terms 5 and 6.

The diagram in figure 29 provides a visual representation of the requirement for AC counter-propagation coupling for gratings with a small period.

The first observation is that FP mode into BP mode AC coupling is only provided by positive sign harmonics, thus, only term 2 couples into the A_{-m} mode and term 3 does not. Similarly, BP mode into FP mode AC coupling is only provided by negative sign harmonics, thus, only term 6 couples into the A_m mode and term 5 does not.

In order for this type of coupling to occur, either the grating period needs to be small, or the harmonic order large. In the case of a small grating period, where a low-order harmonic provides counter-propagation coupling, co-propagation AC coupling can be assumed to be impossible (terms 2 and 3 do not contribute to the A_m mode, while terms 5 and 6 do not contribute to A_{-m} mode). Furthermore, only one harmonic provides such coupling, as other orders would fall outside fibre mode propagation range.

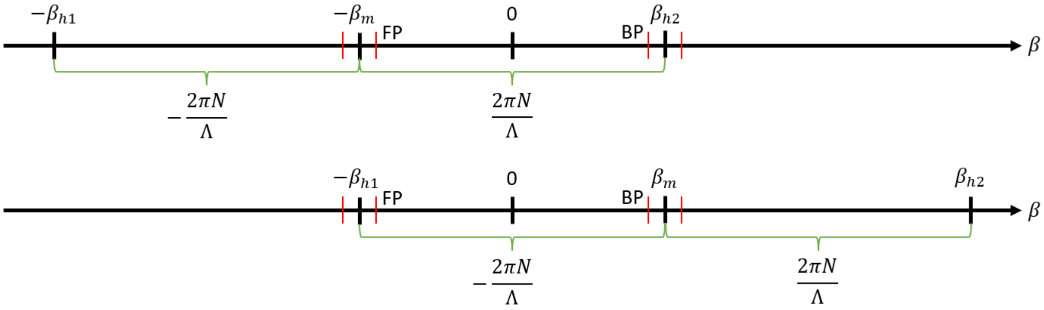

Figure 29: Diagram of counter-propagation AC coupling requirement. The top line shows the requirement for the AC component of the grating to couple a FP mode with propagation factor $-\beta_m$ into a BP mode with propagation factor β_{h2}. Technically, a mode with propagation constant $-\beta_{h1}$ could also be coupled into, however, there are no propagation fibre modes with such a propagation factor as they would be outside the propagation range of the fibre. The same is shown with the second line for the case of a BP mode.

For both co-propagation and counter-propagation AC coupling to occur, a large grating period is required, however, the grating also needs to have very-high order harmonic components.

For the fibre parameters given at the beginning of the subsection and given the limitation of $\Lambda \geq 28\mu$m required for co-propagation Ac coupling, then counter-propagation coupling would occur at harmonics orders of: $N > 82$. In such a case, it is also important to note, that multiple harmonics could provide counter-propagation coupling (i.e. if the harmonic of order N provides counter-propagation coupling, then the harmonics of orders $\{...\ N-2,\ N-1,\ N+1,\ N+2\ ...\}$ could also provide coupling, as the step difference between them of $\frac{2\pi}{\Lambda}$ is smaller than the range of propagation constants of the fibre modes of one type of propagation: BP or FP).

My work focuses on small grating periods, where co-propagation AC coupling does not occur and only a single harmonic provides counter-propagation AC coupling, each term contribution to coupling into either the FP or BP modes being indicated in the last two columns of table 1.

Thus, the simplified and separated form of the equation 6.22 is:

$$\begin{aligned}\frac{\partial A_m}{\partial z} + cc = & \\ & - i \sum_h A_h \kappa_{dc,(h,m)} \exp\left[iz\left(\beta_m - \beta_h\right)\right] \\ & - i \sum_{-h} A_{-h} \kappa_{ac,(-h,m)} \exp\left[iz\left(\beta_m + \beta_h - \frac{2\pi N}{\Lambda}\right)\right] + cc \end{aligned} \tag{6.27}$$

$$\begin{aligned}\frac{\partial A_{-m}}{\partial z} + cc = & \\ & + i \sum_h A_h \kappa_{ac,(h,-m)} \exp\left[iz\left(-\beta_m - \beta_h + \frac{2\pi N}{\Lambda}\right)\right] \\ & + i \sum_{-h} A_{-h} \kappa_{dc,(-h,-m)} \exp\left[iz\left(-\beta_m + \beta_h\right)\right)] + cc \end{aligned} \tag{6.28}$$

6.5 Generating a linear state matrix

The purpose of this section is to reduce the forms of equations 6.27 and 6.28 to a state matrix form $\mathbf{x}' = \mathbf{M}\mathbf{x}$. If matrix $\mathbf{M}$ is not dependent on z, then an eigenvalue approach would allow for decoupling the equations and writing them into a simple set of first-order ordinary differential equations.

The first target is to eliminate the e^{iz} dependence in the state matrix. The trick is to have the exponential terms within the new coefficients in the column vectors, rather than in the matrix:

$$B_m = A_m e^{i(-\beta_m + \frac{\pi N}{\Lambda})z} \Leftrightarrow A_m = B_m e^{i(\beta_m - \frac{\pi N}{\Lambda})z} \tag{6.29}$$

$$B_{-m} = A_{-m} e^{i(\beta_m - \frac{\pi N}{\Lambda})z} \Leftrightarrow A_{-m} = B_{-m} e^{i(-\beta_m + \frac{\pi N}{\Lambda})z} \tag{6.30}$$

First, let's introduce B, which is a function of z as was A, to equation 6.27. The terms on the left hand side will become:

$$\begin{aligned}\frac{\partial A_m}{\partial z} &= \frac{\partial}{\partial z}\left(B_m \exp\left[i(\beta_m - \frac{\pi N}{\Lambda})z\right]\right)\\ &= \frac{\partial B_m}{\partial z}\exp\left[i(\beta_m - \frac{\pi N}{\Lambda})z\right] + i\left(\beta_m - \frac{\pi N}{\Lambda}\right) B_m \exp\left[i(\beta_m - \frac{\pi N}{\Lambda})z\right]\end{aligned} \tag{6.31}$$

The first term on the right hand side of equation 6.27 will become:

$$\begin{aligned}&-i\sum_h A_h \kappa_{dc,(h,m)} \exp\left[iz\left(\beta_m - \beta_h\right)\right] =\\ =&-i\sum_h B_h \kappa_{dc,(h,m)} \exp\left[iz\left(\beta_h - \frac{\pi N}{\Lambda}\right)\right] \exp\left[iz\left(\beta_m - \beta_h\right)\right]\\ =&-i\sum_h B_h \kappa_{dc,(h,m)} \exp\left[iz\left(\beta_m - \frac{\pi N}{\Lambda}\right)\right]\end{aligned} \tag{6.32}$$

Lastly, the second term on the right hand side of equation 6.27 will become:

$$\begin{aligned}
&\sum_{-h} -i\kappa^*_{ac,(m,-h)} \exp\left[i\left(\beta_m + \beta_h - \frac{2\pi N}{\Lambda}\right)z\right] A_{-h} = \\
&= \sum_{-h} -i\kappa^*_{ac,(m,-h)} \exp\left[i\left(\beta_m + \beta_h - \frac{2\pi N}{\Lambda}\right)z\right] B_{-h} \exp\left[i\left(-\beta_h + \frac{\pi N}{\Lambda}\right)z\right] \\
&= \sum_{-h} -i\kappa^*_{ac,(m,-h)} \exp\left[i\left(\beta_m - \frac{\pi N}{\Lambda}\right)z\right] B_{-m} \qquad (6.33)
\end{aligned}$$

Combining the new form of the terms in equation 6.27, the e^{iz} factor can be eliminated:

$$\frac{\partial B_m}{\partial z} = -i\left(\beta_m - \frac{\pi N}{\Lambda}\right) B_m + \sum_h -i\kappa_{dc,(h,m)} B_h + \sum_{-h} -i\kappa^*_{ac,(m,-h)} B_{-h} \qquad (6.34)$$

Applying the same approach for $\frac{\partial A_{-m}}{\partial z}$ leads to:

$$\frac{\partial B_{-m}}{\partial z} = i\left(\beta_m - \frac{\pi N}{\Lambda}\right) B_{-m} + \sum_{-h} i\kappa_{dc,(-h,-m)} B_{-h} + \sum_h i\kappa_{ac,(h,-m)} B_h \qquad (6.35)$$

Thus, the equations above can be written as a linear state matrix. An example for two FP and two BG modes is given below:

$$\frac{\partial}{\partial z}\begin{pmatrix} B_1 \\ B_2 \\ B_{-1} \\ B_{-2} \end{pmatrix} = \boldsymbol{M_B} \begin{pmatrix} B_1 \\ B_2 \\ B_{-1} \\ B_{-2} \end{pmatrix} \qquad (6.36)$$

where:

$$\boldsymbol{M_B} =$$

$$\begin{pmatrix} -i\left(\kappa_{dc,(1,1)} + \beta_1 - \frac{\pi N}{\Lambda}\right) & -i\kappa_{dc,(2,1)} & -i\kappa_{ac,(-1,1)} & -i\kappa_{ac,(-2,1)} \\ -i\kappa_{dc,(1,2)} & -i\left(\kappa_{dc,2} + \beta_2 - \frac{\pi N}{\Lambda}\right) & -i\kappa_{ac,(-1,2)} & -i\kappa_{ac,(-2,2)} \\ i\kappa_{ac,(1,-1)} & i\kappa_{ac,(2,-1)} & i\left(\kappa_{dc,(-1,-1)} + \beta_1 - \frac{\pi N}{\Lambda}\right) & i\kappa_{dc,(-2,-1)} \\ i\kappa_{ac,(1,-2)} & i\kappa_{ac,(2,-2)} & i\kappa_{dc,(-1,-2)} & i\left(\kappa_{dc,(-2,-2)} + \beta_2 - \frac{\pi N}{\Lambda}\right) \end{pmatrix} \tag{6.37}$$

This result shows that the z dependence can be eliminated from the matrix, allowing for the system to be treated as an usual state matrix system.

6.5.1 Solving the linear state system

The result in the last section can be summarised by the equation below, where $\mathbf{b}$ represents the vectors of B_m (as was shown explicitly in equation 6.36 for a fibre with two modes).

$$\frac{\partial}{\partial z}\boldsymbol{b} = \boldsymbol{M_B}\boldsymbol{b} \tag{6.38}$$

If $\boldsymbol{M_B}$ is diagonalisable, then the system of differential equation can be decoupled, where $\mathbf{D}$ is a diagonal matrix of the eigenvalues of $\mathbf{M_B}$, $\mathbf{V}$ is the matrix of eigenvectors of $\mathbf{M_B}$ and the notation $\mathbf{p} = \mathbf{V}^{-1}\mathbf{b}$ is used.

$$\boldsymbol{M_B} = \boldsymbol{V}\boldsymbol{D}\boldsymbol{V^{-1}} \tag{6.39}$$

$$\frac{\partial}{\partial z}(\boldsymbol{V^{-1}}\boldsymbol{b}) = \boldsymbol{D}\boldsymbol{V^{-1}}\boldsymbol{b} \tag{6.40}$$

$$\frac{\partial}{\partial z}\boldsymbol{p} = \boldsymbol{D}\boldsymbol{p} \tag{6.41}$$

This is a set of decoupled ordinary differential equations, which can be solved through direct integration.

$$\frac{dp_h(z)}{dz} = \lambda_h p_h(z) \Leftrightarrow \frac{dp_h(z)}{p_h(z)} = \lambda_h dz \tag{6.42}$$

$$p_h(z) = p_h(0)e^{\lambda_h z} \tag{6.43}$$

$$\boldsymbol{p}(z) = e^{\boldsymbol{D}z}\boldsymbol{p}(0) \tag{6.44}$$

$$\begin{aligned} \boldsymbol{V}^{-\mathbf{1}}\boldsymbol{b}(z) &= e^{\boldsymbol{D}z}\boldsymbol{V}^{-\mathbf{1}}\boldsymbol{b}(0) \\ \boldsymbol{b}(z) &= \boldsymbol{V}e^{\boldsymbol{D}z}\boldsymbol{V}^{-\mathbf{1}}\boldsymbol{b}(0) \end{aligned} \tag{6.45}$$

Before focusing on initial conditions, a discussion on the relationship between $\boldsymbol{a}$, $\boldsymbol{b}$ and the total transverse electric field needs to be made.

In the analytical approach, the total transverse electric field was taken as:

$$E_t(z) = \sum_{h=1}^{N_{modes}} A_h e^{i(\omega t - \beta_h z)} + \sum_{-h=-1}^{-N_{modes}} A_{-h} e^{i(\omega t + \beta_h z)} \tag{6.46}$$

Thus, it is clear that $\boldsymbol{A}$ does not take into account the phase shift due to propagation. However, using the relationship between $\boldsymbol{A}$ and $\boldsymbol{B}$ from last section, the transverse electric field can be written as:

$$\begin{aligned} E_t(z) &= \sum_{h=1}^{N_{modes}} B_h e^{i(\beta_h - \frac{\pi N}{\Lambda})z} e^{i(\omega t - \beta_h z)} + \sum_{-h=-1}^{-N_{modes}} B_{-h} e^{i(-\beta_h + \frac{\pi N}{\Lambda})z} e^{i(\omega t + \beta_h z)} \\ E_t(z) &= \sum_{h=1}^{N_{modes}} B_h e^{i(\omega t - \frac{\pi N}{\Lambda} z)} + \sum_{-h=-1}^{-N_{modes}} B_{-h} e^{i(\omega t + \frac{\pi N}{\Lambda} z)} \end{aligned} \tag{6.47}$$

Thus, $\boldsymbol{b}$ represents the mode coefficients with propagation taken into account, but with an extra opposite phase shift for FP and BP modes. This allows for applying initial conditions directly to the $\boldsymbol{b}$ coefficients.

The initial conditions applied will be setting $E_{t,FP}(z=0)$ to the field at the beginning of the grating and $E_{t,BP}(z=L)$ the back-propagating field at the end of the grating. In practice, the latter can be set to 0, assuming no other reflections occur after the grating and that no light is being inputted from the distal facet.

In other words, the initial conditions are $B_h(z=0)$ and $B_{-h}(z=L)$ (which could be 0).

Let the parameters be split between BP (-) and FP (+) modes:

$$\boldsymbol{b} = \begin{pmatrix} \boldsymbol{b}_+ \\ \boldsymbol{b}_- \end{pmatrix} \tag{6.48}$$

$$\boldsymbol{V} e^{\boldsymbol{D}L} \boldsymbol{V}^{-\mathbf{1}} = \begin{pmatrix} \boldsymbol{S}_{++} & \boldsymbol{S}_{+-} \\ \boldsymbol{S}_{-+} & \boldsymbol{S}_{--} \end{pmatrix} \tag{6.49}$$

Then:

$$\begin{cases} \boldsymbol{b}_+(z=L) = \boldsymbol{S}_{++}\boldsymbol{b}_+(z=0) + \boldsymbol{S}_{+-}\boldsymbol{b}_-(z=0) \\ \boldsymbol{b}_-(z=L) = \boldsymbol{S}_{-+}\boldsymbol{b}_+(z=0) + \boldsymbol{S}_{--}\boldsymbol{b}_-(z=0) \end{cases} \tag{6.50}$$

Which leads to:

$$\begin{cases} \boldsymbol{b}_-(z=0) = \boldsymbol{S}_{--}^{-1}\left[\boldsymbol{b}_-(z=L) - \boldsymbol{S}_{-+}\boldsymbol{b}_+(z=0)\right] \\ \boldsymbol{b}_+(z=L) = \boldsymbol{S}_{++}\boldsymbol{b}_+(z=0) + \boldsymbol{S}_{+-}\boldsymbol{b}_-(z=0) \end{cases} \tag{6.51}$$

6.6 Discussion on non-sinusoidal gratings

The approach in section 6.2 as well as the approach detailed in subsection 6.4 focus on sinusoidal gratings. In practice, such gratings would be hard to manufacture. However, any periodical grating can be described through the use of Fourier series. Or to be more specific:

$$\delta n = a_0 + \sum_{k=1}^{\infty} a_k \cos\left(\frac{2\pi k}{\Lambda} z\right) + \sum_{k=1}^{\infty} b_k \sin\left(\frac{2\pi k}{\Lambda} z\right) \tag{6.52}$$

If the assumption is made that only the DC component and a single harmonic order provide coupling, due to choosing the grating to specifically filter a wavelength, then the grating will act as if its a sinusoid:

$$\delta n = a_0 + a_N \cos\left(\frac{2\pi N}{\Lambda} z\right) + b_N \sin\left(\frac{2\pi N}{\Lambda} z\right) \tag{6.53}$$

This can be further rewritten as:

$$\delta n = a_0 + \sqrt{a_N^2 + b_N^2} \cos\left(\frac{2\pi N}{\Lambda} z + \phi\right) \tag{6.54}$$

where:

$$\sin(\phi) = \frac{-b_N}{\sqrt{a_N^2 + b_N^2}} \tag{6.55}$$

If the assumption is made that the core refractive index is one of the limits of the refractive index variation (or similarly 0 is either the upper or lower limit of δn) and that the variation is symmetric with respect to z, then δn is an even function, where $z = 0$ is the start of the grating, thus, the sine terms in the Fourier series become 0, leading to:

$$\delta n = a_0 + a_N \cos\left(\frac{2\pi N}{\Lambda} z\right) \tag{6.56}$$

The form in equation 6.56 is identical to equation 6.12.

6.7 Implementation of the theory in a simulation

6.7.1 Focus simulation

The theory described has been implemented in Matlab. In terms of the simulation parameters, the grating chosen was a line across the fibre core as shown in figure 30. While the discussion in the previous chapters have used reflectors very small in size, the first simulation has been done on a grating with a different geometry. The reason for such change is that a line grating is closer to what can already be more easily achieved in practice, thus, to provide and initial investigation into a grating which has a higher change of being tested experimentally. However, this chapter will also investigate later gratings which are small in size. The target of the first simulation was to test the approach, that it gives a reasonable answer and that it can be used for localising the focus, whether it is on the grating or not.

The grating parameters were:

- Pitch: 534.9 nm, designed for a Bragg wavelength of 515 nm (third order - $N = 3$)
- Cross-sectional area: ~ 30 μm by ~ 2 μm
- Length of the grating: ~ 5 mm

The grating profile was chosen to be a two-dimensional Gaussian distribution, setting the maximum change in refractive index at 0.02. The relationship between the DC refractive index change and the amplitude of the AC refractive index change was set as: $\overline{\Delta n} = -\Delta n$, such that the change in refractive index δn at the beginning of the grating at $z = 0$ is 0 (see equation 6.12).

The simulation was done after generating the set of fibre modes for a light wavelength identical to the Bragg wavelength. Then the procedure described in the previous subsections was followed.

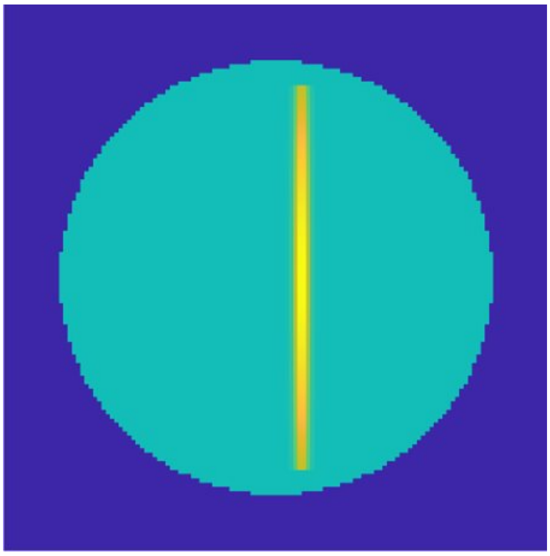

Figure 30: The refractive index change profile of the simulated sample. The colours in the figure represent: dark blue - the cladding of the fibre, cyan to yellow - the amplitude of the sinusoidal change in refractive index profile (Δn) from 0 (cyan) to 0.02 (yellow). The value of the DC change is the opposite ($\overline{\Delta n} = -\Delta n$) in order for the total refractive index change at z=0 to be 0.

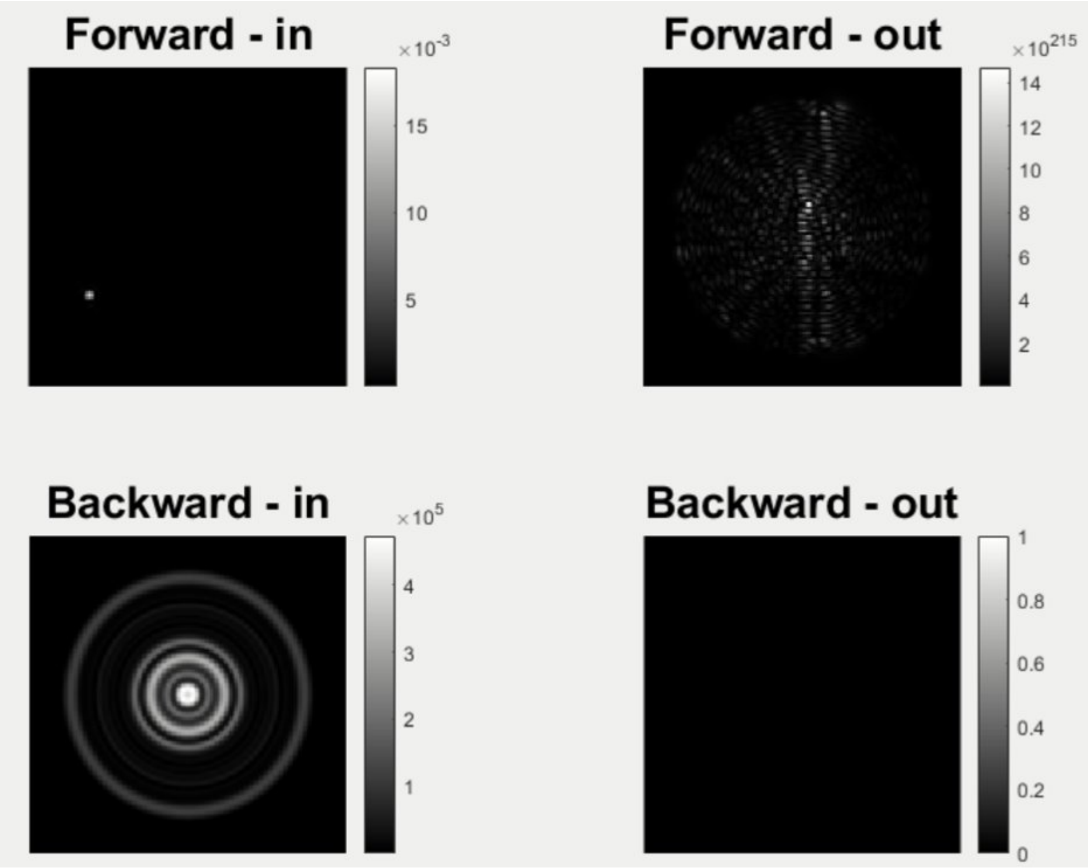

Figure 31: Initial simulation result for the Bragg grating, given by focusing input light at a location away from the grating.

Only the portion of the fibre containing the grating was simulated by specifying the optical field at the beginning of the grating. The first set of initial conditions, the forward input optical field at $z = 0$, was generated by focusing input light at different positions. The second set of initial conditions, the backward optical field at $z = L$, was chosen such that there was no light entering the grating from the output end. The target result of the simulation is the light exiting the grating at both ends of the fibre section.

The initial result for an input focus is given in figure 31. The "Forward-in" panel shows the location of the input focus. The "Forward-out" and "Backward-in" panels show the light exiting at the output end and the input end, respectively. The last quadrant ("Backward-out") represents the light entering in the backward direction at the output end, which is shown to be set to 0.

It is clear that there is a problem. The input focus intensity is in the range of $2 \cdot 10^{-3}$, while the forward light is in the range of 10^{215}. The reflected light is also several orders of magnitude larger than the input light. Thus, the simulation shows an increase in total energy, which is not possible in reality.

In order to understand why this effect occurs, a look has been given at the eigenvalues of the matrix $\mathbf{M_B}$, the results being shown in figure 32.

The blue plot shows the cosine of the argument of the eigenvalue. This illustrates which eigenvalues are purely imaginary (value of 0), purely real (value of ± 1), or in-between. While most eigenvalues are purely imaginary, some of them are not.

However, in order to understand better where which eigenvalues contribute more to the exponential amplification, the orange plot shows on a logarithmic scale the real part of the eigenvalue. The absolute value of the real part has been used in order to include negative value as well. While a negative real part might seem to imply exponential decay, the forward and backward propagations are in opposite directions, thus the component of one will decay while the other will amplify as it propagates.

It is clear that the eigenvalues are split into two groups: the first group has real values in the 10^{-10} range, which are within numerical errors of a purely imaginary eigenvalue, while the second group are in the range of 10^0 to 10^5. The second group and more specifically the eigenvalues which have a larger real part are the problem in this situation.

An important note to mention is that the sum of the eigenvalues is 0, as the trace of $\mathbf{M_B}$ is 0. This implies that the determinant of $\mathbf{S} = e^{\mathbf{M_B}L}$ is 1. In practice, the resulting $\mathbf{S}$ had a determinant of $+\infty$, which is the value allocated by Matlab for a very large determinant. This might mean that there is some numerical error which occurs due to the large real parts of the eigenvalues when calculating the matrix exponential. Thus, it could be that working in the scattering modal space might be a better approach to have greater care in using the very large eigenvalues.

An interesting idea was observed in [33], where the propagation of evanescent fields in stratified media was encountered. The main observation was that due to the exponential evolution of such fields, a numerical stable approach was to consider light fields exiting out of the system at both ends as a function of light fields entering into the system at both ends. This is different to the approach described which considers the light fields, entering and exiting, at one end of the optical system as a function of the light fields, entering and exiting, at the other end. Their approach focused on treating each field individually, however, in the Bragg grating case this would be very complex to compute, as each period of the grating would represent a section of the system. However, the idea of relating inputs to outputs can still be used.

Taking the equation 6.45 and using the notations $\mathbf{q} = \mathbf{V}^{-1}\mathbf{b}(z = L)$ and

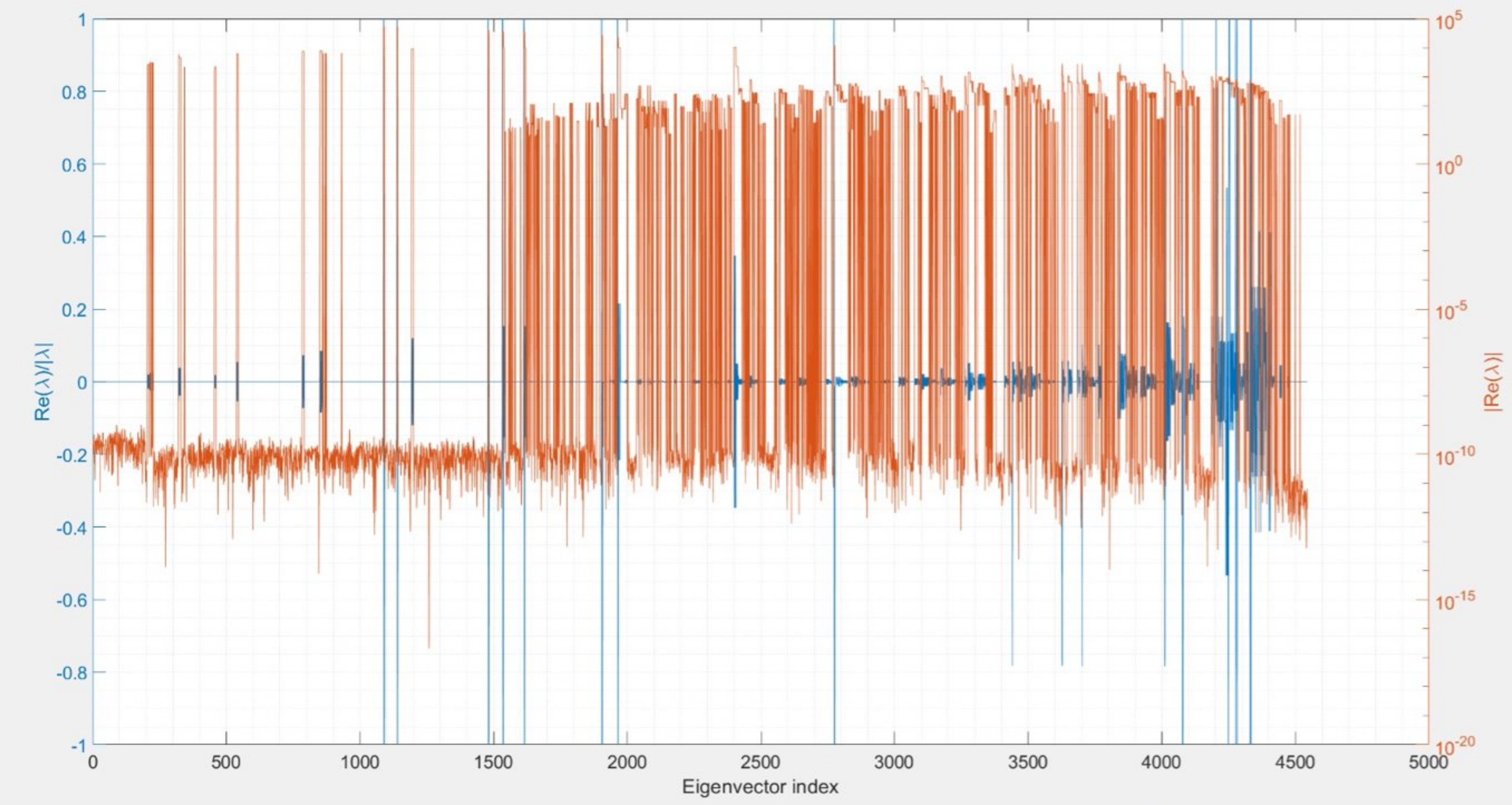

Figure 32: A plot of the eigenvalues of the matrix $\mathbf{M_B}$ for the simulated grating. The horizontal axis represents the index of the eigenvalue. The left vertical axis (blue) represents the cosine of the argument of the eigenvalue. The right vertical axis (orange) represents a logarithmic plot of the absolute value of the real part of the eigenvalue.

$\mathbf{p} = \mathbf{V}^{-1}\mathbf{b}(z=0)$ leads to:

$$\mathbf{q} = e^{\mathbf{D}L}\mathbf{p} \tag{6.57}$$

If the rows of the equation are reordered and separated into positive (index +) and negative (index -) real parts of the eigenvalues' exponent, equation 6.57 can be written as:

$$\begin{pmatrix} \boldsymbol{q}_+ \\ \boldsymbol{q}_- \end{pmatrix} = \begin{pmatrix} e^{\mathbf{D}_+L} & 0 \\ 0 & e^{\mathbf{D}_-L} \end{pmatrix} \begin{pmatrix} \boldsymbol{p}_+ \\ \boldsymbol{p}_- \end{pmatrix} \tag{6.58}$$

The individual exponent terms in the matrix are diagonal matrices, thus, the positive real part rows can be inverted to only work with negative real parts and avoid exponential gain (i.e. a constituent equation in the form $q_k = e^{D_kL}p_k$ was changed to $p_k = e^{-D_kL}q_k$, where $D_k > 0$).

$$\begin{pmatrix} \boldsymbol{p}_+ \\ \boldsymbol{q}_- \end{pmatrix} = \begin{pmatrix} e^{-\mathbf{D}_+L} & 0 \\ 0 & e^{\mathbf{D}_-L} \end{pmatrix} \begin{pmatrix} \boldsymbol{q}_+ \\ \boldsymbol{p}_- \end{pmatrix} \tag{6.59}$$

The next step is to expand $\mathbf{p}$ and $\mathbf{q}$, however, beforehand, the matrix $\mathbf{V}^{-1}$ needs to be reordered to match the new order of $\mathbf{p}$ and $\mathbf{q}$. The order of the columns of $\mathbf{V}^{-1}$ was kept the same, as the order of the modes ($\mathbf{b}(L)$ and $\mathbf{b}(0)$) was not changed. A reminder is given that they were split into two sets based on the propagation direction of the fibre modes they are related to ($b+$ for FP modes and $b-$ for BP modes). The order of the rows of $\mathbf{V}^{-1}$ was changed to separate and split the eigenvectors they relate to into two sets based on the sign of the real part of their associated eigenvalue exponent ($r+$ for positive real part and $r-$ for negative real part). This allows for the new reordered $\mathbf{V}^{-1}$ to be separated into four sub-matrices:

$$\mathbf{q}_{reordered} = \mathbf{V}_{reordered}^{-1}\mathbf{b}(L) \quad \mathbf{p}_{reordered} = \mathbf{V}_{reordered}^{-1}\mathbf{b}(0)$$

$$\begin{pmatrix} \boldsymbol{q}_{+} \\ \boldsymbol{q}_{-} \end{pmatrix} = \begin{pmatrix} \boldsymbol{V}_{r+b+}^{-1} & \boldsymbol{V}_{r+b-}^{-1} \\ \boldsymbol{V}_{r-b+}^{-1} & \boldsymbol{V}_{r-b-}^{-1} \end{pmatrix} \begin{pmatrix} \boldsymbol{b}_{+}(L) \\ \boldsymbol{b}_{-}(L) \end{pmatrix}$$

$$\begin{pmatrix} \boldsymbol{p}_{+} \\ \boldsymbol{p}_{-} \end{pmatrix} = \begin{pmatrix} \boldsymbol{V}_{r+b+}^{-1} & \boldsymbol{V}_{r+b-}^{-1} \\ \boldsymbol{V}_{r-b+}^{-1} & \boldsymbol{V}_{r-b-}^{-1} \end{pmatrix} \begin{pmatrix} \boldsymbol{b}_{+}(0) \\ \boldsymbol{b}_{-}(0) \end{pmatrix} \tag{6.60}$$

Writing $\mathbf{p}_{-}$, $\mathbf{p}_{+}$, $\mathbf{q}_{-}$ and $\mathbf{q}_{+}$ in terms of $\mathbf{b}_{-}(0)$, $\mathbf{b}_{+}(0)$, $\mathbf{b}_{-}(L)$ and $\mathbf{b}_{+}(L)$ and introducing them into equation 6.59 leads to:

$$\begin{pmatrix} \boldsymbol{p}_{+} \\ \boldsymbol{q}_{-} \end{pmatrix} = \begin{pmatrix} \boldsymbol{V}_{r+b+}^{-1} & \boldsymbol{V}_{r+b-}^{-1} & 0 & 0 \\ 0 & 0 & \boldsymbol{V}_{r-b+}^{-1} & \boldsymbol{V}_{r-b-}^{-1} \end{pmatrix} \begin{pmatrix} \boldsymbol{b}_{+}(\boldsymbol{0}) \\ \boldsymbol{b}_{-}(\boldsymbol{0}) \\ \boldsymbol{b}_{+}(\boldsymbol{L}) \\ \boldsymbol{b}_{-}(\boldsymbol{L}) \end{pmatrix} = \mathbf{M}_1 \begin{pmatrix} \boldsymbol{b}_{+}(\boldsymbol{0}) \\ \boldsymbol{b}_{-}(\boldsymbol{0}) \\ \boldsymbol{b}_{+}(\boldsymbol{L}) \\ \boldsymbol{b}_{-}(\boldsymbol{L}) \end{pmatrix}$$

$$\begin{pmatrix} \boldsymbol{q}_{+} \\ \boldsymbol{p}_{-} \end{pmatrix} = \begin{pmatrix} 0 & 0 & \boldsymbol{V}_{r+b+}^{-1} & \boldsymbol{V}_{r+b-}^{-1} \\ \boldsymbol{V}_{r-b+}^{-1} & \boldsymbol{V}_{r-b-}^{-1} & 0 & 0 \end{pmatrix} \begin{pmatrix} \boldsymbol{b}_{+}(0) \\ \boldsymbol{b}_{-}(0) \\ \boldsymbol{b}_{+}(L) \\ \boldsymbol{b}_{-}(L) \end{pmatrix} = \mathbf{M}_2 \begin{pmatrix} \boldsymbol{b}_{+}(0) \\ \boldsymbol{b}_{-}(0) \\ \boldsymbol{b}_{+}(L) \\ \boldsymbol{b}_{-}(L) \end{pmatrix}$$

$$\mathbf{M}_1 \begin{pmatrix} \boldsymbol{b}_{+}(\boldsymbol{0}) \\ \boldsymbol{b}_{-}(\boldsymbol{0}) \\ \boldsymbol{b}_{+}(\boldsymbol{L}) \\ \boldsymbol{b}_{-}(\boldsymbol{L}) \end{pmatrix} = \begin{pmatrix} e^{-\mathbf{D}_{+}L} & 0 \\ 0 & e^{\mathbf{D}_{-}L} \end{pmatrix} \mathbf{M}_2 \begin{pmatrix} \boldsymbol{b}_{+}(\boldsymbol{0}) \\ \boldsymbol{b}_{-}(\boldsymbol{0}) \\ \boldsymbol{b}_{+}(\boldsymbol{L}) \\ \boldsymbol{b}_{-}(\boldsymbol{L}) \end{pmatrix} \tag{6.61}$$

In equation 6.61, taking the right hand side to the left leads to:

$$\left[\mathbf{M}_1 - \begin{pmatrix} e^{-\mathbf{D}_+ L} & 0 \\ 0 & e^{\mathbf{D}_- L} \end{pmatrix} \mathbf{M}_2\right] \begin{pmatrix} \boldsymbol{b}_+(\boldsymbol{0}) \\ \boldsymbol{b}_-(\boldsymbol{0}) \\ \boldsymbol{b}_+(\boldsymbol{L}) \\ \boldsymbol{b}_-(\boldsymbol{L}) \end{pmatrix} = 0$$

$$\boldsymbol{M} \begin{pmatrix} \boldsymbol{b}_+(\boldsymbol{0}) \\ \boldsymbol{b}_-(\boldsymbol{0}) \\ \boldsymbol{b}_+(\boldsymbol{L}) \\ \boldsymbol{b}_-(\boldsymbol{L}) \end{pmatrix} = 0 \tag{6.62}$$

The matrix $\mathbf{M}$ can be calculated using only the eigenvalues and eigenvectors of $\mathbf{M}_B$ and, due to only containing exponents with negative real parts, it is avoiding any numerical issues occurring due to exponential gain. Splitting $\mathbf{M}$ along the columns into 4 sub-matrices, each associated with a component of the column vector and taking $\mathbf{b}_+(0)$ and $\mathbf{b}_-(L)$ as known initial conditions leads to the solution in equation 6.63. In terms of dimensions, $\mathbf{M}$ is a matrix of $2N_m$ rows by $4N_m$ columns, where N_m is the number of fibre modes. Thus, each sub-matrix will be of size $2N_m$ by N_m and two sub-matrices together form a square matrix, allowing for the inversion to occur, assuming the determinant is not 0.

$$\begin{pmatrix} \boldsymbol{M}_{b+(0)} & \boldsymbol{M}_{b-(0)} & \boldsymbol{M}_{b+(L)} & \boldsymbol{M}_{b-(L)} \end{pmatrix} \begin{pmatrix} \boldsymbol{b}_+(\boldsymbol{0}) \\ \boldsymbol{b}_-(\boldsymbol{0}) \\ \boldsymbol{b}_+(\boldsymbol{L}) \\ \boldsymbol{b}_-(\boldsymbol{L}) \end{pmatrix} = 0$$

$$\begin{pmatrix} \boldsymbol{M}_{b+(0)} & \boldsymbol{M}_{b-(L)} \end{pmatrix} \begin{pmatrix} \boldsymbol{b}_+(0) \\ \boldsymbol{b}_-(L) \end{pmatrix} + \begin{pmatrix} \boldsymbol{M}_{b-(0)} & \boldsymbol{M}_{b+(L)} \end{pmatrix} \begin{pmatrix} \boldsymbol{b}_-(0) \\ \boldsymbol{b}_+(L) \end{pmatrix} = 0$$

$$\begin{pmatrix} \boldsymbol{b}_-(0) \\ \boldsymbol{b}_+(L) \end{pmatrix} = \begin{pmatrix} \boldsymbol{M}_{b-(0)} & \boldsymbol{M}_{b+(L)} \end{pmatrix}^{-1} \begin{pmatrix} -\boldsymbol{M}_{b+(0)} & -\boldsymbol{M}_{b-(L)} \end{pmatrix} \begin{pmatrix} \boldsymbol{b}_+(0) \\ \boldsymbol{b}_-(L) \end{pmatrix} \tag{6.63}$$

The approach described above has been implemented into code and the previously described grating was simulated, the results being shown in figure 33. Two cases were simulated, where the focus was either on or away from the grating to observe the ability of the grating to localise the reflection. It is clear that for a 5 mm grating there is no localisation occurring, in both cases the amount of light reflected being similar to the amount of light passing through. However, the grating seems to be confining the light within or outside its cross-sectional area. This implies that the grating behaves as a waveguide within the fibre core.

To illustrate the reason why a longer grating cannot localise the reflection, figure 34 shows the evolution of the light field inside the core of a fibre given a focus at a specific location within the core. It is clear that, while the light is localised close to the focus location, it expands to almost the entire core within 200 μm of the focus plane. Thus, a grating 5 mm long would interact with the light field no matter where the light is focused as, eventually, within its length, the light will reach the grating.

However, for the grating to be used as a reflector, the grating must be short in order to localise the reflection axially. Thus, in figure 35 the same grating was simulated, but with its length set to 5 μm. It is clear that in this case the reflection amount is dependent on the focus location. In the case of focusing on the grating, the reflection has about 15% of the input intensity and it is localised. The light which passes through the grating is slightly affected, the change will be required to be investigated if it affects the excitation focus quality.

In the case of focusing away from the grating, the light passes almost un-

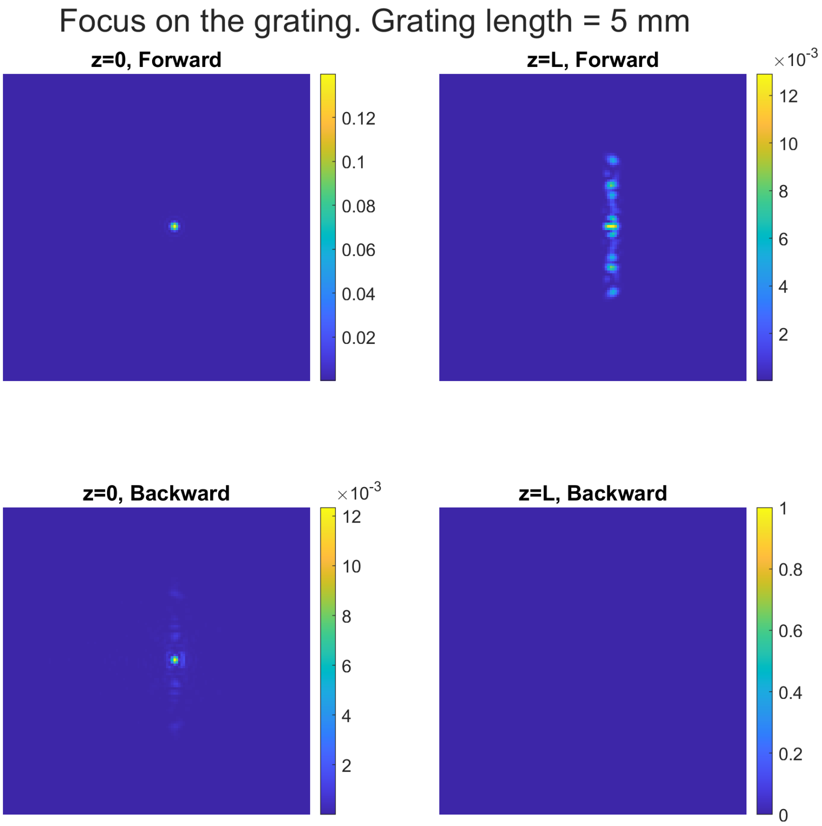

(a) The simulation result for a focus on the grating.

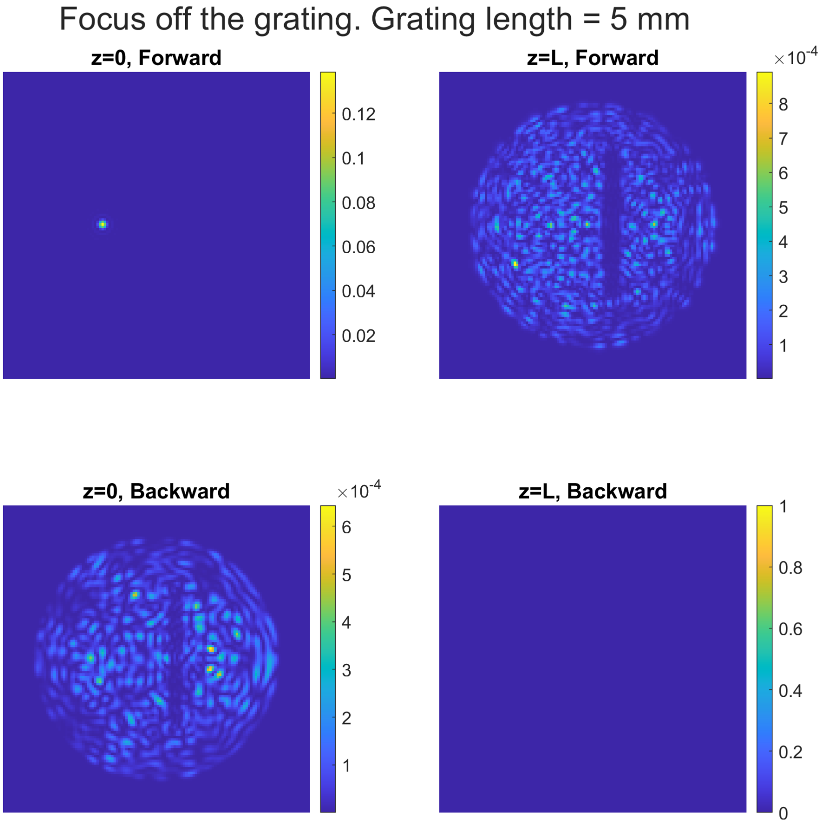

(b) The simulation result for a focus away from the grating.

Figure 33: Simulation results for focusing light on and away from the 5 mm long grating.

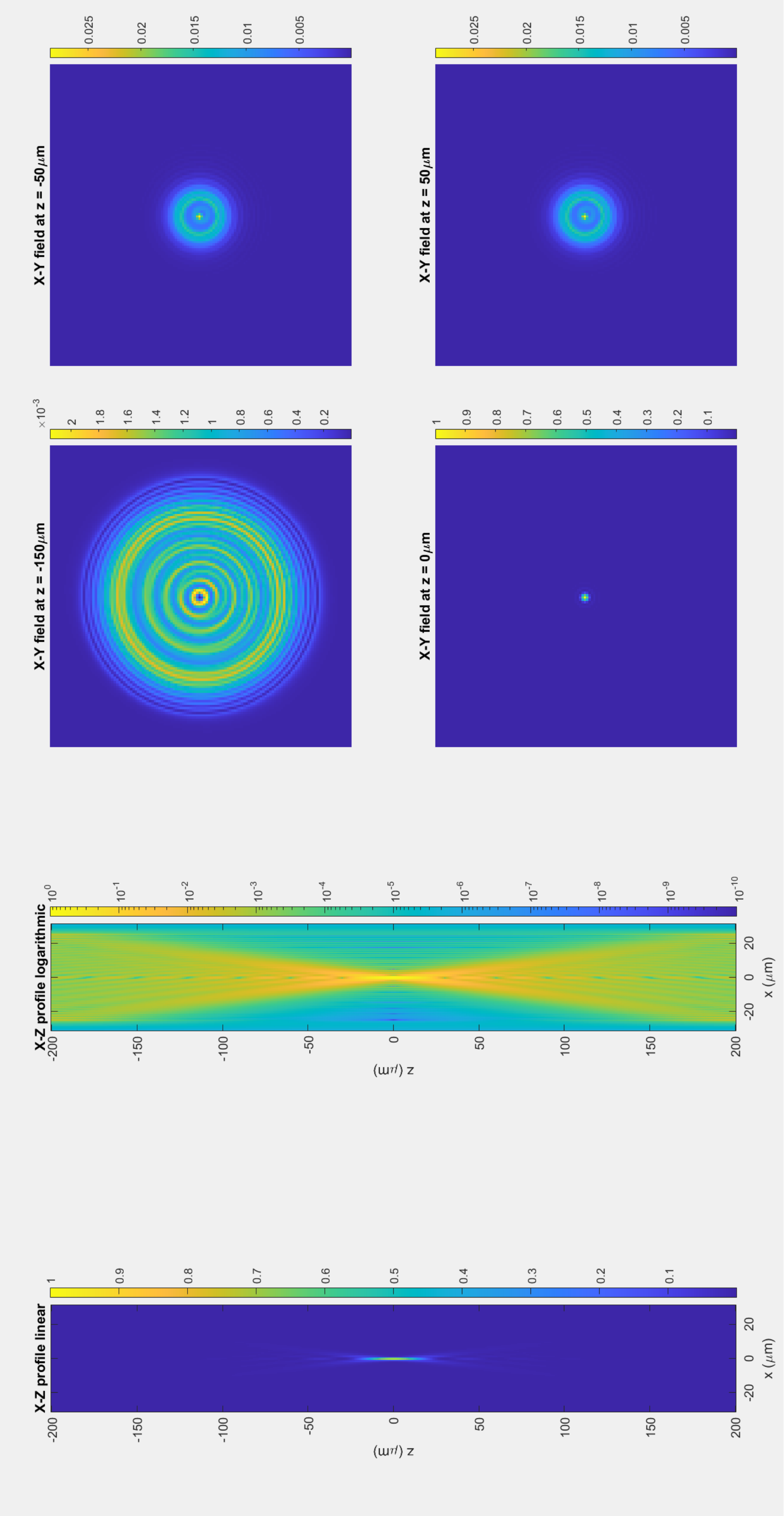

(a) The axial evolution of the light field for a focus in the centre of the core of the fibre.

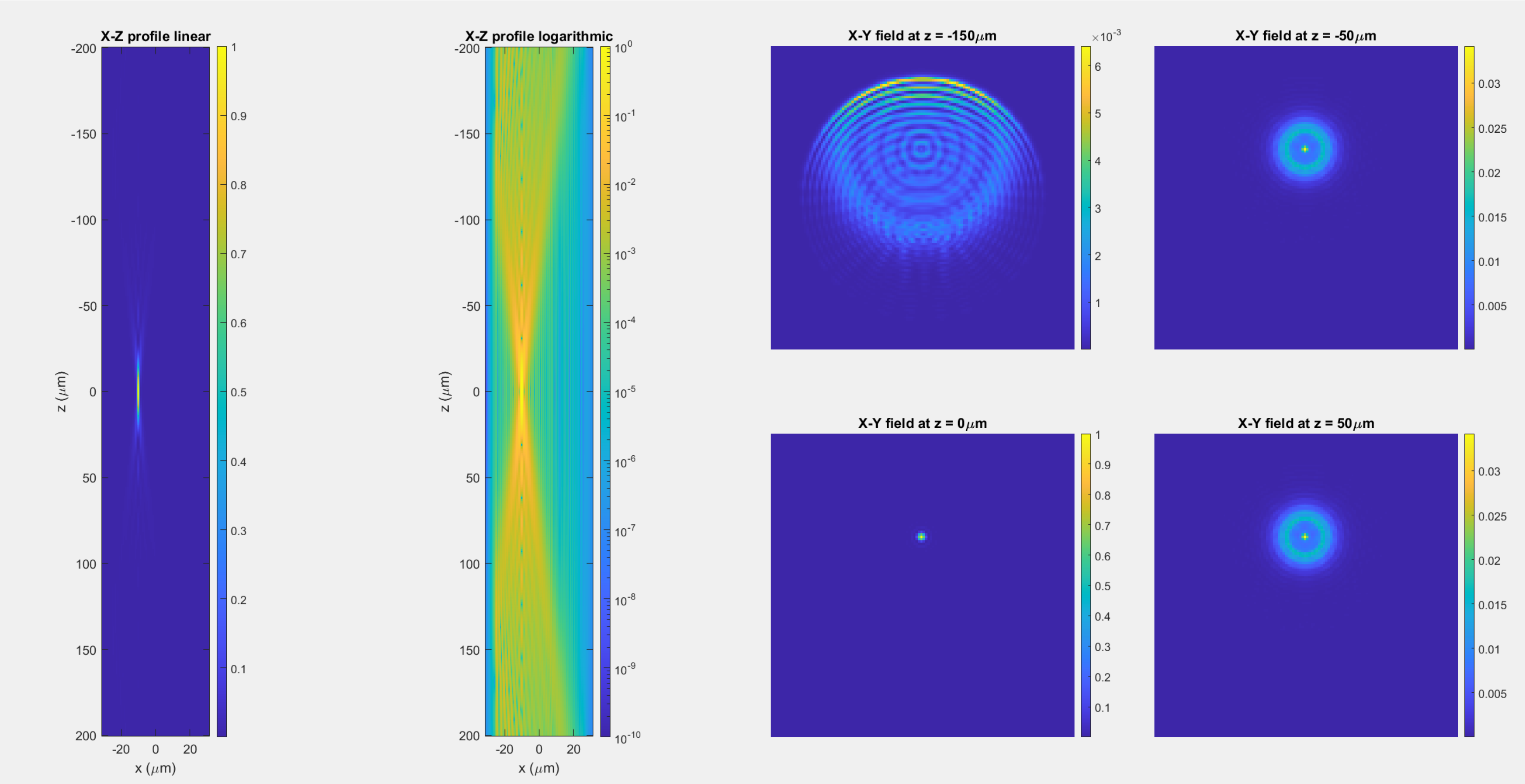

(b) The axial evolution of the light field for a focus to the side of the centre of the core of the fibre.

Figure 34: Simulation results for light field evolution of a focus generated within the core of a fibre. The simulation shows two cases: in the centre and off to the side of the centre of the fibre core. Firstly, the left figures show the axial field evolution of the field intensity along the x-z plane, where z is the axial dimension. Secondly, the right figures show the transversal (x-y) field intensity at different depths (z = -150 μm, -50 μm, 0 μm and 50 μm, where z = 0 μm is the focus plane).

changed. There is still a small amount of reflection, though 4 to 5 orders of magnitude smaller than the input focus. This is due to the focus quality being limited by the fibre modes, thus, some light still exists in the background even with a perfect focus. Thus, a short grating will be able to localise the reflection both in the transversal plane and axially.

6.7.2 Reflection spectrum simulation

One of the most important properties of a Bragg grating is its ability to reflect light within a limited range of wavelengths. Thus, one important property to simulate is the spectrum of the reflected light.

The Bragg grating simulation approach described in this chapter follows a number of steps:

1. Choose the fibre parameters.
2. Compute the set of fibre modes for a specific wavelength of light.
3. Choose grating parameters (excluding length).
4. Compute the $\mathbf{M_B}$ matrix and diagonalise it.
5. Choose a length for the grating and compute the scattering matrix defined in equation 6.63.
6. Choose a set of incoming fields (both forward and backwards propagating) and compute outgoing fields.

In order for a spectrum to be simulated, as the wavelength of the light changes, all of the steps described above, except the first, must be passed through, as the number of modes and their profile will change. This implies that the process to simulate the spectrum is time consuming, depending on the available

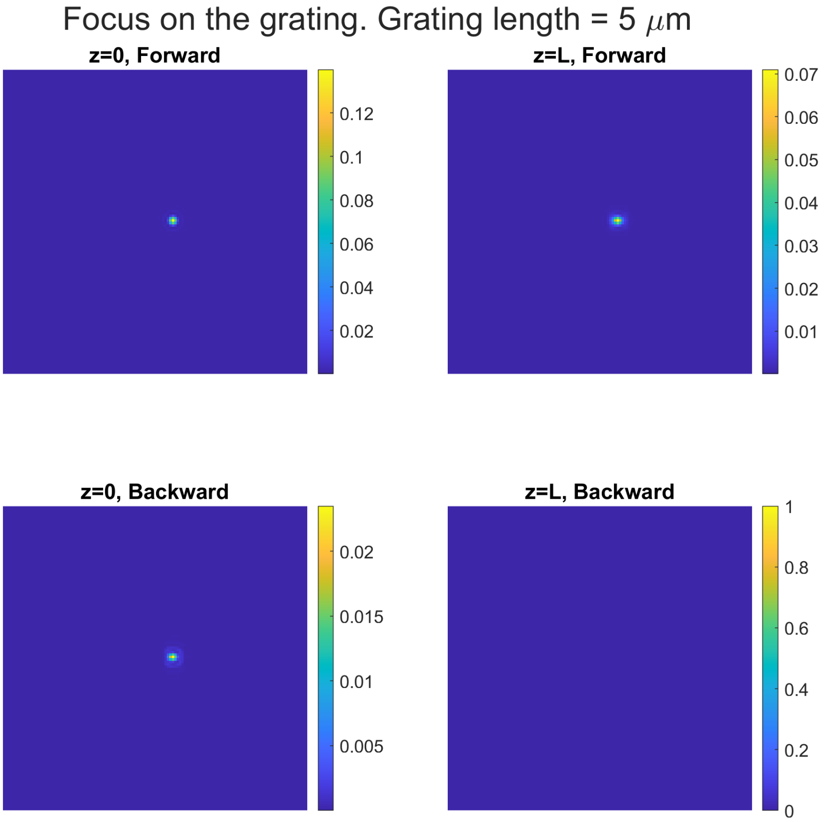

(a) The simulation result for a focus on the grating.

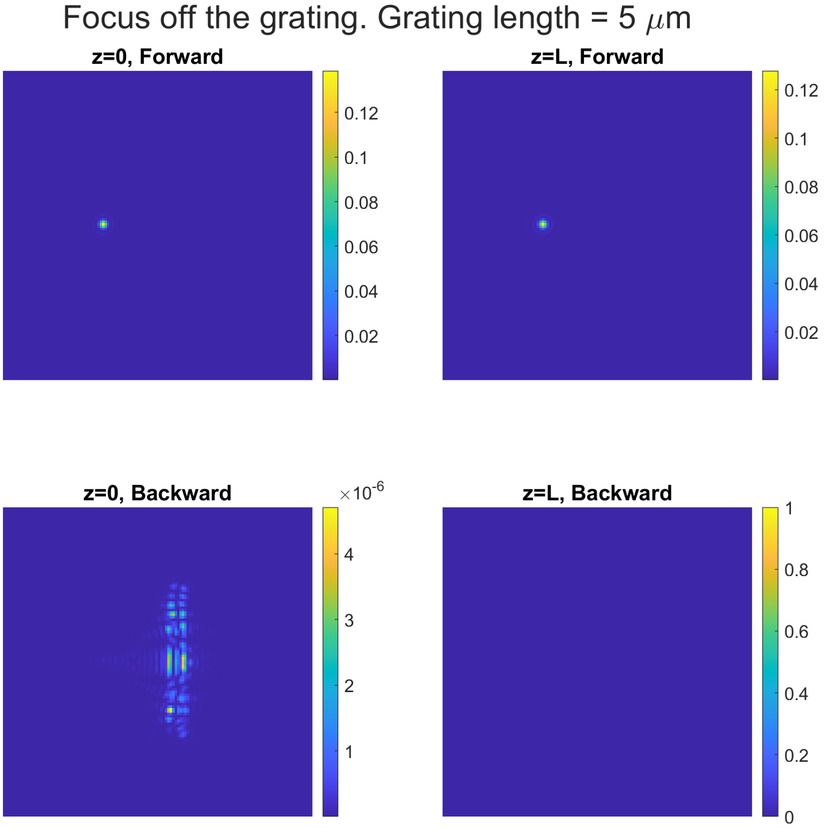

(b) The simulation result for a focus away from the grating.

Figure 35: Simulation results for focusing light on and away from the 5 μm grating.

hardware. However, the advantage of the approach is that as long as some parameters are not changed, steps can be skipped. For example, changing the grating parameters does not require for the fibre modes to be generated again as long as the same fibre is used and the same wavelength range is desired. This is important if a specific grating performance is required and the profile needs to be optimised, while having the wavelength of light and the fibre parameters already be specified.

The first simulation was to compute the spectrum of the grating described in the previous section (6.7.1. The grating period was chosen for a wavelength of 515 nm. The result shown in figure 36, which clearly illustrates that this choice is illustrated in the spectrum of the grating, with a bandwidth of approximately 3 nm.

Another simulation was done for a different Bragg grating. The profile of the grating was changed to be in the centre of the fibre core and the height of the grating increased to cover the entire facet, as shown in figure 37. The parameters of the new grating were:

- Grating period of 1070.3 nm, for Bragg wavelength of 1550 nm (2nd order harmonic)
- Cross-sectional area: height extending more than the core ($> 50\,\mu m$), width $\approx 2\,\mu m$
- Length of 5 mm

While the grating was kept the same, the two different cases for the input light field were chosen: a focus at the centre of the fibre core at the start of the grating and a focus at the centre of the core in the middle of the fibre grating. The results are shown in figure 38. As expected, the spectrum changes between the cases, but it is still around the 1500 nm chosen wavelength. The reason for

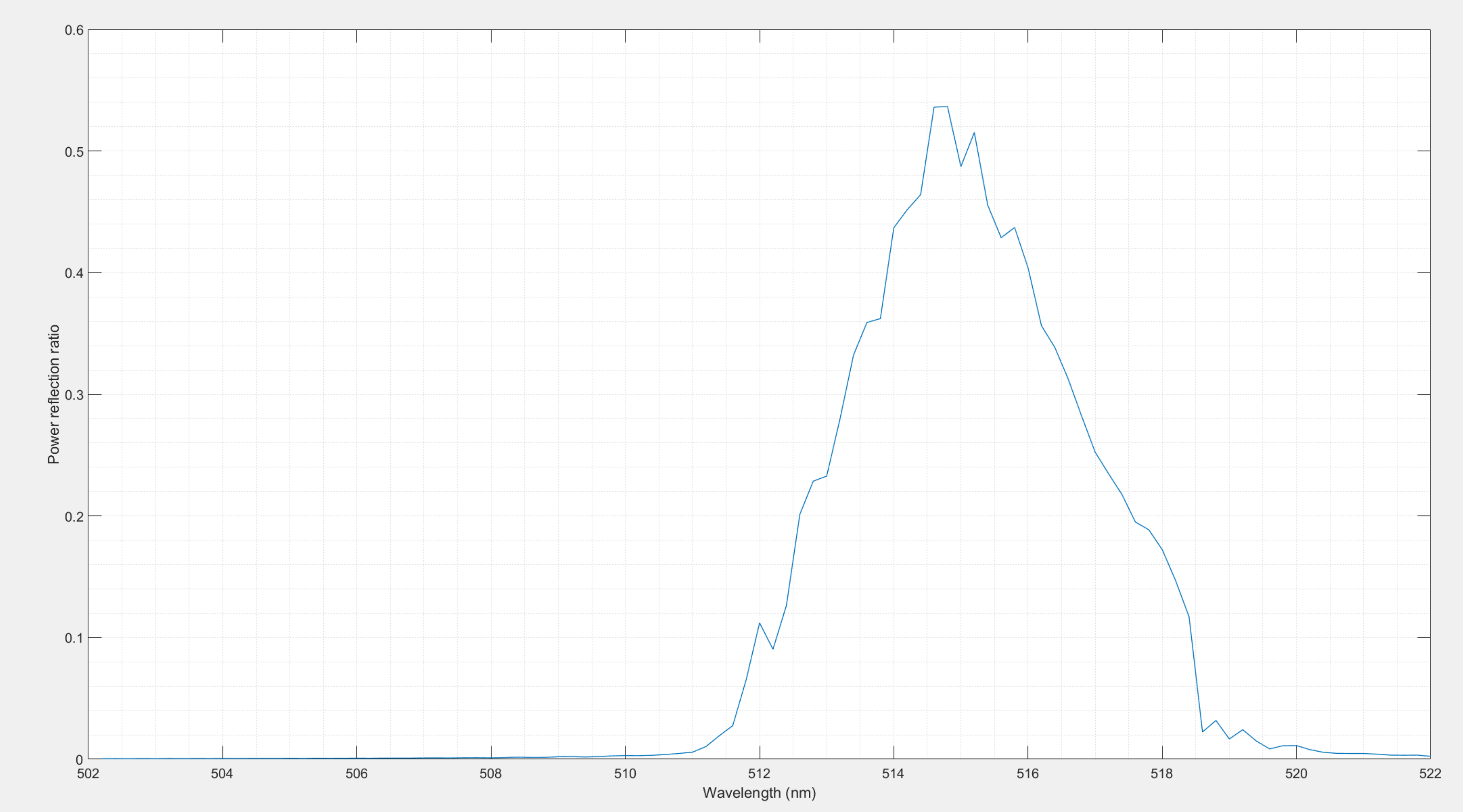

Figure 36: The simulation spectrum result for the grating defined in section 6.7.1. The input was normalised to a total power of 1 W.

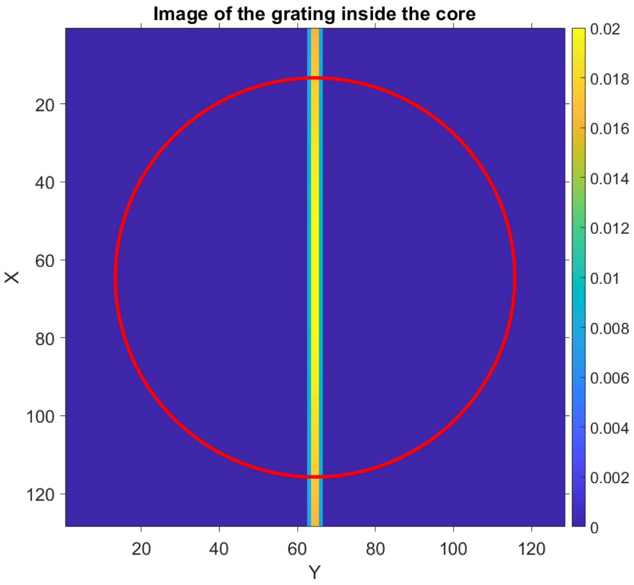

Figure 37: Profile of the refractive index change of the Bragg grating defined for 1500 nm. Red circle indicates the core of the fibre. The simulation window is of size 128×128 pixels, indicated on the x and y axis.

the change is due to modes having a different coefficient. While in both cases it is a focus in the centre of the core, thus, the amplitude of the modal coefficients is identical, the phase components are not. This leads to a difference in the interaction with the grating. This is an important observation to keep in mind when optimising for a desired grating, that the input light is also of importance.

To provide some confirmation to the truthfulness of the simulation, a plot from [34] is shown in figure 38c. The parameters are not identical, as in the cited thesis the grating covers the entire facet, is in a grade index fibre, the input is a field of modes of identical coefficients and the change in refractive index profile is in the order of 2×10^{-4}. However, a similar spectrum is achieved, the thesis specifically indicating that a large refractive index change leads to a wider and more uniform spectrum.

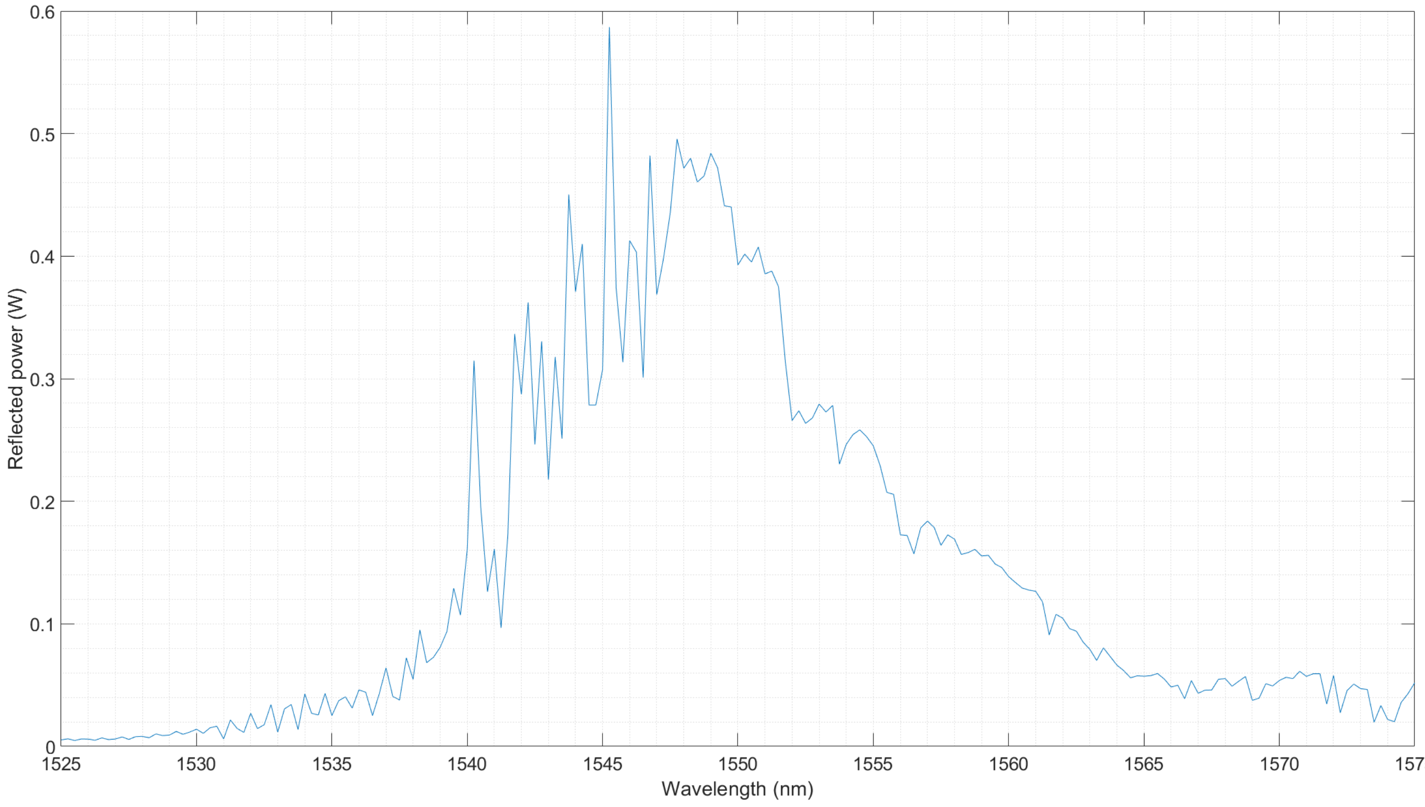

(a) The simulation result for a focus in the centre of the core at the start of the grating.

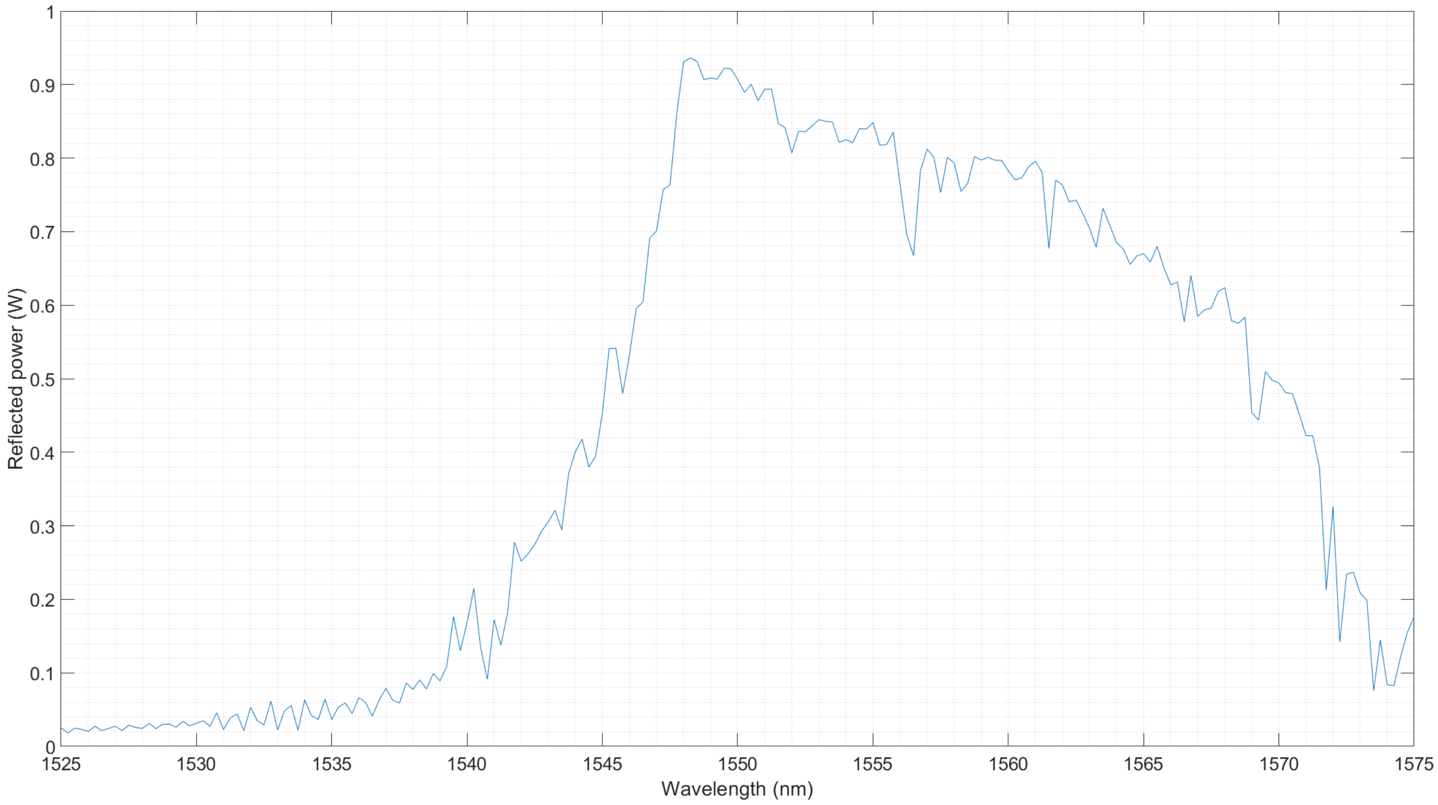

(b) The simulation result for a focus in the centre of the core in the middle of the grating.

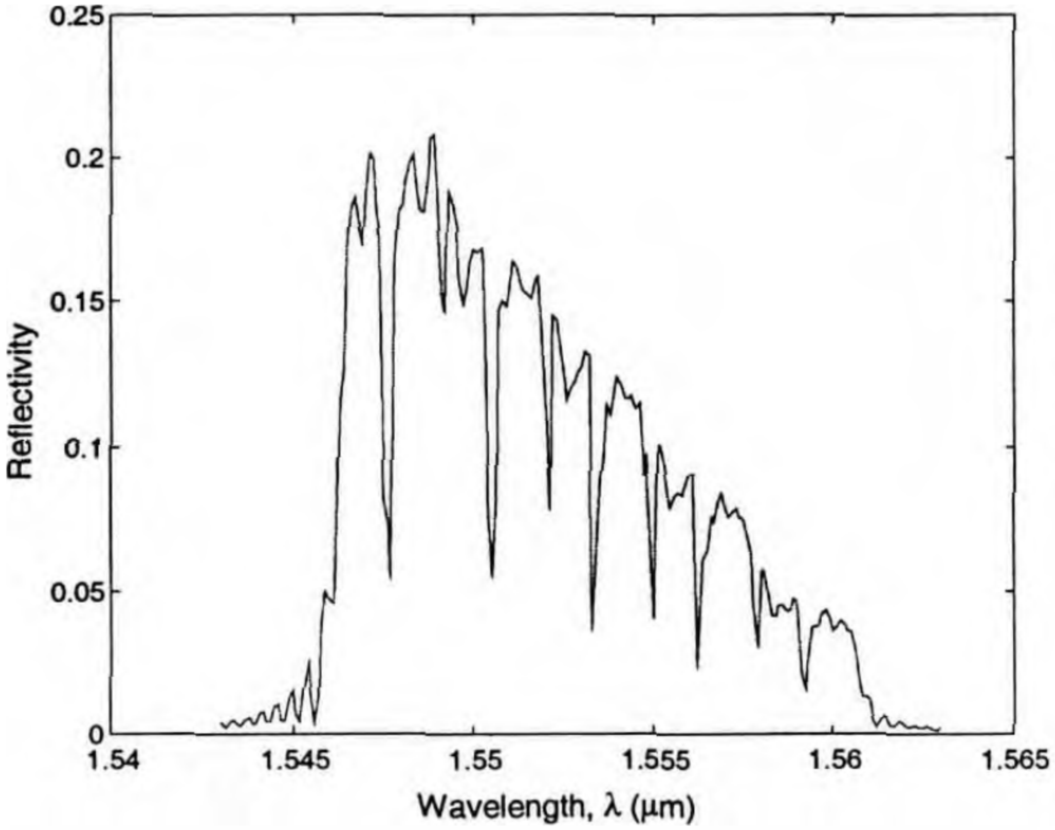

(c) The simulation result, figure 6-5 (b) in [34] for a graded index profile fibre. More info in the text body.

Figure 38: Simulated spectrum of the line Bragg grating defined for a wavelength of 1550 nm.

6.8 Conclusion

In conclusion, this chapters presents a novel approach in simulating Bragg gratings. The advantage of the described approach is that it solves the mode-coupling equation simultaneously, without the resort to more numerical and iterative approaches, which can take a longer time. This allows for a quicker approach in simulating and optimising for the desired Bragg grating depending on the application.

In terms of the main objective of this thesis, the program allows for the computation of the optical field of a given Bragg grating inside a multimode optical fibre as well. This is important if Bragg gratings are to be used as reflectors for a correction approach to bent optical fibres, specifically within the scope of *in vivo* imaging, where one of the ends of the fibre is not accessible during the correction procedure.

A number of simulation results have been shown, however, a more in depth analysis backed by experimental data is required in order to truly validate the approach.

7 Conclusion and outlook

7.1 Conclusion

This thesis had provided an approach to correcting for the change in light transmission through a bent multimode optical fibre for use in *in vivo* microscopy.

The correction method approached the problem in steps, starting with recovering focusing capabilities for a single location at or near the output facet of the fibre. It made use of Walsh-Hadamard modes as an orthogonal basis to characterise the modulation applied by the SLM on the optical field being inputted into the fibre. The advantage of Walsh modes is that varying the coefficient of one of them lead to a sinusoidal variation in the output focus intensity. Such a predictable output allowed for a simple optimisation procedure which would compute the best coefficient with only three measurements at different Walsh mode coefficients. Repeating the optimisation process for different Walsh modes, lead to an iterative process through which the output focus intensity was mostly recovered. This type of process fits into the categorisation of sensorless adaptive optics. The thesis showed through simulations that a significant improvement in the quality of the focus can be achieved, however, this is at the cost of time as the process requires a large number of iterations.

In order to expand the correction from a single location to an area around it, the memory effect was utilised. The approach assumes that for small bends in the fibre, the TM does not change by a large amount and keeps its diagonal form, though with changes in the phase of the elements on the main diagonal. Restricting the assumed form of the TM allows for information about the entire TM to be obtained from the input optical field which generates a focus at the output of the fibre. Through simulations, it was shown that focusing capabilities are recovered in an area around the original target. This area where the intensity of the recovered focus is at least 70% of the fully corrected focus was named the isoplanatic patch. The isoplanatic patch was shown to decrease when increasing the amount of bending applied to the fibre, as more coupling occurs between the fibre modes and the assumption about the diagonality of the TM becomes further from the actual TM. However, within some limits, the approach can correct for around a quarter of the output facet.

However, in order to use the fibre for imaging, the correction must be generated for the entire output facet. Thus, a method utilising multiple target correction foci was described in the thesis. As each correction target has an associated isoplanatic patch, a method of combining the information from different targets was required. The method split the desired output field into regions, each associated with a correction target, which were individually back-propagated through the fibre using their associated diagonal TMs. Then, the resulting fields at the input facet were summed to give the corrected input field.

The correction approach was not limited to focusing at the distal facet of the fibre. Free-space propagation was analytically described through the use of angular spectrum and was used to allow for the change in the axial position of the focusing plane. The methods described above were combined to show that adequate correction is achievable for axial distances up to 50 μm and bending inverse radii of 12 m^{-1} with the use of six target corrected foci.

The second main contribution of the thesis was a novel approach in simulating Bragg gratings in multimode optical fibres. The method follows the literature approach of coupled-modes analysis, but continues the approach by directly solving the set of differential equations generated. The thesis presented simulated results of different gratings: their associated resulting optical fields at the Bragg wavelength and their spectrum. This approach can provide an important tool in optimising the parameters for a Bragg grating if it were to be used as a reflector in the correction approach described previously. However, it could also be used in other applications where Bragg gratings would be required inside multimode optical fibres.

In conclusion, the thesis provides a set of tools and approaches which will be useful in tackling the issue of changes in light transmission through an optical fibre due to bending being introduced. This can have an important impact in improving *in vivo* imaging quality and allowing a better understanding of biological processes which can be observed with this method.

7.2 Outlook

The correction approach and the Bragg grating simulations were only tested in a simulated environment. An important step which needs to be taken is to validate the approaches with experimental data.

The sensorless adaptive optics was described in the thesis as a solution to recovering a focus at a desired reflector target. However, this process is lengthy in time and the results might not be able to reach an optimum correction. Thus, different approaches which improve upon these drawbacks might need to be implemented. However, as long as the result of recovering a specific focus is achieved, the rest of the correction procedure can be used.

The correction approach also has some drawbacks. Specifically, during the project, I have tried to implement the memory approach experimentally. However, I ran into issues relating to the aberrations present in the system. As the change in phase component of the diagonal elements is required to be measured, a precise evaluation of the optical field at the proximal facet is required. Thus, the experimental system must be robust to aberrations or have a very good understanding of them in order to eliminate their influence.

Furthermore, a real-world fibre is only an approximation to an ideal step-index fibre. Thus, to find the correct mode profiles, effects such as diffusion (index change at core-cladding interface is not exactly a step function) and manufacturing imperfections will affect the propagation mode basis.

There is also the question of the specific geometry of the Bragg grating if it were to be used as a reflector. For good localisation of the focus, the grating should be very small in both transversal and axial directions. However, a short grating leads to a very small amount of reflection, which can lead to issues in detecting the reflected signal, especially if there is a large amount of reflection at the proximal facet as well. It is also possible there are other geometries available which could solve this issue, though, this has not been investigated.

Another issue which can arise is that when using multiple reflectors and trying to optimise for the focus at one of them, light from the other reflectors could also be reflected, as even in the ideal case a perfect focus cannot be achieved due to the discrete nature of fibre modes, which would not allow for a good optimisation. Further investigation is necessary to find whether this is a large issue at small inverse bending radii. However, Bragg gratings could be the solution to this problem, as by changing the grating period and using light at multiple wavelengths, the reflection is discriminated between reflectors. But, even in this case, there is an issue in that the memory effect corrections at different wavelengths need to be correlated into an overall correction at the excitation wavelength.

In my opinion, the next steps in building upon the work in this project in terms of the bending correction procedure would be to find the right reflector, solve the aberrations issue and build as thorough as possible the mode basis of the real-world fibre.

Furthermore, I think that graded-index fibres should also be investigated in the context of this correction approach, as I think that due to their greater robustness to bending, they would take advantage even more of the correction approach to expand their range of bending robustness.

Finally, as mentioned above, thorough experimental validation is also needed for the Bragg grating theory presented in this thesis.

References

[1] S. Vasquez-Lopez *et al.*, "Subcellular spatial resolution achieved for deep-brain imaging in vivo using a minimally invasive multimode fiber," *Light: Science and Applications*, vol. 7, no. 110, 2018. DOI: `https://doi.org/10.1038/s41377-018-0111-0`.

[2] L. Shuhui *et al.*, "Memory effect assisted imaging through multimode optical fibres," *Nature Communications*, vol. 12, no. 3751, 2021. DOI: `https://doi.org/10.1038/s41467-021-23729-1`.

[3] R. Hooke, *Micrographia.* The Royal Society, 1667.

[4] C. S. Ball, "The early history of the compound microscope," *Bios*, vol. 37, pp. 51–60, 2 1966.

[5] A. Elliott, "Confocal microscopy: Principles and modern practices," *Current Protocols in Cytometry*, vol. 92, e68, 1 2020.

[6] I. Smith, I. Parker, and M. Bootman, "Fluorescence microscopy," *Cold Spring Harbor protocols*, vol. 2014, 10 2014.

[7] M. Lin and M. Schnitzer, "Genetically encoded indicators of neuronal activity," *Nature neuroscience*, vol. 19, pp. 1142–1153, 9 2016.

[8] J. Lisman, "The challange of understanding the brain: Where we stand in 2015," *Neuron*, vol. 86, pp. 864–882, 4 2015.

[9] J. Kerr and W. Denk, "Imaging in vivo: Watching the brain in action," *Nature reviews. Neuroscience*, vol. 9, pp. 195–205, 3 2008.

[10] D. Kobat, N. Horton, and C. Xu, "In vivo two-photon microscopy to 1.6-mm depth in mouse cortex," *Journal of biomedical optics*, vol. 16, p. 106 014, 10 2011.

[11] T. Wang *et al.*, “Quantitative analysis of 1300-nm three-photon calcium imaging in the mouse brain,” *eLife*, vol. 9, 2020.

[12] M. Plöschner, T. Tyc, and T. Čižmár, “Seeing through chaos in multimode fibres,” *Nature photonics*, vol. 9, pp. 529–535, 8 2015.

[13] R. K. Tyson, *Principles and Applications of Fourier Optics*. IOP Publishing, 2014.

[14] A. Yariv, *Optical electronics in modern communications*. Oxford University Press, 1997.

[15] S. Addanki, I. Amiri, and P. Yupapin, “Review of optical fibres - introduction and applications in fiber lasers,” *Results in Physics*, vol. 10, pp. 743–750, 2018.

[16] D. Flaes *et al.*, “Robustness of light-transport processes to bending deformations in graded-index multimode waveguides,” *Physical Review Letters*, vol. 120, p. 2 333 901, 23 2018.

[17] M. Plöschner *et al.*, “Gpu accelerated toolbox for real-time beam-shaping in multimode fibres,” *Optics Express*, vol. 22, pp. 2933–2947, 3 2014.

[18] S. Farahi *et al.*, “Dynamic bending compensation while focusing through a multimode fiber,” *Optics Express*, vol. 21, pp. 22 504–22 514, 19 2013.

[19] R. Gu, R. Mahalati, and J. Kahn, “Design of flexible multi-mode fiber endoscope,” *Optics Express*, vol. 23, pp. 26 905–26 918, 21 2015.

[20] G. Gordon *et al.*, “Characterizing optical fiber transmission matrices using metasurface reflector stacks for lensless imaging without distal access,” *Physical Review X*, vol. 9, p. 041 050, 4 2019.

[21] Y. Liu *et al.*, “Bending recognition based on the analysis of fiber specklegrams using deep learning,” *Optics and laser technology*, vol. 131, p. 106 424, 2020.

[22] P. Fan, T. Zhao, and L. Su, "Deep learning the high variability and randomness inside multimode fibers," *Optics Express*, vol. 27, pp. 20 241–20 258, 15 2019.

[23] S.-Y. Lee, GitHub repository containing Matlab functions for generating the LP modes of an optical fibre. Last accessed on 12-10-2024. [Online]. Available: `https://github.com/szuyul/MMF-simulation.git`.

[24] R. Davies and M. Kasper, "Adaptive optics for astronomy," *Annual review of astronomy and astrophysics*, vol. 50, pp. 305–351, 1 2012.

[25] K. Hampson *et al.*, "Adaptive optics for high-resolution imaging," *Nature Reviews Methods Primers*, vol. 1, no. 68, 1 2021.

[26] J. Primot, "Theoretical description of shack-hartmann wave-front sensor," *Optics Communications*, vol. 222, pp. 81–92, 1-6 2003.

[27] V. Lakshminarayanan and A. Fleck, "Zernike polynomials: A guide," *Journal of modern optics*, vol. 58, pp. 545–561, 7 2011.

[28] Q. Hu *et al.*, "The lattice geometry of walsh-function-based adaptive optics," *Photonics*, vol. 9, p. 547, 8 2022.

[29] J. Schwiegerling, *Optical Specification, Fabrication, and Testing.* SPIE Press, 2009.

[30] Wikipedia, Accessed on 20.08.2024. [Online]. Available: `https://en.wikipedia.org/wiki/Hadamard_transform`.

[31] R. Turcotte *et al.*, "Deconvolution for multimode fiber imaging modeling of spatially variant psf," *Biomedical Optics Express*, vol. 11, no. 8, 2020. DOI: `https://doi.org/10.1364/BOE.399983`.

[32] R. Kashyap, *Fiber Bragg Gratings.* Academic Press, 1999.

[33] D. Ko and J. Sambles, “Scattering matrix method for propagation of radiation in stratified media: Attenuated total reflection studies of liquid crystals,” *journal of the Optical Society of America A*, vol. 5, pp. 1863–1866, 11 1988.

[34] J. Zhang, “Multimode optical fiber bragg gratings: Modeling, simulation and experiments,” Ph.D. dissertation, McMaster University, 2004.